*instruments*

MDPI

*Review*

# Transition Edge Sensors: Physics and Applications

**Mario De Lucia [1,2,*], Paolo Dal Bo [2,3], Eugenia Di Giorgi [2,3], Tommaso Lari [1,2], Claudio Puglia [2] and Federico Paolucci [1,2]**

[1] Dipartimento di Fisica, Università di Pisa, Largo Bruno Pontecorvo 3, 56127 Pisa, PI, Italy; tommaso.lari@phd.unipi.it (T.L.); federico.paolucci@pi.infn.it (F.P.)
[2] INFN Sezione di Pisa, Largo Bruno Pontecorvo 3, 56127 Pisa, PI, Italy; p.dalbo@studenti.unipi.it (P.D.B.); eugenia.digiorgi@unitn.it (E.D.G.); claudio.puglia@pi.infn.it (C.P.)
[3] Dipartimento di Fisica, Università di Trento, Via Sommarive 14, 38123 Trento, TN, Italy
* Correspondence: mario.delucia@unipi.it

**Abstract:** Transition Edge Sensors (TESs) are amongst the most sensitive cryogenic detectors and can be easily optimized for the detection of massive particles or photons ranging from X-rays all the way down to millimetre radiation. Furthermore, TESs exhibit unmatched energy resolution while being easily frequency domain multiplexed in arrays of several hundred pixels. Such great performance, along with rather simple and sturdy readout and amplification chains make TESs extremely compelling for applications in many fields of scientific endeavour. While the first part of this article is an in-depth discussion on the working principles of Transition Edge Sensors, the remainder of this review article focuses on the applications of Transition Edge Sensors in advanced scientific instrumentation serving as an accessible and thorough list of possible starting points for more comprehensive literature research.

**Keywords:** Transition Edge Sensor (TES); superconducting detector; low temperature; astronomy; dark matter; cosmic microwave background; neutrinos; X-ray



**Citation:** De Lucia, M.; Dal Bo, P.; Di Giorgi, E.; Lari, T.; Puglia, C.; Paolucci, F. Transition Edge Sensors: Physics and Applications. *Instruments* **2024**, *8*, 47. https://doi.org/10.3390/instruments8040047

Academic Editor: Pasquale Arpaia

Received: 31 July 2024
Revised: 30 September 2024
Accepted: 17 October 2024
Published: 31 October 2024



## 1. Introduction

Advanced scientific instrumentation and up-and-coming technologies require detectors with exceptional performance. Making use of detectors with excellent resolving powers, extremely low noise and limited spurious and dark counts will allow for ambitious results in a large number of scientific applications including, but not limited to, astronomy, cosmology, particle physics, biophysics, chemistry and quantum computing. Arguably, a very promising way to achieve such demanding performances is to rely on low-temperature superconducting detectors. At low temperatures, spurious thermal dark counts become negligible and, if paired with single photon sensitivity, such detectors can be optimized to be excellent photon counters at all wavelengths of the energy spectrum. Naturally, they can also be deployed as highly sensitive calorimeters.

As we shall discuss in this review, among the plethora of superconducting detectors Transition Edge Sensors (TESs) are the most widely used because of their excellent energy resolution, their relatively easy fabrication process and their capability of being frequency domain multiplexed. TESs are extremely sensitive superconducting thermometers and their working principle is surprisingly simple.

For most materials, as their temperature decreases, so does their electrical resistivity, but those that are known to exhibit a superconducting phase-transition feature a sudden drop to zero in resistivity when they are cooled below a certain temperature, known as superconducting critical temperature ($T_C$), specific to each superconductor. In the proximity of $T_C$, the resistance vs temperature curve can be very steep, leading to a variation of up to several Ohms (Ω) in a range of a few milli-Kelvins (mK). Further details and a reading list on the phenomenology of superconductivity can be found in Section 2.

In a nutshell, a TES can be imagined as a superconductor kept in contact with a bath (reservoir) at temperature $T_C$ to which a voltage bias is applied. Upon the striking of a particle which deposits its energy in the TES, it is then temporarily heated up to a temperature $T > T_C$ before cooling down again to the reservoir temperature. In this process, the resistance of the TES increases with its temperature and therefore with the energy deposited in the detector itself. In such a picture, the steeper the superconducting transition the more sensitive the TES is, in a trade-off that links the sensitivity to the dynamic range of the detector.

Further details on the working principle of a Transition Edge Sensor and its electro-thermal feedback can be found in Section 3 along with an in-depth discussion on its multiplexing, the amplification chains, its noise and cross-talk sources.

In Section 4, we present the most prominent applications for Transition Edge Sensors in the field of astronomy and astrophysics, while Section 5 will discuss the applications of TESs for nuclear, particle and astroparticle physics including dark matter detection.

The development of TESs for applications as bio-imagers is discussed in Section 6, while Section 7 describes the applications of Transition Edge Sensors in the field of quantum optics and quantum communications. TES arrays see a wide application as X-ray detectors; their applications as spectroscopes and X-ray imagers are discussed in Section 8. Finally, Section 9 contains a brief introduction to the working principles of other superconducting detectors and a discussion on how they compare with TESs.

While the physics and application of TESs have been covered in other review articles and books have been published over the last two decades, they often appear to be either too broad or extremely niche-specific. We would still like to acknowledge their contribution and present them to the interested reader. The two publications by Enss [1] (Ed.) and Enss and Mccammon [2] mostly focus on the physics of low temperature micro-calorimeters, Gottardi and Nagayashi [3] present the applications of TESs in the field of astronomy and astroparticle physics, Nucciotti [4], Pirro and Mauskopf [5], Poda and Giuliani [6], and Poda [7] describe the use of TESs for applications in nuclear and particle physics, while Koehler [8] and Ullom and Bennett [9] discuss the use of TESs as X-ray detectors. Differently, the purpose of this review paper is to provide a useful handbook on TESs starting from their working principles and their main figures of merit in order to convey their critical importance in many scientific applications. In order to facilitate the use of this article, a table of contents is available at the end of the text.

## 2. Superconductivity

Superconductivity is the prototypical example of macroscopic quantum effect, since some of the electrons are condensed into a superfluid state extending through the entire system. The condensation occurs for electronic temperatures ($T$) lower than a critical value, known as critical temperature ($T_c$). As $T$ decreases, the number of condensed electrons increases until full condensation is reached at $T = 0$. Indeed, a superconductor can be represented by means of a two fluids model including normal electrons, known as *quasiparticles* and coupled condensed electrons, known as Cooper Pairs.

### *2.1. Phenomenology*

Despite it being usually identified with only zero resistivity, superconductivity is experimentally described by the all following phenomena [10].

**Zero resistivity.** The DC electrical resistivity of a superconductor shows a steep transition to zero at $T \lesssim T_c$ [10]. Zero resistivity is preserved for injected currents lower than a threshold value, known as *critical current* ($I_c$). At $T = 0$, $R = 0$ is true for AC signals up to a critical frequency $\omega_c \approx 3.5 k_B T_c/\hbar$ (with $k_B$ the Boltzmann constant and $\hbar$ the reduced Planck constant), thus indicating a lower limit to excite electrons from the condensed to the normal state.

**Response to magnetic fields.** A bulk superconductor exhibits the *Meissner effect* [11], which is the expulsion of an external magnetic field. To exclude the magnetic field from

its bulk, a superconductor increases its free energy till reaching the normal state value at the *critical field* ($H_c$) [12], which is maximum at $T = 0$ and is fully suppressed at $T = T_c$. Finally, the magnetic flux passing through a cylindrical superconductor shows a $hc/2e$ (with $h$ being the Planck constant, $c$ the speed of light and $e$ the electron charge) [13,14], where the factor 2 arises from the double charge of a Cooper pair.

**Specific heat.** The specific heat of a superconductor shows a discontinuity with respect to the normal state value at $T_c$. The 1.43 times larger value of the superconductor specific heat is strongly connected to formation of a condensate and its associated condensation energy [15]. In addition, the specific heat decreases exponentially with temperature ($\propto e^{-T_c/T}$) differently from its linearity in the normal state ($\propto T$); thus, a superconductor shows a smaller specific heat for $T \ll T_c$ [16]. This behaviour is due to the fact that Cooper pairs (condensed electrons) are not able to store thermal energy.

**Energy gap.** As already introduced for the AC electrical response of a superconductor, there is a forbidden energy range, known as the *superconducting energy gap* ($\Delta$), between the superconducting condensate and the normal electrons [10,15]. In particular, $\Delta$ increases monotonically as T decreases; thus, the superconducting state becomes more favourable at low temperatures. The energy gap can be measured through electron tunnel spectroscopy, since single electron transport is allowed only for voltages $V \geq \Delta/e$ [17]. Differently, a superconductor can absorb radiation of frequency $\nu \geq 2\Delta/h$ [18], since both electrons forming a Cooper pair need energy $\Delta$ to switch to the normal state [19].

### *2.2. Brief Introduction to BCS Theory*

The Bardeen–Cooper–Schrieffer (*BCS*) theory provides the microscopic explanation of the superconductivity [20]. In particular, BCS describes the superconducting state as a boson condensate living at energies lower than the metallic normal state. This is possible by assuming that at $T = 0$ the fundamental state of a metal (Fermi sea) is unstable for the addition of a weak attractive interaction between a couple of electrons, i.e., the Cooper pair [21].

To provide a simple explanation of the BCS theory, we can perform a *Gedankenexperiment* (thought experiment): we add two electrons $[\overrightarrow{k_1}, E(\overrightarrow{k_1})]$ and $[\overrightarrow{k_2}, E(\overrightarrow{k_2})]$ to the fundamental state of a gas of non-interacting electrons. These electrons occupy previously empty states above the Fermi level ($E_F$). For the Pauli exclusion principle, the two electrons cannot occupy states with $|\overrightarrow{k}| < k_F$ (with $k_F$ the Fermi wavevector); thus, a weak attractive potential needs to build up. On the one hand, the two electrons continuously change their wavevector; on the other hand, the total momentum is conserved

$$\overrightarrow{k_1} + \overrightarrow{k_2} = \overrightarrow{k_1'} + \overrightarrow{k_2'} = \overrightarrow{K}, \tag{1}$$

where $\overrightarrow{K}$ is the momentum of the Cooper pair. Indeed, the interaction is allowed in the intersection between the spherical cortex of thickness $\hbar\omega_D$ (with $\omega_D$ the Debye frequency) around $\overrightarrow{k_1}$ and $\overrightarrow{k_2}$. The maximum attractive force is provided by $\overrightarrow{K} = 0$; thus, the two electrons forming the Cooper pair have wavevectors of the same absolute value and opposite direction ($\overrightarrow{k_1} = -\overrightarrow{k_2} = \overrightarrow{k}$). The Schrödinger equation for the Cooper pair reads

$$-\frac{\hbar^2}{2m}(\nabla_1^2 + \nabla_2^2)\Psi(\overrightarrow{r_1}, \overrightarrow{r_2}) + V(\overrightarrow{r_1}, \overrightarrow{r_2})\Psi(\overrightarrow{r_1}, \overrightarrow{r_2}) = (\varepsilon + 2E_{F,0})\Psi(\overrightarrow{r_1}, \overrightarrow{r_2}), \tag{2}$$

where $V$ is the interaction potential, $\overrightarrow{r_i}$ is the position of the $i$-th electron (with $i = 1, 2$), $\varepsilon$ is the energy of the electrons pair with respect to the non-interacting state ($V = 0$) and $E_{F,0}$ is the single-electron Fermi energy (the factor 2 accounts for the coupled electrons). In the presence of an attractive potential, the general solution of the Schrödinger equation is:

$$\Psi(\overrightarrow{r}) = \frac{1}{L^3}\sum_k g(\overrightarrow{k}) e^{i\overrightarrow{k}\overrightarrow{r}}, \tag{3}$$

where $L$ is the space coordinate, $\overrightarrow{r} = \overrightarrow{r_1} - \overrightarrow{r_2}$ are the real space relative coordinates of the two electrons and $|g(\overrightarrow{k})|^2$ is the probability of finding an electron in $\overrightarrow{k}$ and the other in $-\overrightarrow{k}$. By substituting Equation (3) in Equation (2) and assuming an interaction independent of $\overrightarrow{k}$ with a value of $V_0$ (occurring only in the spherical cortex $\hbar\omega_D$), we can evaluate the energy difference of the electrons with respect to the non-interacting state for weak coupling as

$$\varepsilon \simeq -2\hbar\omega_D e^{-2/V_0\mathcal{N}(E_{F,0})}, \tag{4}$$

where $\mathcal{N}(E_{F,0})$ is the density of states at the Fermi level for 1 spin type. Equation (4) shows that a bounded 2-electron state of energy lower than the Fermi sea can occur at $T = 0$. Thus, the fundamental state of a non-interacting electron gas is unstable in the presence of a weakly attractive potential. It is possible to demonstrate that this instability is brought to the formation of a large density of Cooper pairs; thus, the fundamental state of lowest energy is the *superconducting state*. Since the superconducting wave function is symmetric, the Pauli exclusion principle implies that the two electrons forming the Cooper pair have opposite spin. We also note that the Cooper pairs are bosons, thus occupying the same energy level.

The total energy of the fundamental superconducting state ($W_{BCS,0}$) considers all the possible configurations of coupled electrons, the kinetic energy of the Cooper pair and energy reduction due to interaction.

$$W_{BCS,0} = \sum_k \xi_k \left(1 - \frac{\xi_k}{E_k}\right) - L^3 \frac{\Delta^2}{V_0}, \tag{5}$$

where $\xi_k = \hbar^2 k^2/2m - E_{F,0}$ is the kinetic energy of a Cooper pair, and $E_k = \sqrt{\xi_k^2 + \Delta^2}$ is the total energy of a Cooper pair. Thus, the condensation energy of the superconducting state, obtained by subtracting the normal-state energy ($W_{N,0}$) to $W_{BCS,0}$, reads

$$\frac{W_{BCS,0} - W_{N,0}}{L^3} = -\frac{1}{2}\mathcal{N}(E_{F,0})\Delta^2. \tag{6}$$

Thus, the energy gap provides a measure of the energy reduction of the superconducting state. The first excited BCS state implies the breakage of a Cooper pair; that is, an energy $2\Delta$ is necessary ($\Delta$ for each electron). An uncoupled electron, also known as *quasiparticle*, can only occupy states of energy $\Delta$ above the fundamental state. Thus, the quasiparticle density of states of a superconductor at $T = 0$ takes the form

$$\mathcal{N}_S(E) = \mathcal{N}_N(E_{F,0})\Re\left(\frac{E}{\sqrt{E^2 - \Delta^2}}\right), \tag{7}$$

where $\mathcal{N}_N(E_{F,0})$ is the normal-state density of states and $\Re$ represents the real-part component. The density of states of a superconductor strongly depends on temperature, since the energy gap obeys

$$\frac{1}{V_0\mathcal{N}_N(E_{F,0})} = \int_0^{\hbar\omega_D} \frac{\mathrm{d}\xi}{\sqrt{\xi^2 + \Delta^2}} \left[1 - 2f\left(\sqrt{\xi^2 + \Delta^2} + E_{F,0}, T\right)\right], \tag{8}$$

where $f\left(\sqrt{\xi^2 + \Delta^2} + E_{F,0}, T\right)$ is the temperature-dependent Fermi function. Finally, the critical temperature of a superconductor is related to the zero-temperature energy gap ($\Delta_0$) through

$$\Delta_0 = 1.764 k_B T_c. \tag{9}$$

### *2.3. Engineering Artificial Superconductors by Proximity Effect*

The optimization of TES detectors for different applications requires the development of artificial superconductors with engineered $T_c$. A rather standard approach exploits the so-called *proximity effect* [22]: a weakened superconducting wave function penetrates in a normal metal placed in good ohmic contact with a superconductor. As a consequence, the $T_c$ of a TES can be adjusted by changing the relative thickness of the superconducting ($S$) and normal metal ($N$) thin films forming a bilayer (see Figure 1a).

The superconducting properties of an $SN$ bilayer can be predicted by means of the Usadel theory [23]. The Usadel theory can be applied for dirty systems [24,25], that is the diffusive charge transport both in $S$ and $N$. The superconducting properties of the bilayer are translationally invariant in the $(x, y)$-plane, while they vary along the $z$-axis. By exploiting a function $\theta(z)$ describing the superconducting state, the pairing potential obeys the coupled Usadel equations

$$\begin{cases} \frac{\hbar D_j}{2}\partial_z^2(\theta_j) + iE\sin\theta_j - \left[\frac{\hbar}{\tau_{sf,j}} + \frac{\hbar D_j}{2}\left(\partial_z(\varphi) + \frac{2e}{\hbar}A_z\right)^2\right]\cos\theta_j\sin\theta_j + \Delta_j(T,z)\cos\theta_j = 0 \\ \Delta_j(T,z) = \mathcal{N}_S V_{eff}\int_0^{\hbar\omega_D}\tanh\left(\frac{E}{2k_BT}\right)\Im\left(\sin\theta_j\right)\mathrm{d}E \end{cases} \tag{10}$$

where $D_j$ is the normal-state electron diffusion constant, $E$ is the energy, $\tau_{sf,j}$ is the spin-flip time, $\varphi$ is the superconducting phase, $\Delta(z,T)$ is the temperature ($T$) and $z$ dependent effective superconducting energy gap, $\mathcal{N}_S$ is the density of states at the Fermi level, $V_{eff}$ is the pairing potential and $j = S, N$ indicates the superconductor and normal metal side. This version of the Usadel theory does not consider the impact on the proximity effect of the electrical resistance between $N$ and $S$, because the large contact area provides a negligibly small contribution.

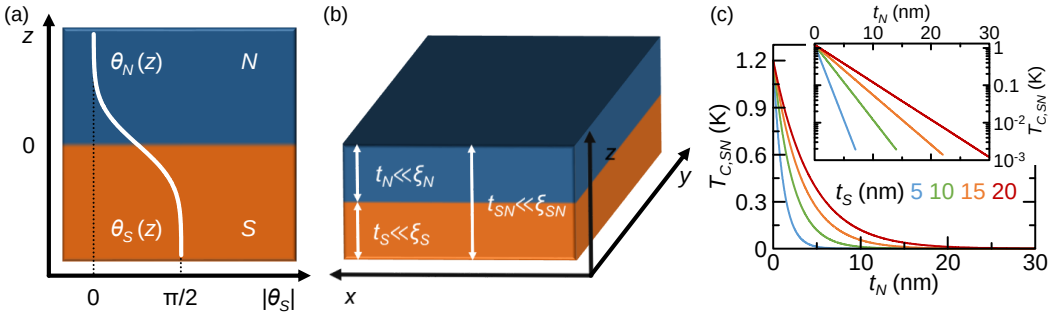


**Figure 1. Proximity effect and critical temperature engineering.** (**a**) Schematic representation of the $z$-dependence of the parameter $\theta_i$ describing superconductivity in an $SN$ bilayer (with $i = S, N$). (**b**) Schematics of the Cooper limit for an $SN$ bilayer, where $t_i$ is the thickness of the $i$ element and $\xi_i$ is its coherence length (with $i = S, N, SN$). (**c**) Critical temperature of an $SN$ bilayer versus $t_N$ for different values of $t_S$ with $S$ aluminium and $N$ copper. The parameters used for Equation (10) are as follows: $T_{C,S} = 1.2$ K, $\omega_{D,N} = 7.98 \times 10^{13}$ rad/s the Debye frequency of copper, $\mathcal{N}_S = 2.15 \times 10^{47}$ J$^{-1}$m$^{-3}$ the density of state at the Fermi level of aluminium, $\mathcal{N}_N = 1.56 \times 10^{47}$ J$^{-1}$m$^{-3}$ the density of state at the Fermi level of copper and $\mathcal{T}_{SN} = 1$ the transmission probability of the $SN$ interface.

The absolute value of the complex function $\theta_j$ obtained by solving the coupled Usadel Equations (Equation (10)) ranges from 0 (normal-state) to $\pi/2$ (fully superconducting state). Figure 1a schematically shows the evolution of $|\theta_j|$ with $z$ within the $SN$ bilayer. The negligible $SN$ resistance implies the continuity of the $\theta_j(z)$ function, that is $\theta_S(z = 0) = \theta_N(z = 0)$ and $\partial_z\theta_S(z = 0) = \partial_z\theta_N(z = 0)$, with $z = 0$ being the interface between $S$ and $N$. Differently, $\theta_j(z)$ would show a discontinuity at the interface for large resistances between the two layers [26]. In either case, the superconducting energy gap and, therefore, the critical temperature vary strongly along the $z$-axis. Consequently, the $R$ versus $T$ characteristic of the $SN$ bilayer would show an extremely broad transition to zero resistance.

Sensitive TESs require a sharp transition to the superconducting state; that is, the $SN$ bilayer is expected to posses a superconducting energy gap constant along the $z$-axis. This is achieved for $SN$ bilayers lying in the *Cooper limit* [27] (see Figure 1b), thus fulfilling the following requirements

1. The thickness of the superconductor thin film ($t_S$) is lower than its superconducting coherence length (typical distance between the two paired electrons [10]): $t_S \ll \xi_S$;
2. The thickness of the normal metal layer ($t_N$) is smaller than its coherence length: $t_N \ll \xi_N = \sqrt{\hbar D_N/(2\pi k_B T)}$;
3. The thickness of the $SN$ bilayer ($t_{SN}$) is less than its effective coherence length ($\xi_{SN}$) $t_{SN} \ll \xi_{SN} = \sqrt{\hbar(t_S D_S + t_N D_N)/(t_{SN}\Delta_{SN})}$ (with $\Delta_{SN}$ being the effective bilayer superconducting energy gap).

These conditions ensure that the coherence is fully preserved along the $z$-axis both in the superconducting and normal states. As a consequence, superconductivity is not affected by the non-ideality (finite charge diffusion, amorphous thin film and defects) of the normal metal thin film and the $SN$ bilayer behaves as a monolithic superconductor.

The effective critical temperature of an $SN$ bilayer within the Cooper limit can be approximated to [28]

$$T_{c,SN} = T_{c,S}\left[\left(\frac{k_B T_{c,S}}{1.13\hbar\omega_{D,N}}\right)^2 + \left(\frac{k_B T_{c,S}\lambda_{F,N}^2\left(\frac{1}{t_N\mathcal{N}_N} + \frac{1}{t_S\mathcal{N}_S}\right)}{2.26\mathcal{T}_{SN}}\right)^2\right]^{t_N\mathcal{N}_N/2t_S\mathcal{N}_S}, \quad (11)$$

where $T_{c,S}$ is the critical temperature of $S$, $\omega_{D,N}$ is the Debye frequency of the normal metal, $\lambda_{F,N}$ is the Fermi wavelength of $N$, $\mathcal{N}_N$ is the density of states at the Fermi level of the normal metal and $\mathcal{T}_{SN}$ is the interface transmission probability. Figure 1c shows the dependence of the critical temperature of an Al/Cu bilayer ($T_{C,SN}$) as a function of the thickness of the Cu film ($t_N$) for selected values of the thickness of Al ($t_S$). Interestingly, $T_{C,SN}$ decreases exponentially with $t_N$, as shown by the inset. Furthermore, by decreasing $t_S$, the critical temperature of the bilayer decreases faster for increasing $t_N$, because the superconducting wavefunction is *weaker* and the proximitization of $N$ is less efficient.

### *2.4. Thermal Properties*

The sensitivity of a TES strongly depends on the thermal exchange mechanisms between the different elements when power or energy are absorbed. The various components of a TES lie within the quasi-classical diffusive limit [10]; that is, their physical dimensions are larger than their Fermi wavelength ($\lambda_F$) and elastic mean free path ($\lambda_{free}$) of electrons. Thus, the electron energy distribution can be well described by the Fermi function and the thermal transport can be simply described by energy diffusion. Here, we will describe the main thermal exchange mechanisms occurring in a TES.

The thermistor of a TES is kept at the superconducting-to-normal-state transition, thus showing the thermal properties of a normal metal. Indeed, its charge carrier thermalization is dominated by *electron–electron scattering*, either due to direct Coulomb interaction or impurities [29]. Within these conditions, the electron–electron thermalization length scale reaches tens of μm [30]; thus, the electronic temperature ($T_e$) can be considered homogeneous all over the entire thermistor. Differently, the thermal conductance of a superconductor ($G_{th,S}$) at $T_e \ll T_c$ is exponentially damped by the presence of the energy gap [31]. Indeed, the Cooper pairs do not transport heat and the number of unpaired electrons decreases exponentially with temperature [10]. In the linear response approximation, $G_{th,S}$ can be expressed as [32]

$$G_{th,S} \simeq G_{th,N}\frac{6}{\pi^2}\left(\frac{\Delta_0}{k_B T_e}\right)^2 e^{-\Delta_0/k_B T_e}, \quad (12)$$

where $G_{th,N}$ is the normal-state thermal conductance.

One of the main thermalization channels of the charge carriers in the thermistor is given by the scattering with the film phonons. In particular, the *electron–phonon scattering* in a clean normal metal can be calculated by [29]

$$P_{e\text{-}ph,N} = \Sigma \mathcal{V}\left(T_e^5 - T_{ph}^5\right), \tag{13}$$

where $\Sigma$ is the electron–phonon coupling constant, $\mathcal{V}$ is the volume and $T_{ph}$ is the phonon temperature. We stress that the exponent can be $n = 4.6$ for dirty metals depending on the type of impurity immersed in the metallic matrix. Similarly to energy transport, the electron–phonon thermalization is exponentially damped in the superconducting state ($P_{e\text{-}ph,S}$) with respect to the normal metal value ($P_{e\text{-}ph,N}$). Indeed, within the linear approximation limit, the electron–phonon thermalization takes the form [33]

$$P_{e\text{-}ph,S} \propto P_{e\text{-}ph,N} e^{-\Delta_0/k_B T_e} \tag{14}$$

In full agreement with thermal conductivity, this behaviour is related to the suppression of the single-electron population in a superconductor with decreasing temperature [10]. Indeed, the Cooper pairs do not exchange energy with the crystal, since their scattering with the phonons is forbidden.

Andreev Mirrors

Usually, the electrodes contacting the thermistor are made of a superconductor of critical temperature much larger than the operating temperature of the TES, that is the critical temperature of the thermistor. Indeed, these superconducting leads act as energy filters, the so-called *Andreev thermal mirrors* [34], thus confining the electron overheating in the thermistor. In the linear response regime, the thermal conductance of an $SN$ contact is suppressed with respect to the conventional value given by the Wiedemann–Franz law by a factor

$$\delta G_{th,NS} = \left(\frac{p_0}{2\pi}\right)^2 \frac{f_0}{\sqrt{\varphi(\eta) k_B T_e/\Delta_0^3}} e^{-\Delta_0/k_B T_e}, \tag{15}$$

where $p_0$ is the Fermi momentum, $\eta = 2H/H_c - 1$ is a dimensionless factor representing the impact of an external magnetic field, $\varphi(\eta) = e^{ip_0 \hat{n}\cdot\vec{r}}\eta$ (with $\hat{n}$ being the unit vector and $\vec{r}$ the real space vector) is tabulated, and $f_0 = \int_0^1 \cos\alpha f(\cos\alpha) \mathrm{d}\cos\alpha \sim 1$ (with $\alpha$ being the incidence angle of the electrons at the interface and $f$ is a slowly varying function). Intuitively, the strong reduction of the thermal conductance can be understood by considering that the hot electrons in the normal metal find a limited number of accessible quasiparticle states within the superconducting gap to diffuse. Thus, the perfect Andreev mirror effect occurs only for very low values of the electronic temperature ($T_e \ll T_c$). By rising $T_e$, the Fermi distribution of the hot electrons in $N$ broadens and reaches the quasiparticle peaks in the density of states of the superconductor. Therefore, hot electrons of the normal metal find available states in $S$ and $G_{th,NS}$ approaches the conventional Wiedemann–Franz value. Indeed, the clean contact between and Al/Cu bilayer and Al lead showed efficient thermal insulation for temperatures up to about 280 mK, that is $\sim 0.22 T_c$ of the aluminium film [35].

## 3. Physics of Transition Edge Sensors

The idea of exploiting a superconducting thin film at temperatures close to its critical temperature as a detector has been around since the 1940s, when proposed by Andrews et al. [36] as infra-red radiation detectors. In particular, the proposed device exploits the steep change in resistance to detect the energy deposited by a striking particle in Figure 2.

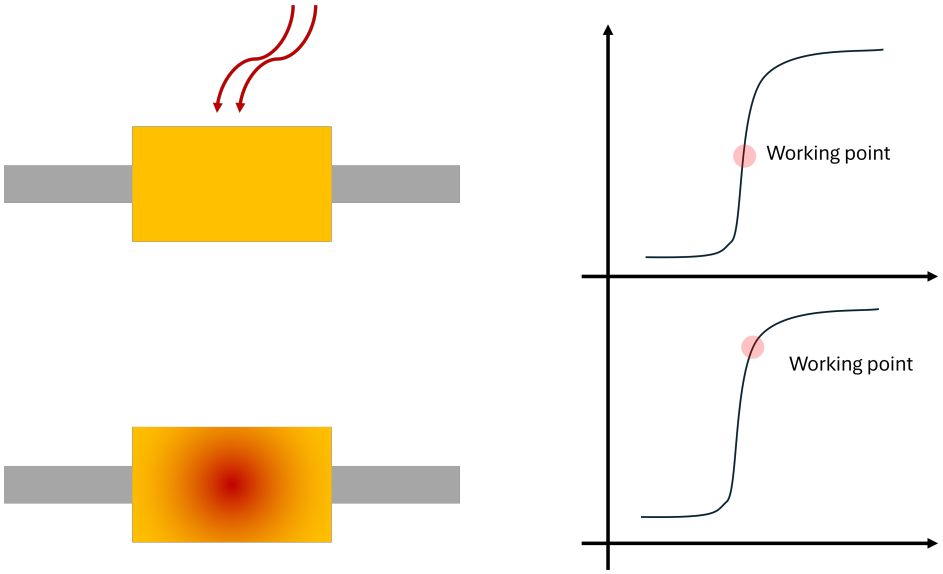


**Figure 2. Working principle of a Transition Edge Sensor.** An event (e.g., photon/phonon absorption) heats the superconductor, moving its temperature from the ideal working point (center of the normal to superconducting transition).

A Transition Edge Sensor (TES) can be modelled as a thin film with a finite thermal capacity $C$ connected to a reservoir at temperature $T_R$ as shown in Figure 3. Any energy deposited onto the film by radiation or particles striking on the TES is converted into heat and then dissipated towards the reservoir with a characteristic time which is inversely proportional to the thermal conductance $G$. Considerations based on the conservation of energy result in the following equation that describes the heating of the film when irradiated or struck by a particle

$$P_{ext} = P_R(T, T_R) + C\frac{dT}{dt}, \tag{16}$$

where $P_{ext}$ is the power deposited by the particle or the radiation, $P_R$ represents the power dissipated towards the thermal reservoir and can be assumed to depend linearly on the temperature difference between the electronic temperature $T_e$ (see Section 2.4) referred to simply as T from now on, and $T_R$ through the thermal conductance $G$, assumed constant in the first approximation. Equation (16) can be, therefore, rewritten as

$$P_{ext} = G(T - T_R) + C\frac{dT}{dt}, \tag{17}$$

which yields two particular solutions in two specific cases

1. $T = T_R + \frac{P_0}{G}$ in case $P_{ext} = P_0$ is a constant
2. $\delta T = \frac{\delta P_{ext}}{\tau_0}\frac{1}{1-i\omega\tau}$ with $\tau = \frac{C}{G}$ with the obvious meaning of the symbols.
   In particular, an instantaneous deposit of energy $E_0$ results in an instantaneous increase in temperature by $\Delta T = \frac{E_0}{C}$ with an exponential decay with time constant $\tau = \frac{C}{G}$.

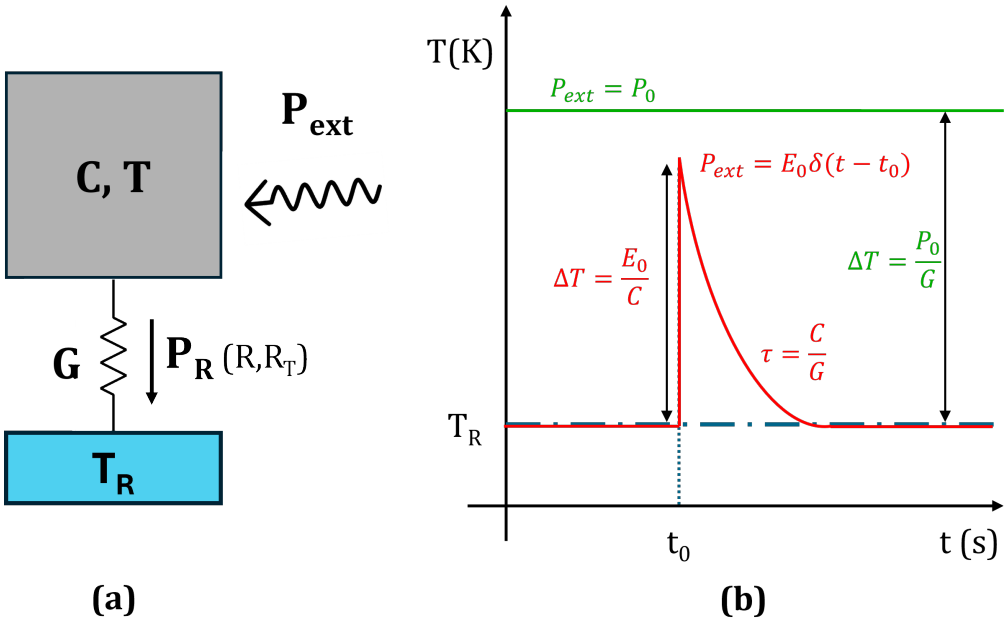


**Figure 3. Working principle of a TES not in electro-thermal feedback.** (**a**) The thermal scheme of a TES with temperature and heat capacity $C$, the weak thermal link to the reservoir through a thermal conductance $G$ and the external power $P_{ext}$ and power exchanged to the reservoir $P_R(R, R_T)$. (**b**) Solution to Equation (17) of the TES as a function of time in the two aforementioned cases.

### *3.1. Negative Electro-Thermal Feedback*

Transition Edge Sensors initially faced challenges in adoption in the scientific community mostly due to their complexity and the difficulty in keeping the TES stable in temperature. This issue was only solved in 1995 by Kent D. Irwin [37], who proposed and successfully established a voltage-biased negative electro-thermal feedback (NETF) of the TES in order to keep its stability in temperature. Such a feedback is typically implemented by adding in parallel to the TES a shunt impedance $Z_L$ with $Z_L << R(T, I)$ so as to contribute to the previous thermal equation with an extra Joule component. The electric scheme of this circuit is shown in Figure 4a, whereas Figure 4b describes its thermal behaviour. Through the effect of the Joule component, the thermal and electrical equations are paired and thus the scheme takes the name of electro-thermal feedback.

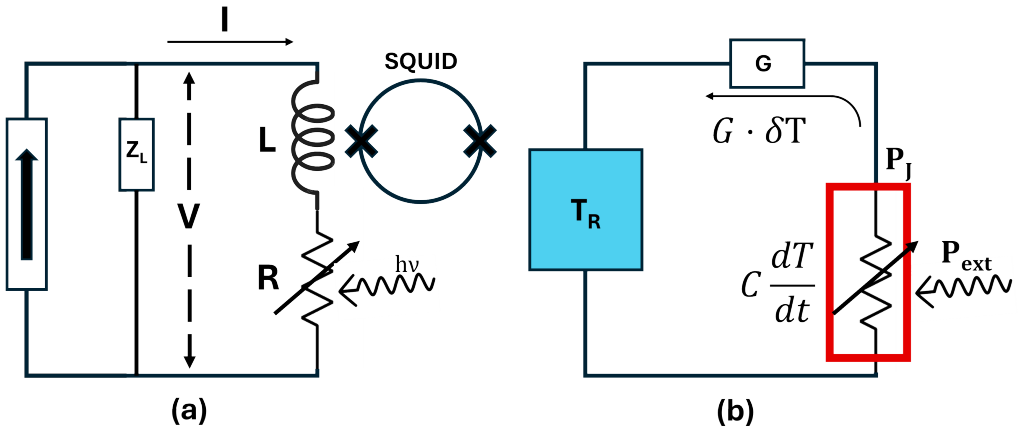


**Figure 4. The schematic of a TES biased in negative electro-thermal feedback.** (**a**) Electric scheme of a TES and (**b**) thermal scheme of a TES. Both schemes contribute to the coupled differential equations in Equation (18).

Two coupled differential equations can be written, one to take into account the thermal behaviour of the superconducting film and the second to represent the electrical behaviour of a TES in its NETF scheme.

$$\begin{cases} C\frac{dT}{dt} = -P_R(T, T_R) + P_J + P_{ext}, \\ L\frac{dI}{dt} = V - IZ_L - IR(T, I). \end{cases} \tag{18}$$

where $C$ is the heat capacity of the TES and absorber subsystem, $T$ is the temperature of the TES, $P_{ext}$ is the signal power, $P_j$ is the power dissipated through the resistance of the TES, $P_R$ is the power exchanged between the TES and the reservoir kept at temperature $T_R$ (thermal feedback) that contributes to cooling down the TES after detection, $L$ is the inductance, $V$ is the Thevenin-equivalent bias voltage that is applied to the TES, $Z_L$ is the shunt impedance and $R(T, I)$ is the resistance of the TES, which depends on the temperature of the TES as well as the current flowing through it.

The I–V characteristic of the system can be determined by solving the coupled differential equations in their steady state ( $\frac{dT}{dt} = 0$, and $\frac{dI}{dt} = 0$ ). For the sake of simplicity, we will assume that the resistance of the TES does not depend on the current flowing through it but only on its temperature ($\beta = \frac{I}{R}\frac{dR}{dI} = 0$). An in-depth analysis of the $\beta \neq 0$ case is discussed by Irwin and Hilton [38]. In the steady state, which describes a condition of dynamic equilibrium between the TES, the reservoir and the external radiation, we can write

$$P_{ext} + P_J = const. \tag{19}$$

From Equation (19), we can infer that as long as $P_J$ is constant, the product $I \cdot V$ is kept constant; hence, the I–V curves of a TES describe the branch of a hyperbola. This holds true until the TES is driven outside of its superconducting state by the external load or because of the Joule power dissipated through the TES itself. When the TES is driven outside of its transition, it is described by its ohmic behaviour and therefore all the hyperbola branches connect to the same straight line, the slope of which represents the normal-state resistivity of the TES. Assuming that the bias load $Z_L$ is negligible, the typical I–V curves of a TES are shown in Figure 5a where curves of different colors represent different values of $P_{ext}$.

Once we have discussed the I–V characteristic curves of the TES in its NETF configuration, it is worth briefly discussing the detection principle and the operation of a TES as a bolometer and as a calorimeter.

To reiterate, when a deposition of energy occurs onto the TES, its temperature increases and so does its resistance. If biased correctly in an NETF scheme, this results in an increased current flowing through the TES (according to the I–V curves shown in Figure 6), which can be further amplified and read out. The main difference between the two operational regimes is the nature of the impinging power: if it is transferred to the TES (or its absorber) instantaneously or with a time-scale which is much faster than the characteristic time-scale of the TES response in NETF, it is said to be operated as a calorimeter (single photon/particle detector). Differently, if the power is delivered to the TES in a time-scale which is comparable or even larger (imagine an optical flux or the variations thereof) than the characteristic time-scale of the TES in NETF, the TES is said to be operated as a bolometer. From a purely physical point of view, there is not a large difference other than the functional dependency of $P_{ext}(t)$ in Equation (18). Figure 6a,b show the operation of a TES as a bolometer (See Section 3.2), whereas Figure 7a,b show the operation of a TES as a calorimeter (See Section 3.3).

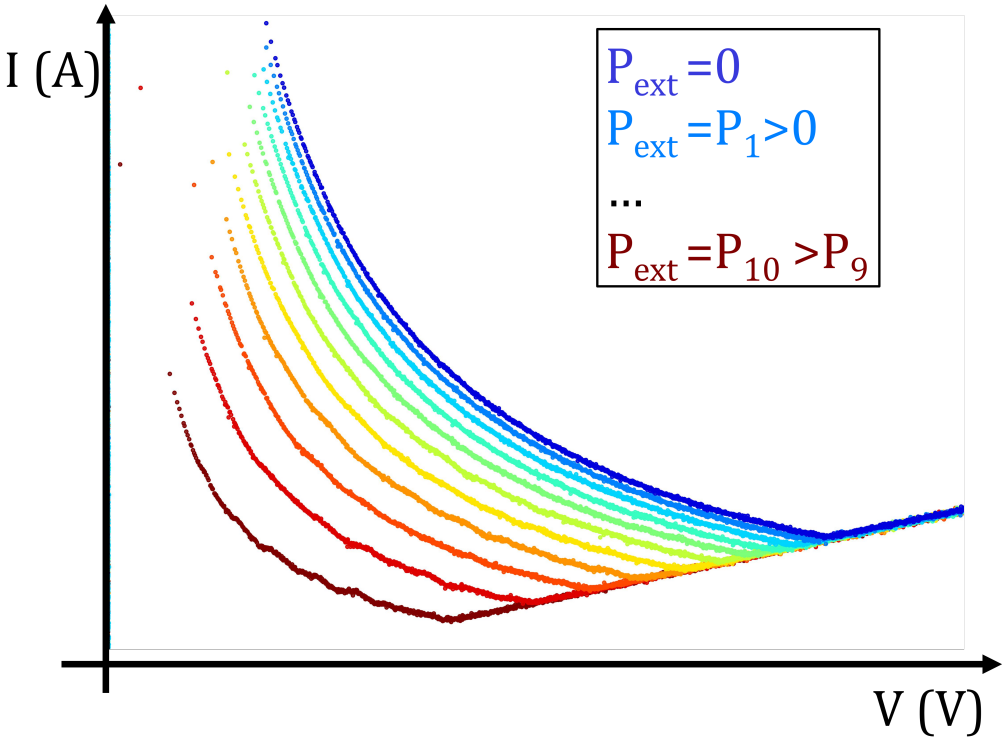


**Figure 5. Measured I–V curves of a TES**. The I–V characteristic of a TES can be derived as the steady-state solution of Equation (18). The top most blue curve represents the case in which no optical load heats up the TES, whereas all the other curves represent increasing values of $P_{ext}$ as described in the legend.

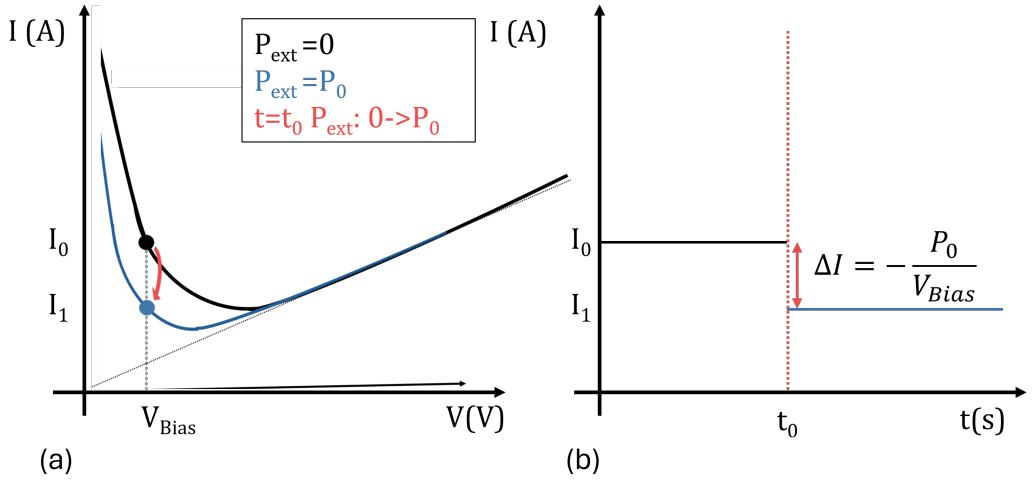


**Figure 6. Operation of a TES in a bolometric regime.** (**a**) Two I–V curves relative to $P_{ext} = 0$ (black) and $P_{ext} = P_0$ (blue). At time $t = t_0$, the external power is turned on and the TES, biased with a voltage $V_{Bias}$, rapidly transitions from one I–V curve to the other, resulting in a different current flowing through the superconductor. (**b**) Response of the TES to the scenario described in (**a**) but represented as a function of time.

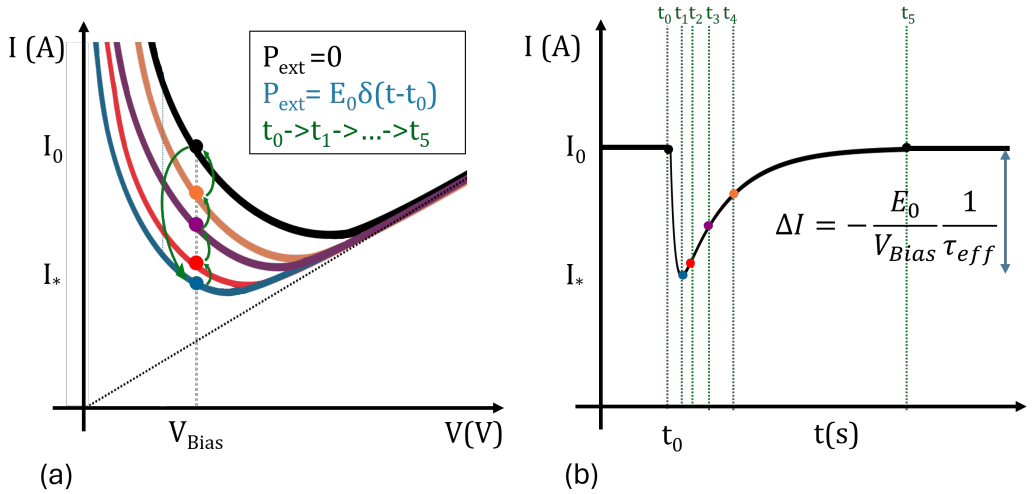


**Figure 7. Operation of a TES in a calorimetric regime.** (**a**) At time $t = t_0$, the external power is turned on and the TES for an infinitely small amount of time; the TES biased with voltage $V_{Bias}$ rapidly transitions from one I–V curve to another and back to the original curve as described by the green arrows. This results in a time-varying current flowing through the superconductor. (**b**) Response of the TES to the scenario described in (**a**) but represented as a function of time.

### *3.2. Bolometric Operation*

By addressing the steady-state case in the previous section, we have effectively also discussed the bolometric operation of a TES. A 'slow' variation of $P_{ext}$ in Equation (18) results in the bias of the TES on a different I–V curve. It is fair to say that as the energy flux impinging on the TES varies, slowly with respect to its characteristic time scales, the TES moves from one I–V curve to another and the physical signal is its bias current which, at all times, is a solution to the steady-state equations presented in Equation (18). A small change in the temperature of the TES $T \to T + \delta T$ results in a change in the Joule power $\delta P_j = -\frac{V^2}{R^2}\frac{dR}{dT}\delta T = -\mathcal{L}G\delta T$. Here, the loop-gain $\mathcal{L}$ is defined as $\mathcal{L} = \frac{\alpha P_j}{GT}$ and $\alpha = \frac{dR}{dT}\frac{T}{R}$ is the a-dimensional derivative of the transition curve.

In this configuration, when the TES is in dynamic thermal equilibrium, the sum of Joule power and external power is conserved; hence, we can write

$$P_{ext} + P_J = const \tag{20}$$

and any small fluctuation is given by:

$$\delta P_{ext} + \delta I \cdot V = 0. \tag{21}$$

Whereby, because of the fixed voltage negative electro-thermal feedback the component, $I \cdot \delta V = 0$. From Equation (21), we can infer the responsivity of the bolometer as

$$\delta I = -\frac{\delta P_{ext}}{V}. \tag{22}$$

### *3.3. Calorimetric Operation*

The calorimetric operation occurs when the impinging power is described, ideally, as $P(t) = E_0\,\delta(t - t_0)$. In the first approximation, we can imagine a small fluctuation of the impinging power $\delta P_{ext} e^{-i\omega t}$ as a generic Fourier component of an impinging power $P_{ext}(t)$. If we solve this problem in Fourier transform space, we obtain

$$\delta P_{ext} - \frac{V^2}{R^2}\frac{dR}{dT}\delta T = G\delta T - i\omega\delta T, \tag{23}$$

$$\delta P_{ext} = (-i\omega C + G + \mathcal{L}G\delta T)\delta T, \tag{24}$$

$$\delta P_{ext} = \delta T G(\mathcal{L}+1)(1-\omega\tau_{eff}), \tag{25}$$

where $\tau_{eff} = \frac{\tau}{(1+\mathcal{L})}$ is the new time constant of the system, which not only depends on $C$ and $G$, but also now depends on the loop parameters which can significantly speed up the response of the TES. Furthermore, by applying Ohm's law, we can infer

$$\delta I = -\frac{V}{R^2}\frac{dR}{dT}\delta T = -\frac{\mathcal{L}G}{V}\delta T. \tag{26}$$

Finally, the responsivity of the detector $S$, defined as the current produced by a unitary change in $P_{ext}$, can be evaluated as

$$S = \frac{\delta I}{\delta P_{ext}} = -\frac{1}{V}\frac{\mathcal{L}}{(\mathcal{L}+1)}\frac{1}{1-i\omega\tau_{eff}}. \tag{27}$$

Equation (27) describes the response of a TES in NETF to any periodic variation of $P_{ext}$. Through it, the response of any optical input can be determined by decomposing it into its Fourier components and computing the transfer function independently before re-combining the solutions; we want to focus on the two most interesting cases:

1. For slow-varying signals ( $\omega << 1/\tau_{eff}$) and in a strong electro-thermal feedback ($\mathcal{L} >> 1$) the responsivity of the detector only depends on the bias voltage

$$S \propto -\frac{1}{V}, \tag{28}$$

   which is consistent with what we discussed in Section 3.2 where we addressed the bolometeric operation of a TES.
2. The current response of the system to an instantaneous delta-like deposit of energy can be calculated through the 1-pole transfer function as

$$I(t) = -\frac{1}{V}\frac{E_0}{\tau_{eff}}e^{-\frac{t}{\tau_{eff}}}\left(\frac{\mathcal{L}}{\mathcal{L}+1}\right), \tag{29}$$

   which in a strong electro-thermal feedback ($\mathcal{L} >> 1$) can be further simplified as:

$$I(t) = -\frac{1}{V}\frac{E_0}{\tau_{eff}}e^{-\frac{t}{\tau_{eff}}}. \tag{30}$$

Since the currents produced by such systems are extremely small, in order to effectively detect the response of a TES detector, the signal thus produced needs to be amplified before being digitized. The most widespread approach involves a superconducting quantum interference device (SQUID) operated as an amplifier (further details in Section 3.6). The main advantage of a SQUID-based amplifier involves its capability of acting as an 'ideal' transconductance amplifier, with an almost zero input impedance and a large output impedance. Thus, the SQUID amplifier couples all the current produced by the TES to its input and while amplifying the signal, it converts it into a voltage turning an impedance-sensitive measurement into a more standard voltage measurement that can be performed with a Digital-to-Analog Converter (DAC).

### *3.4. Inductive Bias*

As a small note, in some applications where noise is critical, it might be worth using a purely inductive load to bias the TES $Z_L = L_L$. This results in the effective reduction of the Johnson noise component, which is due to the finite resistance of the shunt resistance $R_L$. Further details on noise can be found in Section 3.8.

### *3.5. TES Examples*

For the sake of completeness, before further discussions on the technological details and the applications of Transition Edge Sensors, we believe it is appropriate to show two different TESs intended for the detection of cosmic microwave background radiation as part of two different experiments LSPE/SWIPE and LiteBIRD, described in Sections 4.4.14 and 4.4.15, respectively. Figure 8 shows a Transition Edge Sensor developed during the R&D phase of the LSPE/SWIPE experiment; it consists of a Au/Ti/Au trilayer which allows for the fine control of the critical temperature of the film (280 mK) on a SiN membrane, which decouples the TES from the Si substrate and helps to achieve a high sensitivity of the TES by reducing the thermal capacity. The thermal link to the bath is achieved through a gold spiderweb which also acts as an absorber. The size of the spiderweb is ≈8 mm in diameter, while the diameter of the inner core of the web, which hosts the TES (as shown in the inset of Figure 8), measures ≈ 370 µm in diameter.

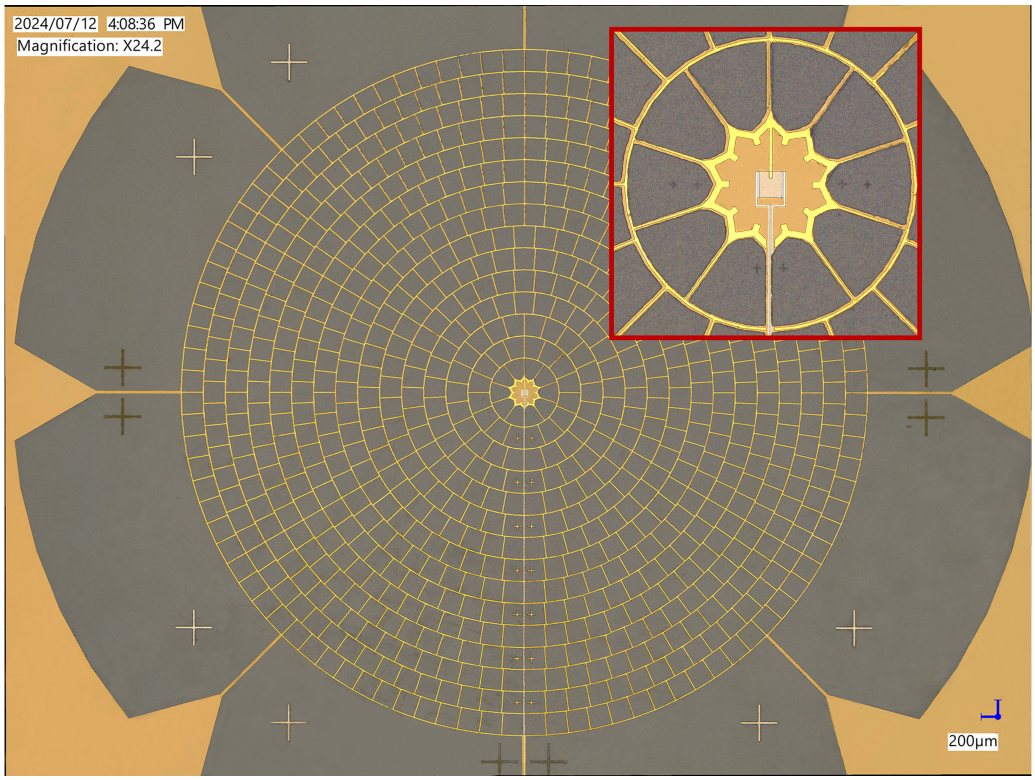


**Figure 8. A spiderweb TES** developed during the R&D phase of the LSPE/SWIPE experiment. The red inset shows a close-up on the TES thermistor.

The chip shown in Figure 9 represents one of the polarimeters (i.e., two detectors sensitive to the two polarizations of light) of the Medium and High Frequencies Telescope (MHFT) that will be part of the payload of the LiteBIRD spacecraft. Each chip consists of two TESs and four membrane-suspended antennas for the detection of the two components polarized separately [39]. The radiation thus coupled to the antennas is fed through a filter-bank for multichroic sensing and is then absorbed in the form of dissipated heat on a membrane-suspended TES (shown in the inset). The TESs, fabricated at the (American) National Institute of Standards and Technology (NIST), are made of Al/Mn films with a critical temperature of 200 mK.

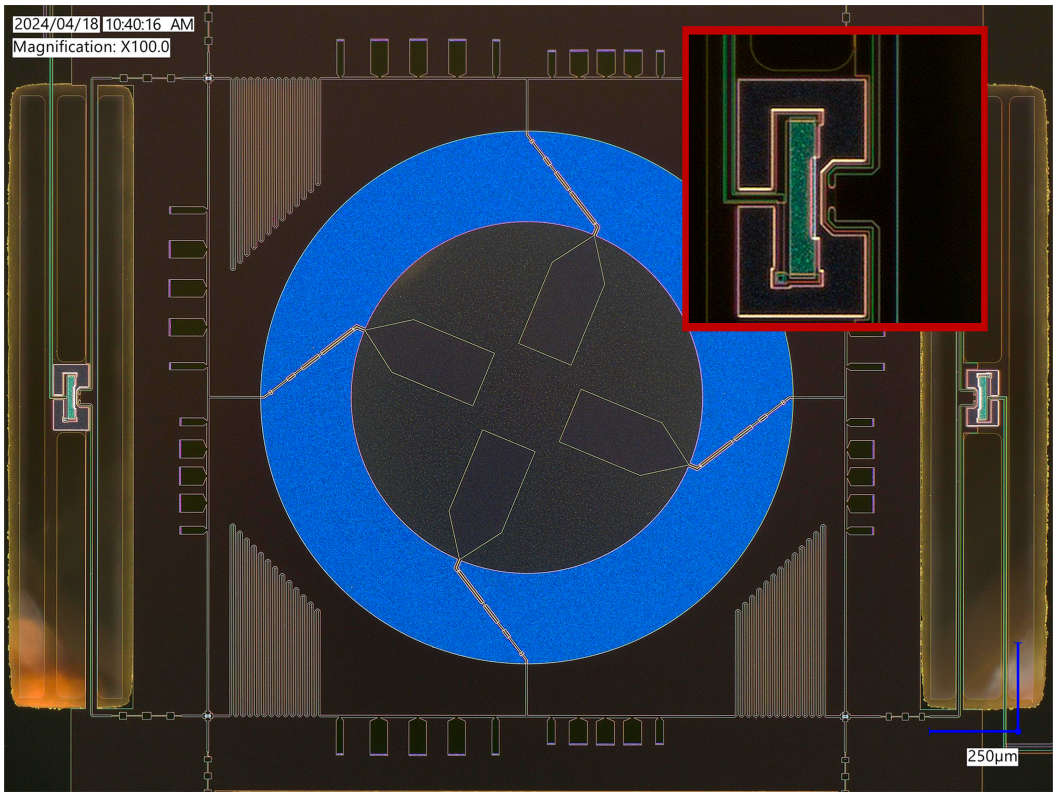


**Figure 9. An antenna-coupled TES** fabricated by NIST which will find application on the MHFT instrument of the LiteBIRD spacecraft. The red inset shows a close up on the TES thermistor.

### *3.6. SQUID Amplification*

#### 3.6.1. DC-SQUID

A SQUID is a superconducting ring, also known as a SQUID washer, interrupted by one (RF-SQUID) or two (DC-SQUID) weak links in the form of Superconductor–Insulator–Superconductor junction, Superconductor–Normal Metal–Superconductor junction, Dayem bridge, etc. [40]. The schematic of a DC-SQUID is shown in Figure 10a. Generally, when a SQUID is biased with a current $I_B$, a variation in the magnetic flux coupled to the SQUID washer, it produces a voltage swing across the junctions, which is periodic with a fixed period defined by the magnetic flux quantum $\phi_0$ ($\frac{h}{2e} = 2.065 \cdot 10^{-15}$ Wb). The trans-characteristic curve of a DC-SQUID that correlates the magnetic flux ($\Phi$) with the voltage generated across the junctions is shown in Figure 10b. The V–$\Phi$ curve is steepest when the flux applied is an even multiple of $\phi_0$: $\Phi = (2n-1)\phi_0/4$. In such a configuration, the response of the DC-SQUID to a small magnetic flux $d\Phi << \phi_0$ is linear and the transfer coefficient $V_\Phi = \partial V/\partial\Phi$ is maximum. In order to use a DC-SQUID as an amplifier, usually, one fixes its working point around any one solution of $\Phi = (2n-1)\phi_0/4$ by having a static flux coupled into the SQUID washer through an apposite flux bias coil and coupling the current signal that needs to be amplified through a separate closely coupled thin-film input coil. This is also recreated in SQUID Array amplifiers which combine a large number of SQUIDs connected in series and in parallel in order to optimize the trans-characteristics and the performance of the device.

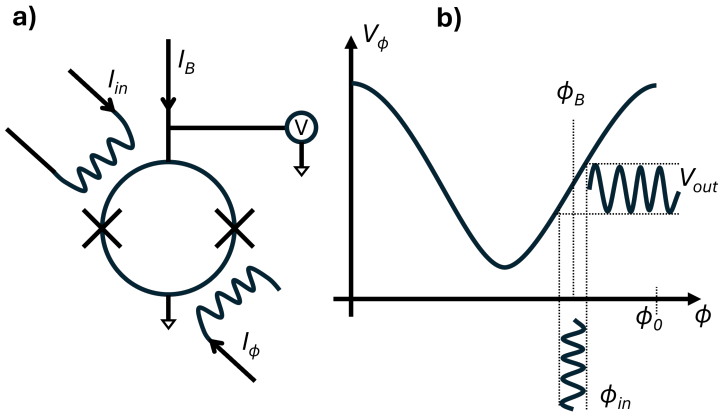


**Figure 10. Scheme of a SQUID amplifier.** (**a**) Electrical scheme of a SQUID amplifier. (**b**) $V_\phi$ characteristics of a SQUID amplifier and the response of the system related to the shape of the characteristic.

#### 3.6.2. SQUID Array Amplifiers

The majority of TES devices leverage the DC-SQUID as the most sensitive detector of magnetic flux currently available. To date, SQUIDs have been used in innumerable low-frequency applications, including gravitational wave detection [41], susceptometry [42], biomagnetism [43], non-destructive evaluation [44] and magnetic resonance imaging [45]. Recently, growing interest in low-noise radio frequency and microwave amplification for particle detection [46], infrared sensor readout and superconducting quantum bit measurements [47] has formed. In these applications, SQUIDs are one of the leading candidates due to their very low power dissipation and good noise characteristics.

Connecting a number of identical DC-SQUIDs in series can considerably amplify the relatively small voltage signal produced by each device individually. In case an array of identical SQUIDs is biased at an identical working point and the same magnetic flux is coupled into each SQUID, the array acts like a single SQUID with an enhanced transimpedance which is ideally the product of the individual contributions. Series SQUID arrays provide outstanding slew rate performance because the linear flux range is preserved. Arrays of 100 SQUIDs are commonplace, and several mV output signals can be achieved. Although the voltage noise density across the array increases linearly with the number of SQUIDs, a 100-SQUID array can drive a room-temperature preamplifier directly [48] and increase the system noise only slightly above the intrinsic noise of the SQUID array. The flux noise density and input current noise density both scale inversely with the number of SQUIDs, conserving a constant coupled energy resolution. In principle, a pickup coil could be coupled to the input coil to form a magnetometer, but series SQUID arrays are almost always used as transimpedance amplifiers in configurations like two-stage SQUIDs or readout devices for cryogenic particle detectors. Experimental results showed a very high bandwidth on the order of 100 MHz with 100-SQUID arrays [49,50].

It is worth noticing that the performance of SQUID amplifiers can be boosted by having arrays with a similar number of SQUIDs in series as in parallel, in particular, to overcome the detrimental effect of a non-uniform bias configuration [51] and to decrease the overall noise of the system [52].

In most applications or instruments, a SQUID is used as a null-detector device linearized through negative feedback [48]. The negative feedback modes of operation include flux-lock modes. In such operation modes, the feedback signal is coupled to the SQUID: an external signal applied to the input coil generates a flux in the SQUID, which is countered by an opposing flux in the feedback coil coupled to the SQUID's inductance. If the feedback and input coils are not screened adequately enough, the feedback signal couples, together with the modulation signal, if conventional readout electronics are used, to the input circuit and interacts with the load. Also, in experiments where the load inductance is usually superconducting and variable, the feedback coupling changes with the load due to

screening effects. Therefore, the SQUID should be designed such that the coupling of the feedback and modulation signals to the input circuit is negligible. This can be achieved by designing the SQUID layout with separate secondary coils for the input and feedback flux transformers.

For specifically critical applications, multiple SQUID arrays can be cascaded [53]. Some applications include those cases in which the signal-to-noise ratio (SNR) needs to be pushed to its maximum, or those in which the thermal budget at the cold state of the cryostat is limited or those in which the amplifier needs to be thermally decoupled from the detectors. While there is no unique cascading scheme [53–56], the general approach to a multi-stage SQUID amplification chain relies on a first stage which acts as a 'front-end' amplifier, i.e., exhibits a limited amplification gain and a large bandwidth in order to not distort the signal. Unfortunately, such a SQUID amplifier also exhibits a rather limited saturation power which also limits the multiplexing factor of TESs read out in parallel through a multi stage SQUID chain. The first stage acts as an emitter–follower transducing an impedance-sensitive signal such as the current produced by the TES into a much handier voltage signal which can be further amplified by the later stage SQUID amplifiers. Since the front-end amplifier produces a voltage signal, such voltage can be fed into a series of SQUID arrays anchored to a plate at a higher temperature. The later stages, commonly referred to as the 'booster' [54], can dissipate more heat because the cooling power increases largely at higher temperature and the amplification factor of a SQUID array is proportional to the power it dissipates [57].

### *3.7. Multiplexing*

In light of all the reasons discussed so far, the operation of a TES occurs at extremely low temperatures well below 1 K. Even the most advanced commercial refrigerators only have a very limited cooling power, usually less than 100 mW [58], at their milli-Kelvin stage. Such a small cooling power would severely hinder the up-scaling of a TES array if they were to be read out individually as the power dissipated by the SQUID arrays and the thermal-load of the signal lines would quickly saturate all the cooling power available. In order to overcome this issue, several multiplexing strategies are available and are here discussed. More in general, the multiplexing of analogue signals occurs in four defined and consequential steps:

1. **Bandwidth limitation** is essential in order to prevent any degradation of the signal due to either out-of-band detector noise aliasing into the signal band or appearing as excess cross-talk.
2. **Encoding or Modulation** is the step whereby the signals from different pixels are encoded by multiplying them by orthonormal functions.
3. **Summation** of the encoded signals into one time-ordered data stream.
4. **Decoding or De-modulation** is achieved through knowing the encoding function and applying a decoding algorithm.

In the next few sections, we will present an overview of the different possible multiplexing schemes and we will demonstrate their working principle as well as show a simulated Time-Ordered Data (TOD) in the case of a calorimetric detection. The use of a TES as a bolometer is merely a simplification of such a case where all the signals are constant.

#### 3.7.1. Time Division Multiplexing

Time Division Multiplexing (TDM) is a rather old technique dating back to the 1870s and was developed in parallel to the rise of the telegraph [59]. TDM allots a specific interval of time to each of the detectors for their readout. With the use of a switch matrix, all the detectors are read out in order in columns and rows. Ensuring a fast commuting time and a small time slot to each detector, frame rates of up to 20 kHz can be achieved [60]. For applications where the detector signals do not vary in time-scales of the order of 100 µs, this results in an effectively '*continuous*' monitoring of the source.

TDM has been widely implemented as a multiplexing scheme for Transition Edge Sensors in a large number of different schemes, all of which exploit the same working principle: a 2D array of TES ($M - rows \times N - columns$) with $M$ SQUIDs, one per each row, is read out by sequentially switching on the SQUIDs (1, 2, $\cdots$, M) during the on-phase of each of the $M$ SQUIDs. A firmware-controlled DAC biases the individual $N$TESs on the M-th row one at the time for time intervals as short as 1 µs. In order to prevent aliasing, the bandwidth of the TES is limited to below the Nyquist frequency defined by the switching interval (e.g., 500 kHz for the 1 µs switching time in the example above). This limitation is achieved with a single-pole RL low-pass filter where $R$ is the resistance of the TES and $L$ is the inductance of the input coil of the SQUID [61]. The number of channels that can be read in a TDM scheme is limited by SQUID-noise aliasing and it scales as $\sqrt{N}$ [62,63] and the energy resolution can be degraded by insufficient accuracy in the pulse arrival time. One possible implementation of a TDM scheme with only two TESs is shown in Figure 11. Figure 12 shows the working principle of a TDM readout with four TESs read out in sequential time frames. During each time frame, each TES is read out only for a fraction of the time frame. Each TES produces an individual pulse with different amplitudes and at different times. The TOD read out at room temperature given by the concatenation of the signals on each channel during their own 'on' period is shown at the top of the graph. It is worth stating that this scheme only serves the purpose of explaining the working principle of TDM. In all practical applications, the switching frequency is much higher than the characteristic time-scales with which the TES signal varies. This results in a fine sampling of the signal without a large information loss on the signals thus acquired.

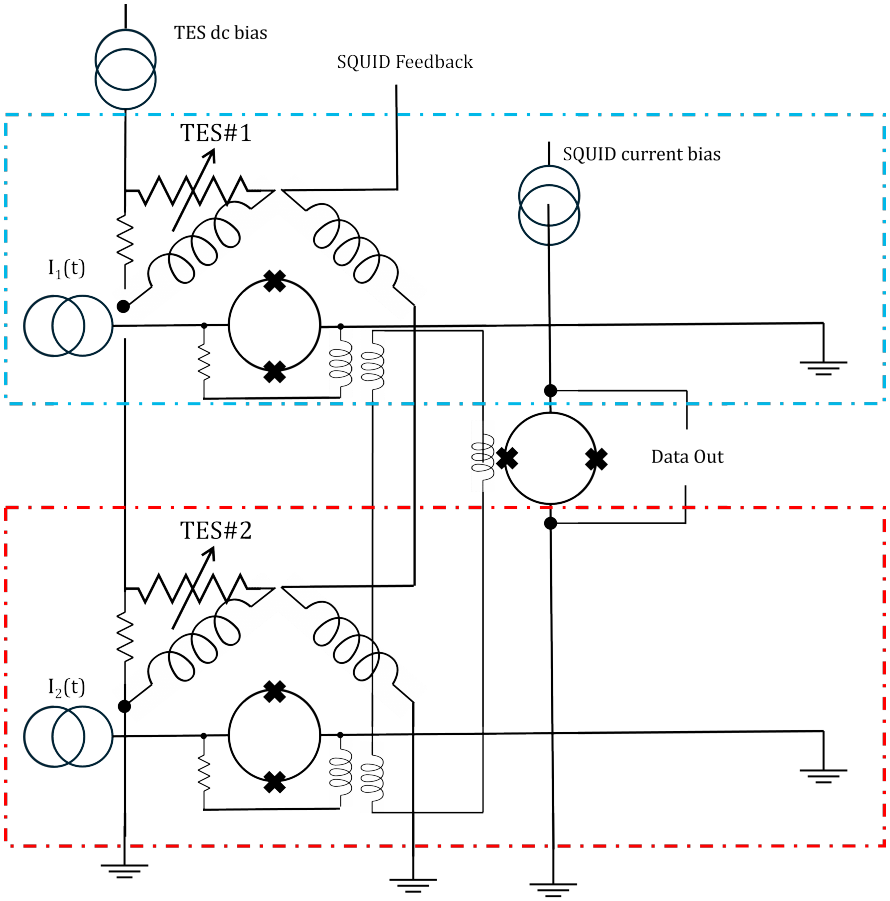


**Figure 11. Circuital schematic implementation of a two-TES TDM.** Each channel is colour coded: cyan for CH#1 and red for CH#2. The switching occurs by turning on and off the different bias lines of the SQUID amplifiers.

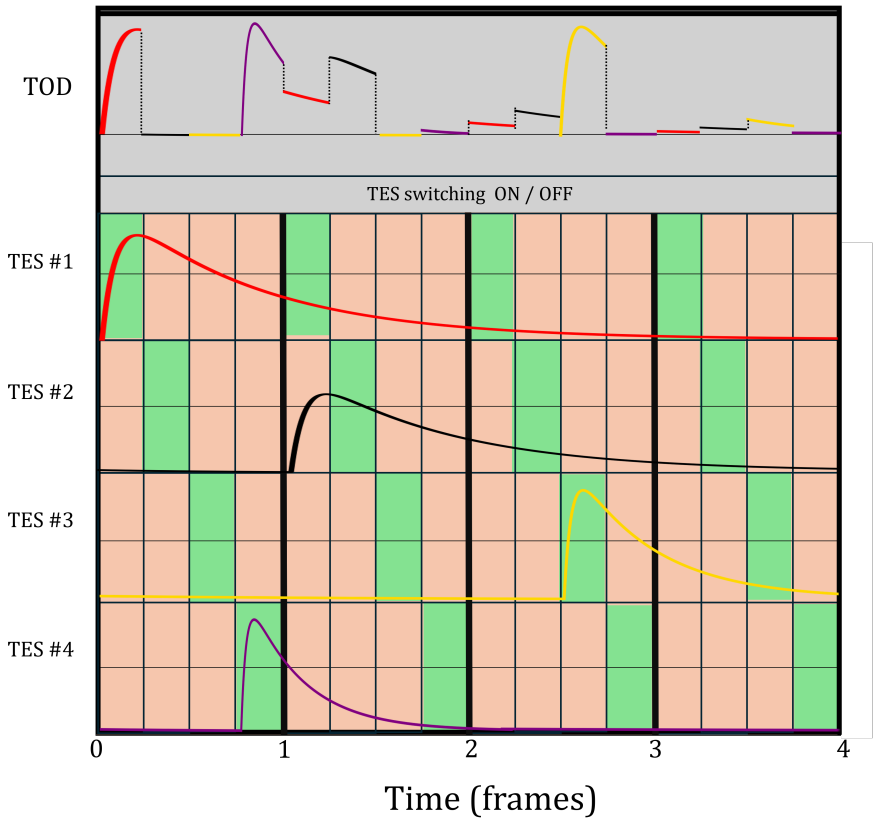


**Figure 12. Time Division Multiplexing scheme**. The signal produced by the four different TESs is shown in red, black, yellow and violet. The green (red) fields in the picture show, per each frame the time each channel is switched on (off). The TOD read out by the electronics contains the data points of the TES signals at (convolved with) their respective own on time intervals. This picture represents an extreme case where the sampling interval is comparable with the characteristic time figures of the TES and shows how such a scheme may lead to data loss because of the difficulty in reconstructing the data curves (see TES#2 in black). Ideally, the sampling time and frequency is much faster than the rise and fall time of the TESs so that a proper sampling can be achieved without data loss. If, on the other hand, the sampling interval is significantly larger than the rise and fall time of the TESs, the pulses are properly reconstructed, but the dead time of the detectors is significantly increased.

#### 3.7.2. Frequency Division Multiplexing

The Frequency Division Multiplexing (FDM) scheme exploits frequency ranges instead of time intervals, resulting in a continuous monitoring of the detectors, which solves the aliasing problem that is inherent to TDM. In FDM, each TES is connected in series to an inductor and to a capacitor, resulting in a bank of band-pass filters, as shown in Figure 13. The circuit will be eventually composed by a fixed number of branches (multiplexing factor), each of which includes the detector's variable resistance and the aforementioned LC filter. Each TES will be biased with a sine wave at a specific frequency, selected by the resonator geometry. This configuration is, alongside the TDM, the most used for the TES readout.

While ideally, the arguments discussed in Section 3 still stands, it is worth stating that, following the discussion found in Dreyer et al. [64], the responsivity of a TES biased with a sinusoidal voltage becomes

$$S = \sqrt{2}/V_c^{rms}, \tag{31}$$

where $V_c^{rms}$ is the rms of the amplitude of the sine wave and the factor $\sqrt{2}$ arises from the average voltage carried by a sine wave over one period.

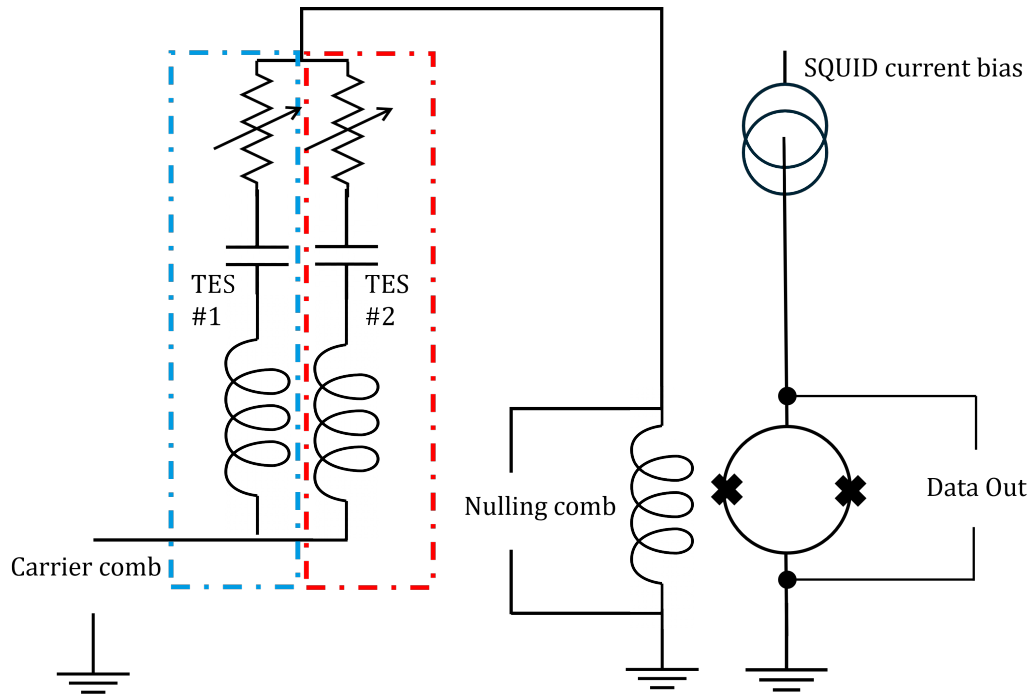


**Figure 13. Frequency Division Multiplexing**. In a simple 2-TES scheme, each detector is connected to a band-pass LC resonator filter. The comb of carriers is generated and sent to the multiplexing circuit through only one wire. Each channel is color coded, cyan for CH#1 and red for CH#2. The nulling occurs at the input coil of the SQUID amplifier.

The FDM is performed by generating a comb of sinusoidal signals at the selected resonance frequencies which are fed to the array on a single transmission line. It is up to the filter bank to distribute the bias signal to each TES, the variable resistance of which acts as an amplitude modulator to the sine waves. In the bolometric regime, the variation of the incoming radiation power leads to a variation in the resistance value of the TES and to an amplitude modulation of the bolometer bias current which can be measured. In the calorimetric regime, the impulsive signal is retrieved by de-convolving the TOD at the frequencies of each individual channel, as shown in Figure 14.

The advantage FDM holds is linked to the possibility of using a single wire for transferring the bias current to the entire circuit, which can comprehend several branches and therefore bolometers. The only limit on the number of detectors that can be read out in this configuration is set by the required bandwidth and the capabilities of the readout electronics. Moreover, the signals coming from the TES channels at different frequencies are summed in a summing node and transferred to the rest of the readout chain on a single wire, in particular to a low input impedance SQUID. This results in a decreased thermal load and lower heat dissipation at the cryogenic stages.

In general, the physical signal produced by the TES is much smaller in amplitude than the bias sine wave, therefore an inverted carrier comb, called *nulling*, is injected in the circuit at the input coil of the SQUID, as shown in Figure 13. This signal cancels out the carrier current, leaving the physical signal modulation unaltered and prevents the saturation of the dynamic range of the SQUID amplifier.

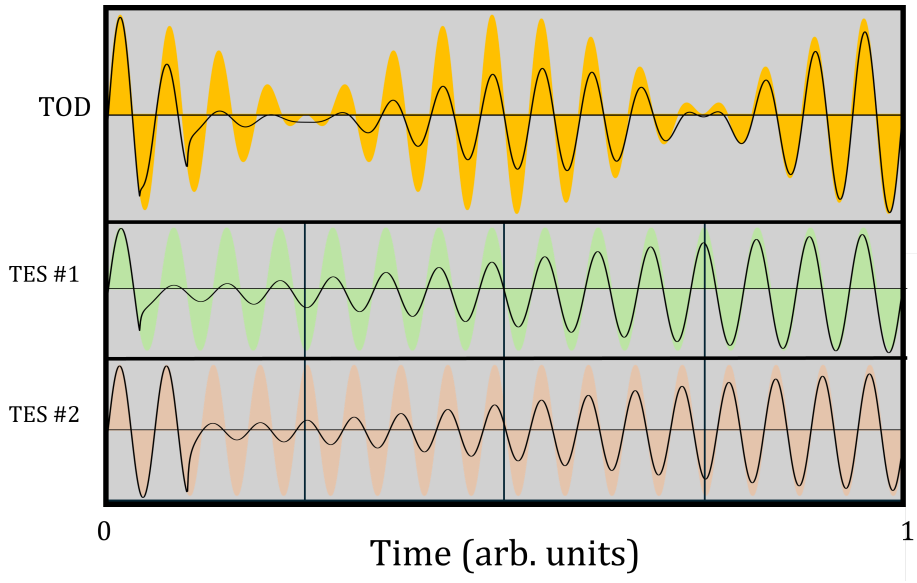


**Figure 14. Frequency Division Multiplexing scheme**. In a simple 2-TES scheme, each detector is continuously monitored. By de-convolving the TOD at the frequencies of each individual channel, it is possible to obtain information on the amplitude of the oscillations at each frequency. By then plotting the amplitude of the pulse which is the envelope function that is convoluted with the sine wave at each specific frequency, it is possible to obtain a pulse-like shape typical of a TES detector. The shaded area represents the response of the TESs in their idle state.

#### 3.7.3. Code Division Multiplexing

Code Division Multiplexing (CDM) is an architecture that combines the advantages of TDM and FDM. In TDM, the modulating function that distinguishes the pulses produced by different detectors is a combination of $N$ square waves with low duty cycle whereas in FDM, the modulation is achieved through $N$ sinusoidal waves at different frequencies. The major breakthrough of CDM is that the detectors have the polarity of their coupling to the SQUID amplifier modulated by Walsh matrices [62]. The simplest case possible is that of a two-channel CDM: the sum and the difference of the signals from TES#1 and TES#2. Knowing the sum and difference of the two signals allows the unique identification of the two individual signals. The advantage of CDM compared to TDM and FDM is that while the SQUID noise is degraded by a factor $\sqrt{N}$, $N$ samples of the $N$ pixels are read out at each frame, therefore resulting in a $\sqrt{N}$ improvement in signal-to-noise ratio [65]. Unfortunately, the very simplified case of using Walsh matrix modulation has yielded non-profitable results due to the complexity of achieving bandwidth limitation in such architecture. Two solutions have been proposed and developed: CDM with flux summation and CDM with current steering. Regardless of the architecture it is implemented in, the working principle of CDM is explained in Figure 15. The top of the figure shows the TOD of four different pulses as produced by four TESs. The signals are equally distributed, with $1/4$ amplitude across the four channels and the coupling to each SQUID that defines the channels is achieved with a polarity that is unique to each TES-Channel pair. The de-multiplexing is achieved by comparing the polarity combination of each pulse on the different feedlines with a look-up table.

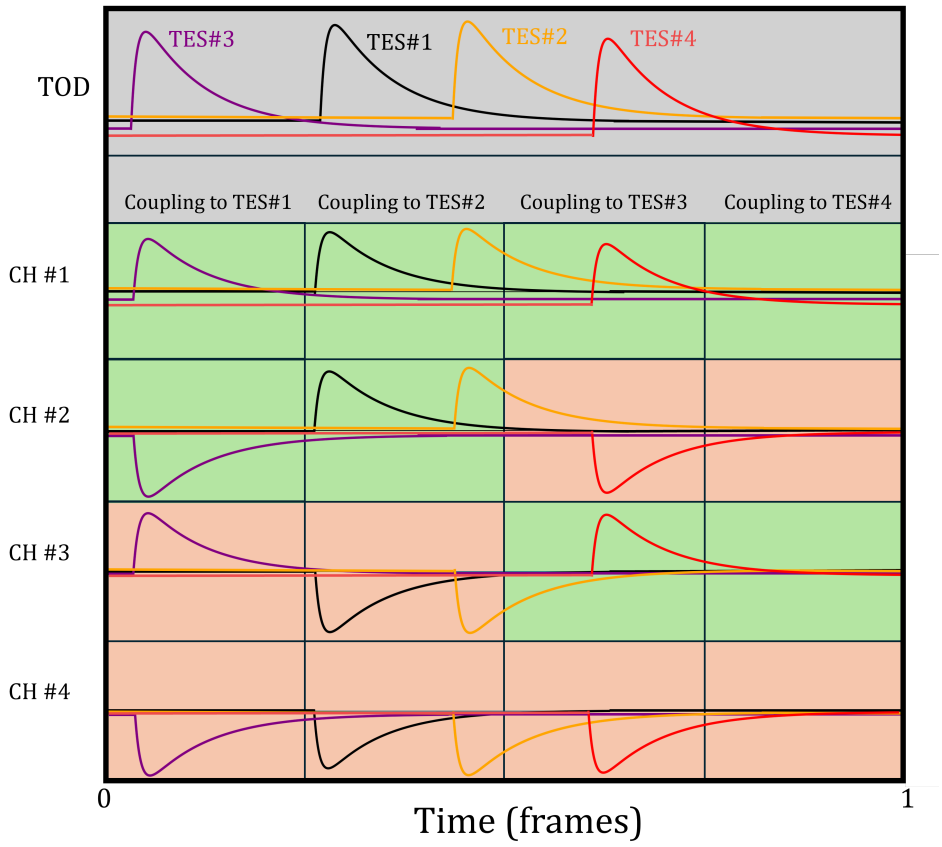


**Figure 15. Code Division Multiplexing scheme**. The top of the figure shows the TOD of four different pulses as produced by four TESs (TES#1, TES#2, TES#3, TES#4). Such signals are equally distributed across the four channels (CH#1, CH#2, CH#3, CH#4) with a polarity that is unique to each TES-Channel pair. The polarity is shown as different background color: green for positive and red for negative. The de-multiplexing is achieved by looking at the polarity combination of each pulse on the different feedlines and comparing it with a look-up table.

CDM with Flux Summation

The simplest way to achieve CDM is to sum the currents from $N$ TESs in $N$ different SQUIDs with different coupling polarities and then read them out sequentially with the use of a traditional TDM SQUID multiplexer. Going back to the two-TES example, this means that the sums of the currents arising from TES#1 and TES#2 are summed at the input of SQUID#1 and subtracted at the input of SQUID#2. In general, through a set of inductors, the fluxes thus produced are summed (with sign) into superconducting transformers that are then coupled to the individual SQUIDs as shown in Figure 16. Compared to current-steering CDM, flux summation is extremely straightforward but it comes at the expense of the complexity of the routing scheme and the size of lithographic elements.

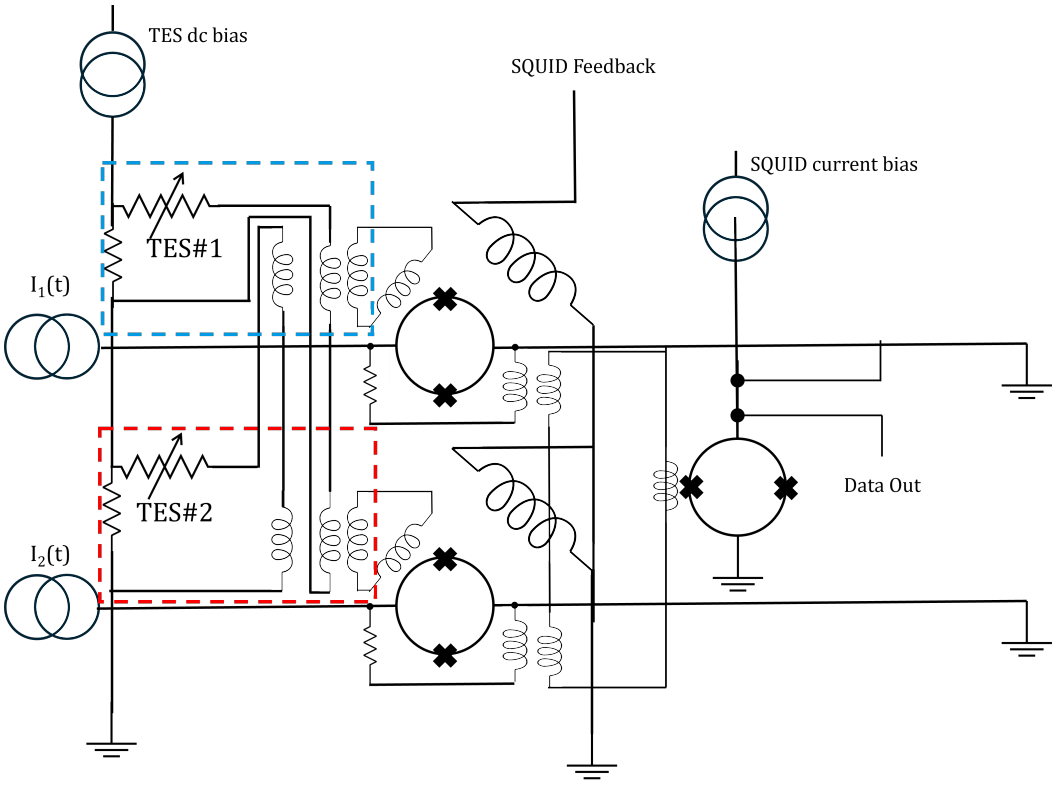


**Figure 16. Code Division Multiplexing**. In a simple 2-TES flux-summation scheme, the two SQUIDs are fed with the signal produced by the two TESs with alternate polarities. The two SQUIDs are alternatively read out on the 'Data Out' line.

CDM with Current Steering

Current steering CDM exploits a superconducting Single Pole Double Throw (SPDT) switch to modulate the polarity with which each TES is coupled to the SQUID amplifier. First, the bandwidth of signal from the TES is limited through an $L/R$ low-pass filter [66]; the signal thus limited is then modulated. The two arms of the SPDT are routed to contain a superconducting-to-normal (S-N) which is a low-inductance SQUID operated as a flux-controlled variable resistor. Furthermore, the second arm of the SPDT has an additional $\pi$ phase offset; thus, when no bias is applied to the SPDT, the SN#2 switch is off and SN#1 is on. In contrast, when SN1 is on, SN2 is off. In the first case, the signal is coupled with positive polarity, whereas in the second, the polarity is negative. When the polarity of each TES is switched, a back-action voltage is generated which has two main effects: acting as a source of cross-talk and producing an additional resistive component. Over a full frame, the cross-talk induced by the switching is null because of the ortho-normality of the Walsh vectors [66]. The extra resistance $R_s = L_{sw}/\tau_{sw}$ (where $L_{sw}$ is the parasitic inductance of the SN switch and $\tau_{sw}$ is the interval between two switching times) is in series with the bias voltage and needs to be small compared to the normal state resistance of the TES. Because the polarity modulation induced by the current-steering occurs at a frequency much larger than the bandwidth of the signal, no aliasing deteriorates the noise figure of the detector [66]. In principle, a hybrid scheme between current-steering and flux summation is possible and it involves coupling the signal from the TES into two superconducting transformers with opposite polarities and each branch is then switched on or off through SN switches. This last approach has the great advantage of reducing the number of address lines required to drive the commutation of the SN switches. Thanks to the periodic nature of the response of the SN switches, the number of address lines required to read out $N_{rows}$ of TESs is $log_2 N_{rows}$ [65]; this means that 256 rows of TES can be read out with only 8 address lines reducing dramatically the power dissipated in the cryostat and the thermal load.

3.7.4. Microwave Multiplexing (μ-MUX)

The biggest challenge of both TDM TESs and FDM TESs is the maximum achievable multiplexing factor which, for most practical implementations, is limited to less than 100. The development of other cryogenic detectors which operate at frequencies up to 8 GHz contributed to the development of ever-improving microwave electronics. Microwave multiplexing (μ-MUX) exploits the same working principle of FDM of coupling each TES to a resonant circuit with a unique resonance frequency and reading out each element in parallel by modulating and demodulating the signals produced by the TES at different frequencies. Such coupling, in the μ-MUX scheme, occurs through an RF-SQUID, one per each TES, that couples the current flowing through the TES to the resonance frequency of an LC circuit through local variations in magnetic flux [67]. All the resonating circuits are then coupled to the same coplanar waveguide (CPW) transmission line for their readout through the first amplification stage through a High Electron Mobility Transistor (HEMT) amplifier. Furthermore, there is often present a saw-tooth wave coupled to the RF-SQUID in order to up-convert the TES signal to higher frequencies in the 20 kHz range where the $1/f$ noise becomes negligible. A typical scheme for the implementation of microwave multiplexing can be found in Figure 17.

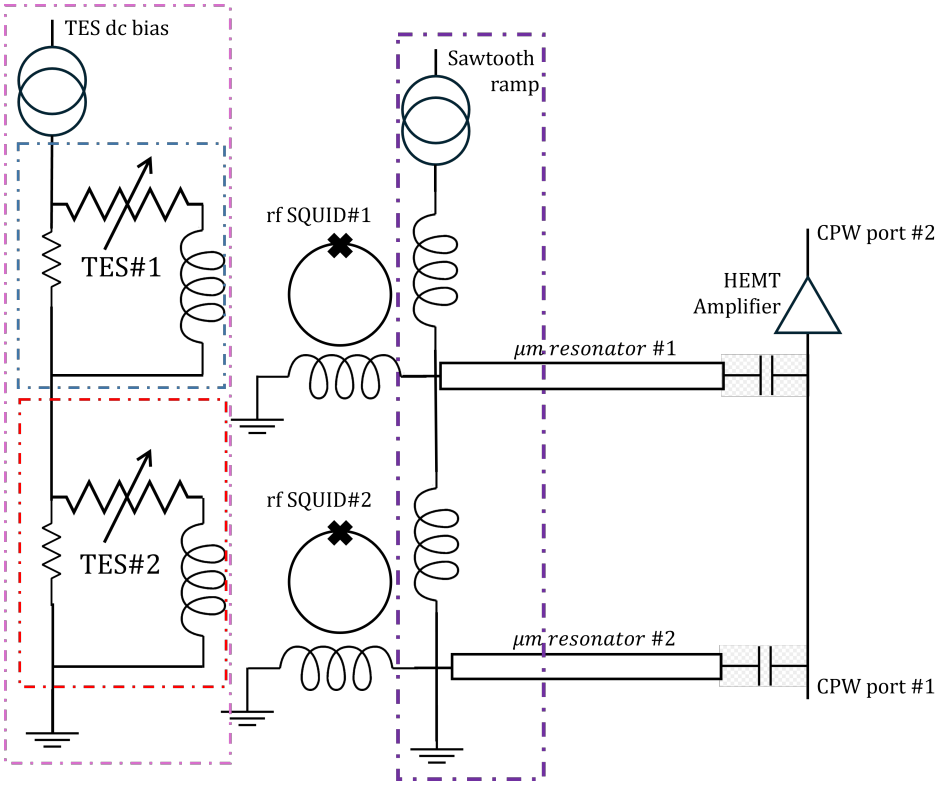


**Figure 17. Electronic schematic for the implementation of a 2-TES μMUX.** The section in the violet box represents the two TESs and their bias circuit. They are individually coupled to a microwave resonator through an RF-SQUID (blue box for #1 and red box for #2). The section in the violet box represents the saw-tooth wave used as a signal frequency up-converted.

In such a scheme, a multiplexing factor of up to 2000 can be achieved in the 4–8 GHz octave, where the 2 MHz spacing between adjacent frequencies is an optimum both for the readout electronics, and the fabrication of the multiplexer chip. Each resonant circuit has an estimated bandwidth of about 100 kHz and a depth of about 10–20 dB, which result in a quality factor of the resonators in the order of 40,000–80,000. In such a configuration, Dober et al. [68] demonstrated that the readout only contributes to less than 5% of the overall noise of the detectors with an input-referred current noise of 45 $\mathrm{pA}/\sqrt{\mathrm{Hz}}$ and a $1/f$ knee at about 20 mHz.

#### 3.7.5. Comparison

The previous section on different multiplexing techniques is rather difficult to follow without previous hands-on experience on TES detectors and quite some familiarity with SQUID amplifiers and transducers. Table 1 summarizes the main characteristics of the different multiplexing schemes. We hope such a table may help the reader choose the best option for the multiplexing of their TES array.

**Table 1. Comparison between different multiplexing schemes**. All values are intended to be typical unless differently stated.

| | **TDM** | **FDM** | **CDM** | **μ-MUX** |
|---|---|---|---|---|
| Complexity | ○ | ○○ | ○ ○ ○○ | ○ ○ ○ |
| Cost | ○ | ○○ | ○ ○ ○ | ○ ○ ○○ |
| Aliasing | Yes | No | No | No |
| Dead Time | Yes | No | Yes | No |
| Noise Level ($pA/\sqrt{Hz}$) | 10 | 10 | 19 | 45 |
| MUX factor | <128 | 32 | ∼100 | 2000 |

### *3.8. Noise Sources*

The main thermodynamical noise sources that affect TESs are the following: Johnson noise arising from both TES and load resistance; and thermal noise due to fluctuations in power transfer between the reservoir (at a temperature $T_R$) and the TES through the thermal link. One further noise contribution is introduced by both the cold (SQUID) and warm (amplification chain) readout electronics.

In addition to these intrinsic sources, TES bolometers exhibit photon noise, which arises from the fluctuation in the photon occupation number of the impinging radiation. Photon noise solely depends on the impinging radiation and not on the detector or its experimental setup and therefore cannot be further improved upon. For this reason, the desired noise level of a bolometer is comparable to or smaller than the photon noise of the source. A detector that operates in this regime is said to be photon noise limited.

For many practical applications, it is convenient to define the figure of merit commonly referred to as Noise Equivalent Power (NEP). NEP is defined as the signal power that must be applied to the TES in order to produce a signal which is equivalent to the measured noise. It can be calculated as the square root of the power spectral density (PSD) of the noise

$$NEP(\omega) = \sqrt{S_P(\omega)} \quad \left(\mathrm{W}/\sqrt{\mathrm{Hz}}\right). \tag{32}$$

In the next few pages, for the sake of clarity we will indicate the power spectral density $S_P(\omega)$ as $NEP^2(\omega)$. In general, it is fair to assume that the different noise sources are independent and uncorrelated; therefore, we can add in quadrature the different contributions and define a total noise equivalent power $NEP_{tot}$ as

$$NEP_{tot} = \sqrt{\sum_{i=1}^{n} NEP_i^2}. \tag{33}$$

Following the arguments presented throughout this review, we want to make a distinction between the case of a TES used as a bolometer and as a calorimeter. In the former, it is the low-frequency component of the noise $\left(\omega_{noise} \leq 1/(2\pi\tau_{eff})\right)$ that leaks into the signal band, whereas in the latter, the signal has a much wider band and therefore the noise components at much higher frequency feed into the signal. This is because the response function of a TES to an instantaneous absorption of energy by the calorimeter is formally identical to the noise associated with thermal fluctuations; therefore, their PSDs are identical in shape [69]. While the performance of a bolometer is defined by its $NEP_{tot}$, the performance

of a calorimeter is defined by its energy resolution, i.e., the smallest variation in energy it can measure. The maximum energy resolution achievable by a calorimeter, under the assumption that the noise that affects it is stationary, can be computed through an optimum filter and it can be computed following McCammon [69] as

$$\delta E_{FWHM} = 2\sqrt{2ln2}\left(\int_0^\infty \frac{4}{NEP_{tot}^2(f)}\,df\right)^{-1/2} \quad \text{(J)}. \tag{34}$$

3.8.1. Thermodynamic Fluctuation Noise

This component is associated with white shot noise due to the discrete energy carrier flow in the thermal link between the reservoir and the TES. An estimate of this noise can be made by considering the average energy fluctuation associated with a thermal capacity $C$ in equilibrium with a thermal reservoir with a temperature $T_R$, $\langle \Delta E^2 \rangle = k_B T^2 C$. Since shot noise is white, we can calculate the energy fluctuation as the integral over all frequencies of noise spectral amplitude by the response function of the weak conductive link and the thermal mass assembly (a low-pass filter with cutoff frequency, $f_c = 1/\tau$) [70]. Thus, we obtain that the power fluctuations propagating through the thermal link exhibit a spectral density given by

$$NEP_{tfn}^2 \simeq 4k_B T^2 G \quad \left(\text{W}^2/\text{Hz}\right). \tag{35}$$

This equation only stands if the reservoir and detector are in thermal equilibrium. Outside of equilibrium, it is necessary to consider the thermal gradient across the link; therefore, the two limiting cases have been found considering the two extreme cases whereby the energy carriers have a mean free path which is significantly larger than the length of the thermal link or much smaller. In the former case, according to Boyle and Rodgers Jr [71], the NEP can be computed as

$$NEP_{tfn}^2 = 4k_B T_R^2 G_0 \frac{t^{\beta_G+2}+2}{2}\left(\text{W}^2/\text{Hz}\right), \tag{36}$$

where $t = T/T_R$, $G_0$ is the thermal conductance at T = 0 K, $G = |\partial P_{link}/\partial T| \propto T^{\beta_G}$ [69]. In the latter, Mather [72] derived

$$NEP_{tfn}^2 = 4K_B T_R^2 G_0 \frac{\beta_G+1}{2\beta_G+3}\frac{t^{2\beta_G+3}+2}{t^{\beta_G+1}-1} \quad \left(\text{W}^2/\text{Hz}\right) \tag{37}$$

with the aforementioned nomenclature.

3.8.2. Johnson Noise

Johnson noise [73] is due to both voltage fluctuations across the bias resistor and across the TES. For a general resistor, these voltage fluctuations exhibit a power spectral density given by [74]

$$S_V = 4k_B T R \quad \left(\text{W}^2/\text{Hz}\right). \tag{38}$$

Since the TES is in NTEF, we must consider its effect when discussing the effects of both sources. In the case of voltage fluctuations generated by the bias resistor, the TES produces current signal as a response to the voltage change according to the electrical admittance of the TES [38]

$$Y_{ext} = S(\omega) I_0 \frac{\mathcal{L}-1}{\mathcal{L}}(1+i\omega\tau_I) \quad \text{(A/V)}, \tag{39}$$

where $S(\omega)$ is the responsivity of the TES, $\mathcal{L}$ is the loop-gain, and the time constant of a current-biased TES reads [38]

$$\tau_I = \frac{\tau}{1-\mathcal{L}}. \tag{40}$$

The NEP can be calculated by multiplying the voltage Johnson noise of the bias resistance by Equation (39) and dividing it by the responsivity of the TES according to Irwin and Hilton [38]

$$NEP^2_{P_{R_{bias}}}(\omega) = 4k_B T_{bias} I_0^2 R_{bias} \frac{(\mathcal{L}-1)^2}{\mathcal{L}^2}(1+\omega^2\tau_I^2) \quad \left(\mathrm{W}^2/\mathrm{Hz}\right), \tag{41}$$

where $T_{bias}$ is the electronic temperature of the bias impedance. Whereas the voltage Johnson noise arises across the resistance of the TES, the Joule power generated is dissipated differently through the TES with respect to the previous scenario; hence, Irwin and Hilton [38] computed the Johnson NEP as

$$NEP^2_{P_{TES}}(\omega) = 4k_B T I_0^2 R_{TES} \frac{\xi(I_0)}{\mathcal{L}_I^2}(1+\omega^2\tau^2) \quad \left(\mathrm{W}^2/\mathrm{Hz}\right). \tag{42}$$

In addition, in order to account for the non-linearity in the voltage drop across the superconductor which is due to a $\Delta R$ induced by a change in the current flowing through it, we must include a factor ($\xi$)

$$\xi(I) = 1 + 2\beta_I, \tag{43}$$

where $\beta_I$ is the logarithmic derivative of the TES resistance with respect to the current flowing through it and defined as $\beta_I = \frac{dR}{dI}\frac{I}{R}$.

#### 3.8.3. Readout Noise

The main contribution to the noise in the readout chain usually arises from the SQUID amplifier. For most commercial applications, the current equivalent noise at its input coil $i_{n_{SQUID}}$ $\left(\mathrm{A}/\sqrt{\mathrm{Hz}}\right)$ is provided by the manufacturer. In order to obtain its NEP, we can divide $i_{n_{SQUID}}$ by the detector responsivity

$$NEP^2_{SQUID} = \frac{i_{n_{SQUID}}(\omega)^2}{S(\omega)^2} \quad \left(\mathrm{W}^2/\mathrm{Hz}\right). \tag{44}$$

If well designed, the noise produced by the cold-amplification stage dominates over the noise introduced by any other element further down the readout chain. Typically, the voltage noise $e_n$ of an operational amplifier operating at room temperature is of the order $1\ \mathrm{nV}/\sqrt{\mathrm{Hz}}$. Such an operational amplifier exhibits a current noise $i_n \sim \mathrm{pA}/\sqrt{\mathrm{Hz}}$ coming out of its input terminals. If the SQUID exhibits a dynamic resistance $R_{dyn} \sim 100\ \Omega$ (which is typical for SQUID arrays with gain of a few hundred V/A), the interplay between the noise current and the dynamic resistance of the SQUID becomes non-negligible and it induces a voltage drop across the SQUID amplifier. Under these conditions, the NEP generated from the warm readout becomes

$$NEP^2_{wr}(\omega) \simeq \frac{(e_n(\omega)^2 + i_n(\omega)^2 R^2_{dyn})}{Z^2_{tran} S(\omega)^2} \quad \left(\mathrm{W}^2/\mathrm{Hz}\right). \tag{45}$$

#### 3.8.4. Photon Noise

As previously discussed, the photon noise can be regarded as a noise floor which is only dependent on the detected radiation and not on the detector nor on its readout chain. It sets a fundamental limit to the sensitivity of any detector. It includes two terms [75]

$$NEP^2_{opt} = 2h\nu P_{opt} + \zeta \frac{P^2_{opt}}{\delta\nu} \quad \left(\mathrm{W}^2/\mathrm{Hz}\right), \tag{46}$$

where $\nu$ is the band center of the detected radiation, $\delta\nu$ is the detection bandwidth, $P_{opt}$ is the total optical power and $\zeta$ is called the bunching factor [76] and ranges between 0 and 1 and its nature will be discussed later.

The first term is simply due to the photon shot noise and derives from the simple counting of the number of photons with given energy per unit time, whereas the second term arises from the fact that photons are bosonic in nature and tend to distribute their energies according to Bose–Einstein's distribution. In general, it is possible to state, with good measure, that $0.3 \leq \zeta \leq 0.6$ [76].

#### 3.8.5. Excess Noise

In the last few years, a number of research groups have reported noise figures with components that exceed the ones we have just discussed. In most cases, such excess noise appears at high frequency, in the proximity of the roll-off frequency of the TES [76]. Such components appear to be correlated with the steepness of the superconducting-to-normal transition and the a-dimensional derivative $\alpha$ and it seems to improve if $\alpha$-mitigation strategies are put in place [77,78]. Furthermore, there is anecdotal mention of this effect being exacerbated by inhomogeneities in the superconducting film, but the published data are scarce [76].

Excess noise in X-ray calorimeters has been widely studied since Galeazzi [79] and can be attributed to two different effects:

- **Flux Flow Noise** is due to trapped magnetic field lines that create a vortex in the superconductor. A vortex is free to move on the surface of the superconductor and while doing so, it generates a voltage drop. The noise term arising from flux flow can be written as $\sqrt{\phi_0 \frac{IR_{ff}}{1+\frac{IR}{V_0}}}$ where $\phi_0$ is the magnetic flux quantum, $I$ is the current flowing through the TES $R_{ff}$ and $V_0$; the latter represents the voltage above which the noise saturates ($V_0$), whereas the former is only a coefficient with units of Ohms.
- **Internal Thermal Fluctuation Noise** arises from the finite thermal conductance in the TES film. Different segments of the film may exhibit a different temperature simply because of geometrical and physical properties of the TES and the point where the TES is struck. These thermal fluctuations can lead to an extra noise component. Accounting for internal thermal fluctuations, noise allows one to scale the simple one-conductance approximation of a TES to a more realistic description of the detector.

It is worth mentioning that in addition to this excess noise, there is a well known effect that arises in a TES when the heat capacity of the thermal link to the reservoir becomes comparable with the heat capacity of the TES itself. An in-depth discussion can be found in Gildemeister et al. [80].

#### 3.8.6. Noise Comparison Between Different Multiplexing Schemes

It is obvious that different multiplexing schemes, such as those presented in Section 3.7, exhibit different noise levels and some extra contributions which are inherent to the multiplexing architecture may appear. In this section, we will address the aforementioned noise sources and we will discuss how they interplay with different readout schemes.

In general, wide-band noise from the SQUID is added to the signal after it is encoded and such noise is then filtered out during decoding [38]. The noise that is added during the encoding strongly depends on the bandwidth of the encoded signal.

- **Time Division Multiplexing:** In TDM, the encoding occurs through a modulation of the signal with a boxcar that represents the switching between different TES channels. Each pixel is read out for a 'time-frame' which has a rate of $1/N\delta t_s$, where $N$ is the multiplexing factor and $\delta t_s$ is the time span for which the multiplexer dwells on one pixel [38].

  The noise components with a frequency above the Nyquist frequency associated with the frame rate $f_{Low} = 1/(2N\delta t_s)$ is embedded in the signal. Any noise above the boxcar Nyquist frequency is aliased and averages out $f_{High} = 1/(2\delta t_s)$. The NEP of the SQUID is thus increased by a factor $N$ and therefore the gain of the SQUID needs to be tuned to be $N$ times larger than that of a non-multiplexed SQUID in order to retain the same SNR [38].

- **Frequency Division Multiplexing:** In an FDM scheme, two phenomena can occur: (i) noise sources can modulate the amplitude of the carrier tones and (ii) noise leakage in the band of the carrier tones. Category (i) includes photon noise and thermal fluctuation noise. These sources are accounted in an analogous fashion to a single TES biased in DC. Category (ii) includes Johnson noises and readout noises. The current signal that these sources contributes must be multiplied by a factor $\sqrt{2}$ as shown by Dobbs et al. [81] in order to take into account the AC bias of the TES. Similarly, the responsivity of the detector also includes a $\sqrt{2}$ factor (Equation (31)) which leaves the NEP unchanged. Furthermore, Lueker et al. [82] found that the effects of NETF on Johnson noise sources when the TES is DC biased (Equations (41) and (42)) also apply when the TES AC was biased (besides from the aforementioned $\sqrt{2}$ factor).
- **Code Division Multiplexing:** In a CDM scheme, the TESs are all effectively Frequency Domain Multiplexed, therefore the same consideration apply except their outputs are split and sent to the input coils of several SQUIDs with different polarities.
- **μ-MUX:** Effectively, for μ-MUX, all the previous considerations observed about FDM TESs hold true. Except, the SQUID noise component needs to be replaced by the far more detrimental noise figure of a HEMT [83,84] and the NEP of an RF-SQUID [85] needs to be added in quadrature to the total NEP $NEP_{tot}$.

### *3.9. Cross-Talk*

Cross-talk is a known issue of detector arrays where multiple pixels are read out simultaneously. A large number of mitigation strategies can be put in place, but overall inter-pixel cross-talk cannot be fully eradicated. In FDM, and likewise for CDM, a cross-talk occurs between the frequency channels. Different types of cross-talk arise from the LC filter configuration. Four major cross-talk effects can be measured according to Dreyer et al. [64] and Mates et al. [86]: the electro-magnetic coupling between the inductors, the coupling between the oscillators, the carrier current leakage and the common impedance.

The first term is related to the mutual inductance coupling $M_{ij} = k_{ij}L_iL_j$ between two inductors of self inductance $L_i$ and $L_j$. The current flowing in the $i$-th leg $I_i(\omega_i)$ can induce a voltage drop $V_j = \omega_i M_{ij} I_i(\omega_i)$ at the ends of a coupled inductor [81]. This term can be eliminated or optimized by maximizing the physical distance between LC resonators which are neighbours in frequency space.

One further cross-talk mechanism is due to the physics of tightly packed weakly coupled oscillators [87,88] and has to do with the hybridization of the individual resonance frequencies which through this interaction repel each other. Further details are discussed by Mates et al. [86], who evaluate this cross-talk component as

$$\chi = \frac{16f^4}{(f_2 - f_1)^2} \frac{M_{12}^2}{Z_0^2}\,, \tag{47}$$

where $f_1$ and $f_2$ are the two resonance frequencies of the two RLC channels, which are rather close in frequency; hence, $f \sim f_1 \sim f_2$, $M_{12}$ is the mutual inductance and $Z_0$ is their impedance. This cross-talk effect scales with the square of the magnetic coupling $M_{12}$ and inversely with the square of the frequency separation. Therefore, it can be mitigated by both separating the coupled oscillators both in space and in frequency. The carrier current leakage is an unavoidable form of cross-talk. It occurs because two LC filters, in frequency space, are described by two resonance peaks (described by two Lorentzian curves, see Figure 18b), the tails of which necessarily overlap. The overlap of such ends represents the fraction of electrical power that the two resonators share. This cross-talk component describes the modulation of the current flowing through one single RLC channel when the resistance in one of the frequency-neighbouring branches varies. This effect can only be mitigated by only increasing the frequency distance between the multiplexing frequencies

within the limits given by the bandwidth. For a generic j-th branch, the off-resonance current is defined as

$$I_j(\omega_i) = \frac{V_{bias}(\omega_i)}{R_{TES,i} + i\omega_i L_j + 1/(i\omega_i C_j)} \,. \tag{48}$$

The cross-talk is due to the variation in this current $I_j(\omega_i)$ when the resistance $R_i$ varies: $\Delta I_j(\omega_i)/\Delta R_i$ [81]. The off-resonance component is infinite, in the ideal scenario, but for most practical applications it needs to be considered finite, and therefore the current $I_j$ described by Equation (48) is finite.

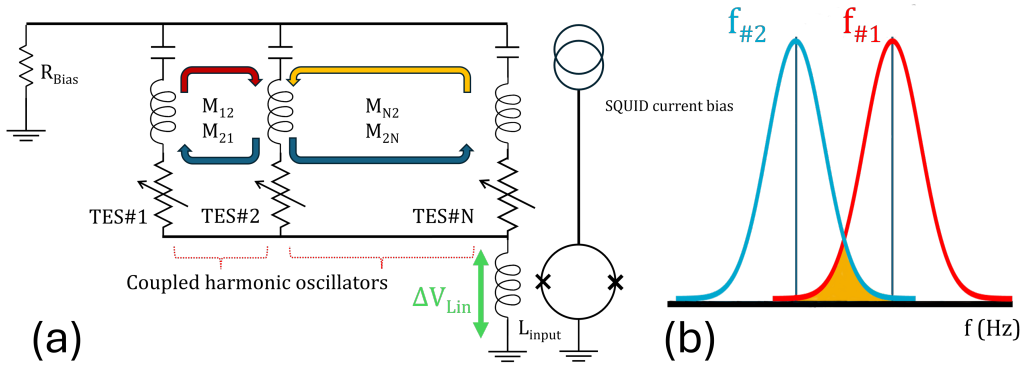


**Figure 18. Cross-talk scheme in FDM.** (**a**) Schematic of $N$ frequency division multiplexed TESs with the different cross-talk components: (i) the mutual inductance between different channels, (ii) the coupled oscillators, (iii) the voltage drop due to the shared input impedance. (**b**) The cross-talk term due to to the overlap of the Lorentzian—shown as Gaussians for simplicity. The area shaded in orange represents the cross-talk.

The common impedance term is linked to the presence of the wiring and of a preamplifier such as a SQUID. The modulation of the current at the frequency $\omega_i$ causes the modulation of the current flowing through the input coil of the SQUID, which in turn causes the modulation of the current in all the neighbouring branches [81].

In a rather similar fashion, the inter-pixel cross-talk in μ-MUX multiplexing schemes deals with the electromagnetic coupling between different harmonic oscillators. In μ-MUX schemes, some of the same coupling mechanisms already discussed for FDM apply: the widely discussed mutual electro-magnetic coupling between the inductors of different channels, the innate effects of the coupled harmonic oscillators and the overlap of the Lorentzian tails of the resonance shapes. In addition to these, we must consider the non-linearity of the microwave components which act on the superposition of the channel tones and result in a weak mixing of the tones [86]. In particular, it is worth stating that while other cross-talk components fall off quite quickly with physical distance and frequency spacing, this last cross-talk component does not and therefore it sets an effective cross-talk floor. In principle, it can be mitigated by an accurate selection of the microwave components, and by driving the resonators at lower powers in a trade off between SNR and cross-talk. Potentially, a tone-tracking readout [68] could also reduce the effects of such a cross-talk component [89].

As a rule of thumb, it is good practice to space the resonators in frequency by at least 10 times their line width in order to effectively reduce the effect of the overlap of the Lorentzian tails [86]. The final contribution to cross-talk that still needs to be addressed is the contribution arising from capacitive and inductive coupling between different transmission lines which carry the FDM signals. Unfortunately, these strongly depend on a case-by-case basis and are severely influenced by the geometry of the problem. Generally, it is always good practice to keep the transmission lines as far apart as possible and include a ground plane in between each two different transmission lines.

## 4. Applications in Astronomy and Astrophysics

Despite that the original development of Transition Edge Sensor micro-calorimeters was not intended specifically for astronomical purposes, TESs find a plethora of applications in the field of astronomy: ranging from high-energy $\gamma$-ray astronomy to cosmological application at extremely low energies such as the investigations of the polarization modes of the cosmic microwave background (CMB). Their large bandwidth coupled with the excellent energy resolution make TES promising detectors for most applications. Furthermore, TESs can be optimized in order to be single-photon sensitive across a wide spectrum and can also be operated as bolometers (coupled with lenses, feed-horns or antennas) at lower energies. In this section, we will discuss some of the most prominent applications of TESs in the field of astronomy.

### *4.1. X-Ray Astronomy*

#### 4.1.1. ESTREMO/WFXRT

ESTREMO/WFXRT was a proposed mission for the ESA Cosmic Vision Programme 2015–2025 [90,91]. This was a spacecraft mission for observation of very high-energy events such as gamma-ray bursts (GRBs) which often also exhibit an X-ray afterglow which can be detected directly from the ESTREMO/WFXRT detectors. The importance of GRBs is that they can be studied to extract information on the first population of luminous sources ignited in the dark universe at high redshift $z > 7$. Furthermore, GRB measurement can help determine the cosmic history of metals in star-forming regions with metal absorption and edges while also allowing the probing of the Warm-Hot Interstellar Medium (WHIM) properties through high-resolution absorption studies. Observing WHIM can allow the identification of the missing baryonic matter. Dark Matter (DM) baryons are heated up to X-ray-emitting temperature $10^5$–$10^7$ K. Thus, X-ray observations play a fundamental role in the indirect measurement and characterization of DM.

While the configuration of the payload and the instruments on board the ESTREMO/WFXRT were never finalized, two main instruments were envisioned: the Wide Field Instrument (WFI) and the Narrow Field Instrument (NFI). The first of which spans energies between 2 and 200 keV in order to catch X-ray Flashes (XRF) and galactic transients and supposedly would have developed CdZTe detectors. The NFI, instead, would have either deployed only TESs or a mix of Charge Coupled Devices and TESs. In any case, the desired energy resolution of such TESs would have been of 1 eV at 1 keV.

#### 4.1.2. Athena X-IFU

The Advanced Telescope for High-Energy Astrophysics (*Athena*) is an ESA space-borne X-ray observatory in the energy range 0.2–12 keV [92]. The main scientific goals of *Athena* involve the study of highly energetic processes in space such as the physical and chemical properties of hot plasmas, such as those found in galaxy clusters and the study of black hole accretion disks with their jets, outflows and winds. It will also be able to perform measurements on exoplanets, stars, supernovae and interstellar mediums.

*Athena* will exhibit an angular resolution of 5″ for its two main instruments the Wide-Field Imager [93] and the X-ray Integral Field Unit (X-IFU) [92]. *Athena* X-IFU is a spatially resolved spectrometer with a field of view of 5′ and an energy resolution of 2.5 eV at 10 keV [94]. The focal plane consists of 3840 Mo/Au TESs [95] with an Au/Bi absorber with an expected NEP below $10^{-17}$ W/$\sqrt{\text{Hz}}$. Furthermore, located 1 mm underneath the main TES array, there is an Ir/Au TES-based cryogenic anti-coincidence detector (CryoAC) [96] to reject the non X-ray-induced events to a rate below $5 \times 10^{-3}$ counts/s/cm$^2$/keV in the 2–10 keV range. The X-IFU TESs are multiplexed in an FDM scheme with a multiplexing factor 40:1 [97] allowing for the complete readout of the TES array with 96 channels [96].

#### 4.1.3. Lynx X-Ray Observatory

The Lynx X-ray Observatory (*Lynx*) is a NASA-funded concept study for future missions with a proposed launch date of 2036 [98]. If launched, *Lynx* will have similar scientific

goals to *Athena*. It will, in fact, investigate the birth and the evolution of supermassive black holes, observing in the X-ray high-redshift black holes (z $\sim$ 10) with a mass a few thousand times that of our sun. Furthermore, *Lynx* will allow a large survey of black holes at redshifts $z$ = 2–6 to investigate whether all massive black holes emerge at $z \leq 6$ or whether some low-mass black holes have developed at lower redshift [99].

*Lynx* will be capable of addressing several open questions in the field of star formation. In conjunction with infra-red data from other telescopes, *Lynx* with its census of star-forming regions in the X-rays will contribute to a better understanding of circumstellar grain growth, and will help investigate the magnetic and non-gravitational effects in proto-planetary discs. Furthermore, X-ray imaging spectroscopy will revolutionize the field of Supernovae Remnants science, providing three-dimensional spectroscopic images of metals synthesised in the explosions. The full list of scientific goals of *Lynx* can be found in its concept study paper [100].

The Lynx X-ray Observatory will have a primary mirror with a diameter of 3 m and will be equipped with three main instruments: the High-Definition X-ray Imager (HIXI) [101], the *Lynx* X-ray Microcalorimeter (LXM) [98] and the X-ray Grating Spectrometer (XGS) [102]. While HIXI is a wide-field high imager with high spatial resolution, the spectroscopic measurements are performed with the LXM (with a resolving power R $\sim$ 2000 in the 0.2–7 keV range) and the XGS (R $\sim$ 5000–7500 in the 0.2–2 keV range). In particular, the *Lynx* X-ray Microcalorimeter will consist of a 100,000 TES array with energy resolution of 2 eV up to 7 eV and 0.3 eV in the 0.2–0.75 keV range [103].

### *4.2. Infrared Astronomy*

#### 4.2.1. Origins Space Telescope

The NASA flagship mission Origins Space Telescope (*Origins*) proposed for launch in 2035 is the largest spacecraft-borne mission so far with a mirror size of 5.9 m in diameter and a spectral sensitivity ranging from 2 µm to 588 µm [104]. The current mission goals for *Origins* [105] include the study of galaxy formation, planet formation and the evolution of supermassive black holes. In particular, the scientific interest lies in the generation of metals, dust and organic molecules and how pulsars and supernovae affect the interstellar medium. A second topic of interest is planet formation and the development of habitability: in particular for Earth and Earth-like exoplanets, how were water and other life's ingredients delivered to such planets? Finally, *Origins* aims to perform transition spectroscopy of K- and M-Dwarf planets to investigate which, if any, exhibit the conditions necessary for habitability. *Origins* is expected to produce a broader and clearer picture on dwarf planet habitability than JWST [105].

*Origins* will be equipped with three main instruments: the Origins Survey Spectrometer (OSS) [106] which will allow the observation of emission lines between 25 µm and 588 µm and probe galaxy evolution up to $z \sim 8.5$. By design, OSS requires detectors with an NEP $\sim 3 \times 10^{-20}$ W/$\sqrt{\text{Hz}}$ and a saturation power of 0.2 fW. The Far-infrared Imager and Polarimeter (FIP) [107] will perform wide field polarimetric observations of astrophysical objects bridging the energy gap between ALMA (Atacama Large Millimeter/submillimeter Array) and JWST. Its detectors are less challenging with a required NEP $\sim 3 \times 10^{-19}$ W/$\sqrt{\text{Hz}}$ and a saturation power of 20 fW. Finally, the Mid-Infrared Spectrometer Camera Transit (MISC-T) [108] will be responsible for the transit spectroscopy of exoplanets including K- and M-Dwarf planets. MISC-T will have a resolving power $R < 300$ and for it TES in both the calorimetric and bolometric use are being investigated despite a strong suggestion towards their use as calorimeters [109].

#### 4.2.2. SPICA-SAFARI

SPICA (Space Infrared Telescope for Cosmology and Astrophysics) was a medium-class spacecraft mission proposed to ESA and cancelled in 2021. Like the Origins Space Telescope, SPICA intended to bridge the gap in energies between the observational capabilities of ALMA and JWST [110]. SPICA was intended to perform spectroscopy between

20 μm and 230 μm. Its scientific goals were aligned with the proposed science that will be performed with *Origins*: galactic formation and evolution, black hole evolution and studies on metallicity in dust-covered galaxies and active galactic nuclei. SAFARI, the Spica FAR-infrared instrument [111], was proposed as a spectrometer between 30 μm and 210 μm with an NEP $\leq 3 \times 10^{-19}$ W/$\sqrt{\text{Hz}}$ with a saturation power of 1 fW [112]. SAFARI was intended to sport 3600 FDM [113] Ti/Au TESs with a critical temperature of 155 mK suspended on a 1 μm SiN membrane [114]. Despite substantial progress being made toward the development of ultra-low noise TESs [114,115], ESA decided not to move forward with SPICA as its next medium-class mission.

### *4.3. Millimetre and Sub-Millimetre Astronomy*

#### 4.3.1. SCUBA-2

SCUBA-2 (Submillimetre Common-User Bolometer Array 2) is a dual-band TES camera operating at 450 and 850 μm with 10,000 TES bolometers on the focal plane read out in a TDM scheme [116]. The Transition Edge Sensors, developed by NIST, are Mo/Cu with a critical temperature of 130 mK for the TESs in the 850 μm band and, in order to account for higher optical powers in the sky, the TESs in the 450 μm band were designed with a critical temperature of 190 mK in mind. All the sub-assemblies of SCUBA-2 exhibited a dark NEP in the range 1.6–3.2 $\times 10^{-16}$ W/ $\sqrt{\text{Hz}}$ and a saturation power ranging between 87 and 541 pW [117,118].

Ground-based sub-mm observations are meant to explore the cold universe by investigating dust and gases in the early stages of galaxy, star and planet formation. At such wavelengths, the dust continuum is effectively optically thin and therefore it is possible to observe the critical processes that occur during galaxy/star/planet formation. The commissioning of the instrument, deployed on the James Clerk Maxwell Telescope, involved the characterization of selected galaxies with SCUBA-2 at both 450 and 850 μm and was reported by Casey et al. [119]. A review with the main scientific achievement of SCUBA-2 in its first decade (2011–2021) was published by [120]. In 2023, SCUBA-2 performed a full extra-galactic survey at 850 μm [121] with an unprecedented angular resolution of 14 arcseconds, which is a survey over three orders of magnitude more detailed compared to the previous survey at the same wavelengths (COBE) [122].

#### 4.3.2. GISMO

The Goddard IRAM Superconducting Millimeter Observer (GISMO) was a guest instrument at the IRAM 30m telescope operating between 2012 and 2014. GISMO consisted of one single TES focal plane with 128 pixels (8 × 16) in a TDM configuration [123]. The TESs that constituted the focal plane of GISMO were designed with an operating temperature of 400 mK that could be reached in the $^3$He/$^4$He evaporation cryostat and exhibited an NEP $4 \times 10^{-17}$ W/$\sqrt{\text{Hz}}$. GISMO also exhibited a bandpass filter with 25 GHz bandwidth about its maximum at 150 GHz (2 mm). The GISMO 2 mm survey [124] provided valuable information on the bright end of the infrared luminosity function and the massive end of the dust mass function at $z \sim 4$ for rare massive high-redshift highly star-forming galaxies. The work GISMO carried out paved the way for the observations of ALMA 2 mm continuum survey [125].

### *4.4. Cosmic Microwave Background*

#### 4.4.1. CLOVER

CLOVER was a project funded by the Science and Technology Facilities Council (STFC) of the United Kingdom and lead by the universities of Cambridge, Cardiff, Manchester, and Oxford [126–128]. Its main goal was the observation of primordial B-mode polarization of the CMB radiation with a sensitivity equivalent to a tensor-to-scalar ratio $r \geq 0.01$. CLOVER consisted of three separate instruments operating at 97, 150 and 220 GHz to provide discrimination between the CMB and foregrounds [129]. Each instrument would have deployed NIST TES polarimeters coupled to feed-horns which act as band-pass

filters and focusing elements. Each polarimeter consists of a Mo/Cu Transition Edge Sensor with an NEP of $1.5\times10^{-17}$, $2.5\times10^{-17}$, and $4.5\times10^{-17}$ W/$\sqrt{\text{Hz}}$, respectively, in each band [130,131]. Despite its ambitious goals and promising science goals, the project was not funded to completion.

#### 4.4.2. Atacama Cosmology Telescope

The Atacama Cosmology Telescope (ACT) was a telescope in the Atacama desert in Chile specifically designed for cosmological observations of the CMB operational between 2007 and 2022 [132]. During its life span, it sported three main instruments, the Millimetre Bolometer Array Camera (MBAC) [133,134] and its two upgrades, ACTPol [135] and Advanced ACTPol (AdvACT) [136]. ACT has provided the scientific community with extremely important results, among which are the first detection of gravitational lensing in a CMB map by Das et al. [137] and the discovery of the El Gordo galaxy cluster (ACT-CL J0102-4915) [138]. All instruments have ACT mounted Transition Edge Sensors as the sensitive element. MBAC comprises three TES arrays in the frequency bands 145, 220 and 280 GHz. Each array contains 32 × 32 detectors read out in a TDM scheme. The superconducting elements of the detectors are Mo/Au bilayers tuned so as to achieve a critical temperature of 0.5 K and a measured NEP below $8\times10^{-17}$ W/$\sqrt{\text{Hz}}$ [139].

The first upgrade to MBAC, ACTPol, consists of three polarization-sensitive arrays, PA1 and PA2 which operate at 148 GHz, while PA3 operates both at 97 and 148 GHz [135]. Each polarimeter is coupled to a feed-horn, except for PA3 which has 4 polarimeters per feed-horn, one in each band. Combined, there are 1279 feed horns and 3068 detectors in the ACTPol instrument. Each TES is constituted of a Mo/Cu bilayer with a critical temperature of 150 mK and an NEP below $2.0\times10^{-17}$ W/$\sqrt{\text{Hz}}$ and a saturation power of about 10 pW [140].

The final upgrade to ACTPol, AdvACT, produced a map of the sky in five bands between 28 and 230 GHz [141,142]. The AdvACT TESs are fabricated from single-layer Al/Mn films [143] instead of bilayer Mo/Cu films as in ACTPol with a critical temperature of 160 mK and an NEP below $2.0\times10^{-17}$ $W/\sqrt{\text{Hz}}$ [135,144,145]. The final constraint set by the ACT on the tensor-to-scalar ratio was published by Galloni et al. [146] and it currently is $r \leq 0.03$.

#### 4.4.3. ABS

The Atacama B-mode Search (ABS) was both an experiment and an instrument operating at 145 GHz [147]. As per its name, it was deployed in the Atacama desert of Chile and its main purpose was the measurement of B-mode polarization of the CMB and especially the determination of the tensor-to-scalar ratio of the primordial B-mode components. The receiver of ABS consists of 240 feed-horn coupled polarimeters [148]. Each polarimeter consists of a planar orthomode transducer (OMT) that couples the orthogonal polarization components of light to two different TESs for detection and measurement [149]. The detectors are produced by NIST and are designed to operate at 300 mK in a $^3$He/$^4$He adsorption refrigerator. The upper limit ABS set for the tensor-to-scalar ratio was $r \leq 2.3$ with a 95% confidence level [150].

#### 4.4.4. BICEP

The Background Imaging of Cosmic Extragalactic Polarization (BICEP) along with the Keck Array are a series of experiments on the CMB polarization deployed in Antarctica [151]. During the years, the experiments have evolved and were upgraded from BICEP to BICEP2 [152], the Keck Array [153], BICEP3 [154] and eventually the BICEP Array [155]. The first generation of BICEP (2006–2008) used NTD Ge thermistors as detectors [156], but the choice quickly moved to TESs starting from BICEP2 (2010–2012), which sported 500 Ti TESs coupled to 150 GHz radiation. The TESs exhibited a critical temperature of about 450–500 mK and an NEP of 5–6 $\times$ $10^{-17}$ W/$\sqrt{\text{Hz}}$ [157]. During the lifespan of BICEP2, the Keck Array which consists of five BICEP2-class receivers sharing the same

mount was developed. The Keck Array is also sensitive to radiation in different frequency bands (95, 150 and 220 GHz). The data from the Keck Array alone set an upper limit to the tensor-to-scalar ratio $r < 0.09$ at 95% confidence level, which was further reduced to $r < 0.07$ when combining the Keck Array observations with external datasets [153,158].

BICEP 3 is the latest BICEP Telescope with 2560 TESs measuring radiation in the 95 GHz band. The detector technology was not upgraded between BICEP2 and BICEP3, but the number of detectors on the focal plane was increased over 5 fold.

The Keck Array has been replaced by the BICEP Array which consists of four BICEP3-like receivers operating in the 30/40, 95, 150 and 220/270 GHz bands [155].

#### 4.4.5. CLASS

The Cosmology Large Angular Scale Surveyor (CLASS) is an array of microwave telescopes for CMB studies, including the detection of primordial B-mode polarization [159]. CLASS is designed as follows: it exhibits one focal plane with 36 detector pairs operating at 38 GHz, two focal planes with 259 detector pairs each operating at 93 GHz, and a dual-band telescope with 1000 detector pairs at each of 148 and 217 GHz [160–162]. Each detector consists of a feed-horn coupled to an OMT coupled to two Mo/Au TESs with a critical temperature of 150 mK and an NEP of $2.1 \times 10^{-17}$ W/$\sqrt{\text{Hz}}$ [163,164]. CLASS is currently in operation, carrying out a survey of 70% of the sky from which it will not only infer the value of the tensor-to-scalar ratio, but also carry out new physics while investigating both the Milky Way galaxy and the circular polarization of CMB.

#### 4.4.6. SPT

The South Pole Telescope (SPT) is a 10 m diameter off-axis Gregorian Telescope designed to observe the CMB from Antarctica in order to study its anisotropies. In particular, the SPT first observed B-mode polarized CMB radiation (albeit not being primordial). Three main instruments have been deployed at the SPT since its commissioning: the SPT-SZ camera with 960 TDM TESs sensitive in bands about 95, 150 and 220 GHz [165]. The main science goal of the SPT-SZ camera was a large-area survey of the Southern Sky. The second camera mounted on the SPT was the SPTPol (SPT-Polarimeter) with 1560 Transition Edge Sensors in a polarimeter configuration with a feed-horn, an OMT and two TESs, one per each polarized component of the light. The 780 polarimeters were divided in two frequency bands: 90 and 150 GHz [166]. The third generation camera, SPT-3G, was installed in 2018 with 16000 detectors on the focal plane, split evenly between 90, 150 and 220 GHz [167–169].

#### 4.4.7. POLARBEAR

The polarization of the background radiation (POLARBEAR) is an experiment set in the Atacama desert of Chile and it aims at measuring the B-mode polarization component of the CMB radiation [170]. The POLARBEAR array consists of 637 polarization-sensitive pixels for a total of 1274 antenna-coupled TES bolometers. The TESs are made of Ti/Al bilayers with a critical temperature of about 500 mK and exhibit an NEP of $1 \times 10^{-16}$ W/$\sqrt{\text{Hz}}$, while the coupling at 148 GHz occurs through double-slot dipole antennas. By the end of its lifetime, POLARBEAR was capable of performing a large angle survey of the Southern Sky with low enough noise that the lensing signal could be reconstructed with more precision from polarization than from CMB temperature. By design, POLARBEAR was supposed to be capable of detecting B-mode polarization down to a tensor-to-scalar ratio of 0.025. An updated POLARBEAR has been deployed in 2022 under the name POLARBEAR 2b (PB-2b) and is currently a part of the Simons Observatory Array [171]. PB-2b's focal plane consists of 7588 lenslet-antenna coupled polarization-sensitive Al/Mn TES bolometers which are simultaneously sensitive to 95 GHz and 150 GHz bands. The 7588 TESs are read out with 40 lines in an FDM scheme with a multiplexing factor of about 40:1 [172].

#### 4.4.8. QUBIC

The Q and U Bolometric Interferometer for Cosmology (QUBIC) [173] employs an interferometric approach to detecting the polarization of CMB radiation within two main bands: at 150 and 220 GHz [174]. The deployment site for QUBIC is in Alto Chorrillos, Argentina [175]. Bolometric interferometry allows for the production of maps of the CMB polarization with a resolution of 23 arcminutes. The detector module consists of 256 NbSi TESs with a critical temperature of ∼410 mK multiplexed 128:1 in a TDM scheme [176]. The TESs exhibit an NEP below $2 \times 10^{-16}$ W$/\sqrt{\text{Hz}}$ [174].

#### 4.4.9. AliCPT

The Ali CMB Polarization Telescope (AliCPT) is the first Chinese CMB telescope in the Tibetan plateau to perform unprecedented CMB polarization measurements in the northern hemisphere. Its primary scientific goal is the detection of primordial gravitational waves with sensitivity $\sigma(r) \sim 0.02$ and an *a posteriori* maximum of $r$ in the range 0.012–0.029 [177]. AliCPT is a 72 cm aperture two-lens refracting telescope and will feature 32,376 TES polarimeters aimed at the detection of the 90 and 150 GHz bands [178]. The AliCPT focal plane consists of 19 independent module polarization-sensitive feedhorn-coupled Al/Mn TESs ($T_C \sim 420$ mK) equally split between the 90 and the 150 GHz bands. The TESs are read out in a µ-MUX scheme with a multiplexing factor of 2000:1. The 90 GHz band is expected to exhibit a saturation power of 7 pW and an NEP of $3.8 \times 10^{-17}$ W $/\sqrt{\text{Hz}}$, whereas the expected saturation power for the 150 GHz band is 12 pW with an NEP of $5.3 \times 10^{-17}$ W$/\sqrt{\text{Hz}}$ [179].

#### 4.4.10. Simons Observatory

The Simons Observatory, also located in the Atacama desert of Chile, is a ground-based CMB observatory funded by the Marilyn and Jim Simons foundation as well as the Heising–Simons foundation [180]. The Simons Observatory aims to observe the CMB polarization at six frequency bands centered around 30, 40, 90, 150, 230 and 280 GHz. It will consist of one Large Aperture Telescope (6 m primary mirror and 7.8° field of view) and three Small Aperture Telescopes (0.42 m aperture) [181]. While the former is sensitive to all bands mentioned before, two of the Small Aperture Telescopes observe in the 90 and 150 GHz bands while the remaining one observes at 220 and 270 GHz. The TESs (Al/Mn) exhibit a critical temperature of ∼190 mK and an NEP $\sim 4.1 \times 10^{-17}$ W$/\sqrt{\text{Hz}}$ [182,183]. The primary scientific goal of the Simons Observatory is producing a polarization maps of the sky with a ten-fold improved sensitivity compared to Planck [181]. As secondary goals, the Simons Observatory aims to measure the sum of neutrino masses, and investigate the galaxy evolution and the duration of the reionization epoch [184].

#### 4.4.11. CMB-S4

The cosmic microwave background Stage 4 (CMB-S4) is a future ground-based CMB experiment with 19 telescopes between the Atacama desert in Chile and Antarctica aiming to investigate the existence of primordial B-mode polarized light to a tensor-to-scalar ratio as low as $10^{-3}$ [185,186]. In its preliminary form, CMB-S4 aims to employ fourteen 0.55 m Small Area Telescopes (SATs) at 155 GHz and below and four 0.44 m SATs at 230/280 GHz, with dichroic, horn-coupled Al/Mn [187] TESs in each SAT, measuring two of the eight targeted frequency bands between 25 and 280 GHz. Furthermore, it aims to employ one 5 m class Large Area Telescope (LAT), for 'delensing' purposes, equipped with TESs distributed over seven bands from 20 to 280 GHz [188].

#### 4.4.12. EBEX

The E and B Experiment (EBEX) was a balloon-borne experiment for the detection of CMB anisotropies during a 27-day circumpolar flight in Antarctica [189]. The great advantage of a balloon-borne experiment over the aforementioned ground-based experiments is the fact that its flight altitude is ∼42 km, at which the absorption of microwave radiation is

almost negligible. This allows for higher SNR compared to ground-based experiments of the same size. EBEX features 1432 TES bolometric detectors read out in an FDM scheme. EBEX observes in three frequency bands, namely 150 GHz, 250 GHz and 410 GHz, with 768, 384 and 280 TESs, respectively [190]. Each TES is made of an Al/Ti bilayer with a critical temperature of 500 mK and as an array, the NEP is below $1.7 \times 10^{-17}$ W/$\sqrt{\text{Hz}}$ [189]. It contributed to setting a constraint on the value of the tensor-to-scalar to $r \leq 0.034$ ratio along with the measurements performed with Planck and the BICEP/Keck Array.

#### 4.4.13. SPIDER

SPIDER is a balloon-borne CMB experiment [191,192] deployed in a 17-day circumpolar flight from Antarctica in 2015 [193]. The payload consists of six monochromatic refracting telescopes mounted within the same cryostat for observations at 100, 150 and 280 GHz. Each telescope was equipped with a polarization-sensitive TES array for a total of 800 pixels read out in a TDM scheme. The TESs for such observations are made of pure Ti with a critical temperature of 500 mK and exhibit an overall NEP $\sim 4 \times 10^{-17}$ W/$\sqrt{\text{Hz}}$ [194]. With just a 10% sky coverage, SPIDER derived the upper limit on the tensor-to-scalar ratio as $r \leq 0.11$ with a confidence level of 95% [195].

#### 4.4.14. LSPE

The Large-Scale Polarization Explorer (LSPE) is a proposed balloon-borne experiment for the measurement of CMB anisotropies at large angular scales [196]. The project, expected to fly in 2026, is funded by INFN and ASI and the circumpolar flight is in partnership with NASA. LSPE consists of two instruments: SWIPE (Short Wavelength Instrument for the Polarization Explorer) and STRIP (Survey Tenerife Polarimeter). LSPE/SWIPE [197] is a Stokes polarimeter with a cold half-wave plate modulator and its two focal planes are equipped with 330 multi-mode Spiderweb TES bolometers [198] at 140, 220 and 240 GHz. LSPE/STRIP [199] is aimed at accurate measurements of the low-frequency polarized radiation at 44 and 90 GHz, dominated by Galactic synchrotron emission and deploys a detection system based on OMTs and HEMT amplifiers.

The LSPE/SWIPE TES are made of a Ti/Au with a critical temperature of 500 mK and a saturation power of 10 pW. The TESs are intended to exhibit an NEP below $1 \times 10^{-17}$ W/$\sqrt{\text{Hz}}$ so that the experiment is limited by the photon noise of the sources.

#### 4.4.15. LiteBIRD

LiteBIRD, the acronym for 'The Lite (Light) satellite for the study of B-mode polarization and Inflation from cosmic background Radiation Detection' is a JAXA-led spacecraft mission which aims to measure the B-mode polarization of the CMB with sensitivity such that a tensor-to-scalar ratio as small as $r \sim 0.001$ can be measured (LiteBIRD will be able to measure $r = 0$ with $\delta r \leq 0.001$) [200]. LiteBIRD will produce a fine CMB at large angular scales at 60, 78, 100, 140, 195 and 280 GHz, where the first two and last two bands are required to perform foreground subtraction and the 100 and 140 GHz bands are the CMB channels.

As of July 2024, the full engineering details of LiteBIRD are not defined yet, but it will most likely be constituted of two main instruments: the Low Frequency Telescope (LFT) [201], and the Medium and High Frequency Telescope (MHFT) [202]. While the LFT is sensitive between 30 and 160 GHz in nine overlapping bands, the MHFT spans between 80 and 500 GHz in nine more overlapping bands. LiteBIRD will be equipped with over 4000 multichroic TESs read out in an FDM scheme with a multiplexing factor $\sim 68$. The TES bolometers, produced by NIST, are made of Al/Mn with a critical temperature of 200 mK, an NEP of $\sim 1 \times 10^{-17}$ W/$\sqrt{\text{Hz}}$ and a saturation power in the order of 1.9–4.8 pW [203].

## 5. Applications in Nuclear, Particle and Astroparticle Physics

The search of DM is moving towards joint ventures between astrophysical observations and laboratory experiments. Given the multitude of DM models currently available,

different experiments are being proposed and carried out to extend the search of DM particles to masses below 10 GeV. These experiments rely on measuring very small fractions of energy deposited in the detector through DM-nucleus scattering [204–208]. Similarly, extremely sensitive detectors capable of measuring very small energies can enable new experiments that further progress our understanding of neutrino physics. These experiments include the search for neutrino-less double-beta ($0\nu2\beta$) decay [209,210] and other processes beyond the standard model, the detection and measurement of Coherent Elastic Neutrino-Nucleus Scattering (CE$\nu$NS) [211] and probe the absolute scale of the neutrino mass (e.g., goals of HOLMES and CUPID) enabling the possibility to determine the neutrino mass hierarchy.

Furthermore, neutrinos represent an unavoidable background for DM search [212] and sterile neutrinos are competitive DM candidates [213].

TESs could be the cornerstone for experimental studies both for neutrino physics and DM search, thanks to their excellent sensitivity. In this section, we will present current experiments exploiting TESs for neutrino studies and DM searches.

### *5.1. Electron Capture Decay*

#### 5.1.1. HOLMES

HOLMES is an experiment which aims to determine the absolute value of electron neutrino mass with a sensitivity of $\sim$1 eV by measuring the de-excitation energy spectrum of $^{163}$Ho electron capture (EC) decay [214]. This approach requires a calorimetric measurement, which allows one to reconstruct all the EC de-excitation energy, and a high energy resolution, especially for energies close to the kinematic endpoint of the decay ($Q_{EC} \sim 3$ keV). In order to meet these requirements, HOLMES will use an array composed of a large number of TES microcalorimeters.

Each single pixel of the HOLMES experiment consists of a ($125 \times 125$ μm$^2$) Mo-Cu bilayer TES sensor in thermal contact with a ($200 \times 200 \times 2$ μm$^3$) Au absorber which is directly implanted with $^{163}$Ho. Both the sensor and the absorber are suspended on a $Si_3N_4$ membrane. This device exhibits an energy resolution of 4.22 eV at 6 keV [215].

HOLMES TESs are read out by a microwave SQUID multiplexing chip, developed and fabricated by NIST, which allows for the parallel read out of 33 channels.

#### 5.1.2. NuMECS

The neutrino ($\nu$) Mass Electron-Capture Spectroscopy [216] collaboration aims at measuring the neutrino mass through calorimetric spectroscopy of EC events in decay isotopes such as $^{163}$Ho which are embedded in Mo/Au TES, similar to those fabricated for HOLMES [4].

### *5.2. Rare β and Double-β Decays*

#### 5.2.1. CUPID

CUPID (CUORE Upgrade with Particle Identification) is the next generation experiment which aims to measure the lepton flavour-violating process ($0\nu2\beta$) decay [217,218]. It will be host in the same cryogenic infrastructure of its predecessor, and state-of-art $0\nu2\beta$ decay experiment, CUORE [209] at the Gran Sasso National Laboratory (Italy). When deployed, it will utilise an array of approximately 1600 scintillating $Li_2{}^{100}MoO_4$ crystals, each enriched with the $^{100}$Mo isotope and having a mass of 280 g [218]. CUPID, compared to CUORE, will benefit from an improved background suppression achieved via a double read out of the thermal and optical signals produced by its crystals.

While the detectors of choice for CUPID are NTD Ge, TESs are considered as a promising technology for upgrades towards CUPID-1T. Singh et al. [219] present a large-area TES photon detector which meets the requirement to be employed in the CUPID experiment for the light channel read out. In this device, a TES is coupled to a large area (50.8 mm diameter) Si wafer which acts as a photon absorber. The sensor is a bilayer (45 nm Ir and 20 nm Pt) superconducting film; it has an area of 330 μm $\times$ 300 μm and exhibits a

critical temperature of ∼33 mK. Further R&D efforts towards further upgrades of CUPID such as CUPID-1T involved the instrumentation of a $Li_2{}^{100}MoO_4$ crystal with an Al/Mn TES, such as described by Bratrud et al. [220].

#### 5.2.2. ACCESS Project

The ACCESS (Array of Cryogenic Calorimeters to Evaluate Spectral Shapes) intends to perform precision measurements of forbidden $\beta$-decays. A testbed with a pilot array of calorimeters based on natural and doped crystal containing $\beta$-emitters ($^{113}$Cd and $^{115}$Id, and $^{99}$Tc) will be performed. While the obvious choice of detectors for ACCESS is germanium NTDs such as those for CUORE and CUPID, the possibility of employing TESs is currently being investigated [221].

### *5.3. Coherent Elastic Neutrino-Nucleus Scattering*

#### 5.3.1. NUCLEUS

NUCLEUS is a cryogenic experiment that will explore CE$\nu$NS by measuring nuclear recoil energies down to 10 eV [222]. It will be installed at an experimental site at the Chooz nuclear power plant (France) where it will benefit from a large flux of $O(\mathrm{MeV})$ energy (anti)neutrinos [223].

NUCLEUS, as a nuclear recoil detector, will employ an array of cryogenic calorimeters composed of nine $CaWO_4$ and nine $Al_2O_3$ crystals with a total mass of 10 g [222]. In each calorimeter, a TES, similar to those developed for the CRESST experiment (see Section 5.4.1), is used as the sensor. This TES consists of a 200 nm tungsten film coupled to an Al phonon collector and is operated at a temperature of 15 mK. A prototype 0.5 g $Al_2O_3$ calorimeter achieved an energy threshold below 20 eV.

In order to attain background reduction, the NUCLEUS detector will be encapsulated in a cryogenic veto [224]. This will include an instrumented Si detector holder and a surrounding kg-scale detector. Tungsten TESs are employed in both veto detectors as phonon sensors.

#### 5.3.2. MInER

The Mitchell Institute Neutrino Experiment at Reactor (MInER) is a CE$\nu$NS experiment with a 1 MW reactor as the source of electron anti-neutrinos with an energy up to a few MeV [225]. The detector consists of a sapphire $Al_2O_3$ absorber connected to SuperCDMS-like TES modules [226]. Further details on the detectors can be found in Section 5.4.2.

#### 5.3.3. CRAB

The CRAB (Calibrated nuclear Recoils for Accurate Bolometry) Collaboration suggests the use of nuclear recoil induced by radiative capture of thermal neutrons as an efficient way to calibrate detectors in the 100 eV range [227]. The NUCLEUS and CRAB Collaborations reported on the observation of such a detected peak in a 0.75 g protoypal $CaWO_4$ detector at 112 eV irradiated by a neutron source arising from $^{252}$Cf. The detector was built for the first phase of NUCLEUS and is based on TES developed for CRESST (see Section 5.4.1) and described in [204].

#### 5.3.4. RES-NOVA

RES-NOVA is a proposed observatory which intends to detect cosmic neutrinos originating from core-collapsing supernovae through nuclear scattering (CE$\nu$NS) in array detectors primarily made of Roman lead (Pb) exploiting the high CE$\nu$NS cross-section and the unmatched isotopic purity of archelogical Pb [228]. The detector is made up of 500 large-mass Pb single crystals paired with ultra-sensitive TESs to measure any possible temperature increases due to particle interaction [229]. RES-NOVA aims at targeting energy thresholds of 1 keV or below in order to be sensitive to flavour-blind neutrinos with an exposure of 620 ton · y [228].

#### 5.3.5. Ricochet

The Ricochet experiment will performs an accurate measurement of CE$\nu$NS spectrum at the Institute Laue-Langevin nuclear reactor (France) [230]. For this purpose, it will employ an array of cryogenic calorimeters based on two different technologies: NTD-Ge thermistors [231] and TESs [232]. The TES-based detector will include the following: (1) an absorber that could be made of different material such as Si, Ge, Zn or Al; (2) a TES film deposited on a Si substrate separated from the latter; and (3) a readout and bias circuit.

A prototype of the Ricochet TES-based detector, which employs an Al/Mn superconductive film and a 1 g Si absorber, is presented in [233]. This device exhibits a baseline root-mean-square energy resolution lower than 40 eV.

### *5.4. Dark Matter and Axions*

#### 5.4.1. CRESST

CRESST (Cryogenic Rare Event Search using Superconducting Thermometers) is an experiment hosted at the Grans Sasso National Laboratory which searches for weakly interacting massive particles (WIMPs) of energy $< 400$ keV [234] by taking advantage of their elastic scattering with $CaWO_4$ crystals [235]. This interaction produces both phononic overheating of the crystal and scintillation light. The latter strongly depends on the type of the interacting particle. CRESST exploits TESs both as phonon and photon detectors to evaluate the type and energy of the incident particle. The thermistor of these TESs is made of tungsten and operate at a temperature of about 15 mK. These detectors showed an energy resolution of 4.1 eV (6.7 eV) at an energy of 5.9 keV (6.5 keV) [236].

#### 5.4.2. SuperCDMS

The Cryogenic Dark Matter Search (SuperCDMS) collaboration intends to detect DM particles at the Sudbury Neutrino Observatory facility (SNOLAB) in Canada. The detection principle relies on measuring the ionization and the phonons produced by the scattering of Weakly Interacting Massive Particles (WIMPs), a DM candidate, with the nucleus of ultra-pure Ge and Si crystals. The thermal energy thus deposited is read out with tungsten TESs. The expected phonon energy resolution is better than 5 eV and recoil energy resolution is better than 1 eV [237].

#### 5.4.3. ALPS II

Any Light Particle Search (ALPS) II is a light shining through a wall (LSW) experiment searching for axion-like particles (ALPs) which are possible candidates as weakly interactive sub-eV particles (WISPs) [238]. In an LSW experiment, a laser beam is sent through a long magnet, allowing for the coherent photon–axion conversion due to the Primakoff effect [239]. The wall acts as a barrier for the light, while the almost zero cross-section for the axion/baryonic matter interaction enables the axion to pass through the wall. The photon–axion back conversion is produced by a second magnet after the wall. Since the conversion process is very rare, ALPS II exploits optical resonators to boost both the number of photons for ALP production and their reconversion probability to light. ALPS II aims at demonstrating the existence of particles of mass 1 μeV$< m <$ 1 meV. To this end, tungsten TESs operating at ∼20 mK have been developed. At the moment, TESs with energy resolution of about 150 meV have been demonstrated at 1.165 eV [240].

#### 5.4.4. EDELWEISS

Similarly to SuperCDMS, EDELWEISS (Expérience pour Detecter Les WIMPs En Site Souterrain) targets the detection of WIMPs through the ionization and the phononic signals produced in ultra-pure Ge crystals. While EDELWEISS relies on Ge crystals instrumented with NTD detectors [241], in order to investigate light-WIMPs, the EDELWEISS collaboration is pursuing an R&D activity to achieve 1 eV threshold Ge bolometers coupled to efficient background-rejection techniques. In this scope, $Nb_x/Si_{1-x}$ TESs are currently being developed [242]. Further R&D efforts are being put in place by the CRYOSEL collaboration

which effectively demonstrated the operation of an NTD and a superconducting single-electron device, which operates in a similar way to the devices described in Section 9.2. For further details, see [243].

#### 5.4.5. STAX

STAX is an LSW experiment proposing to search for ALPs at extremely low energies $m < 10$ μeV [244] by exploiting gyrotrons, which are very intense sub-THz photon sources [245]. In particular, STAX proposed the use of gyrotrons operating at 30 GHz with a power of several tense MW. The main challenges of the project were as follows: (i) the realization of a high quality factor GHz cavity operating under high inject power, (ii) the realization of a high quality factor GHz cavity operating at cryogenic temperatures under strong magnetic fields (10 T), and (iii) the development of TES calorimeters for extremely low energies. In particular, STAX proposed the use of a molybdenum TES with an operating temperature of about 15 mK. Furthermore, the miniaturization of the thermistor/absorber was proposed [35].

#### 5.4.6. COSINUS

The COSINUS experiment (Cryogenic Observatory for Signals seen in Next-generation Underground Searches) is intended to perform follow up measurements on the DAMA/LIBRA [246] results. DAMA/LIBRA detected an annual modulation of DM signal due to the Earth orbiting around the sun and thus modulating its relative velocity with respect to the DM particles [247]. The novelty introduced by COSINUS consists in coupling the NaI targets of DAMA/LIBRA with a dual channel (light and phonon) readout in a similar fashion to CRESST [248]. The phonon channel consists of an Au pad on the NaI absorber which is wire bonded to a tungsten TES with a critical temperature of 28 mK and an energy resolution of 0.441 keV, while the light channel, which also employs the same tungsten TES, exhibits an energy resolution of 0.988 keV up to 200 keV [249].

#### 5.4.7. BabyIAXO

BabyIAXO is an intermediate stage of the International Axion Observatory (IAXO) and its primary goal is the testing of the different subsystems of the IAXO, BabyIAXO will also detect or reject solar axions with axion–photon coupling down to $g_{a\gamma} \sim 1.5 \times 10^{-11}$ GeV$^{-1}$ [250]. As of the present date, several detector technologies are being investigated including TESs as possible for implementation [250].

#### 5.4.8. TESSERACT

TESSERACT represents the synergistic effort of searching DM through the exploitation of cryogenic targets and sub-eV TESs by two distinct experiments HeRALD (Helium Roton Apparatus for Light Dark matter) and SPICE (Sub-eV Polar Interaction Cryogenic Experiment) complemented with EDELWEISS and Ricochet [251]. HeRALD exploits the interaction of DM with a superfluid helium target, which produced scintillation light and evaporated atoms (an energy of 1 meV is necessary to evaporate an atom) [252]. Instead, SPICE uses sapphire or GaAs crystals that generate athermal phonons after interacting with DM [253].

TESSERACT exploits the same TESs with aluminum absorbers to detect light, atom evaporation and phonons. This approach ensures a different DM mass search window from meV-to-GeV allowing one to probe DM candidates over 12 orders of magnitude, thus testing different DM models [251].

## 6. Biophysics and Medical Imaging with Transition Edge Sensors

The technological advancement of Transition Edge Sensors as semi-commercial energy-resolving single-photon detectors has allowed several groups around the world to investigate the possibility of using such detectors for biomedical imaging.

The fundamental idea behind these applications is using a TES as the main detector of a Confocal Laser Scanning Microscope (CLSM). Differently from a conventional microscope, where the sample is evenly illuminated with a wide light source producing a focused image and an unfocused background, a confocal microscope uses point-illumination and a pinhole aperture in order to effectively eliminate the out-of-focus light. By raster-scanning the whole surface of the specimen under investigation, it is possible to achieve an effective focus-stack of the specimen as well as information on the thickness of the specimen. In cases where a laser source is used to induce fluorescence in the specimen, a confocal microscope has the extra advantage of only exciting a single point of the specimen. Since only the fluorescence light that is produced very close to the focal plane can be detected, this results in a higher optical resolution image.

In this scenario, the single-photon sensitivity of TESs comes as a great advantage when working with living cells, where light irradiation deteriorates the cells and causes the photo-bleaching of any fluorescent dyes used as markers [254]. Moreover, the incredible resolution of TESs allows for the identification of different biomarkers in the same specimen, hence the identification of different functions and features within the specimen. The energy resolution in standard confocal microscopes is achieved through the use of a diffraction grating or optical filters which further increase the radiation dose to which the specimen is exposed.

Niwa et al. [255] (2017) proposed the first confocal microscope with a TES detector which also exploits the optical fiber that is used to feed the light into the cryostat as the pinhole of the microscope, further reducing the complexity of the instrument. Such an instrument exhibited an astounding 98% photon-detection efficiency at 850 nm [256] while being successfully able to capture photons in the 400–2800 nm range spanning the whole visible and near infra-red.

Such an instrument was used to collect a sample image of yellow, red and blue ink spots. Under the same illumination, in the few ($\sim$20) photons regime, a raster scan was performed and the light was detected by both a photo-multiplier tube (PMT) and a TES. Associating a colored pixel in the image according to the response of the TES (blue for wavelengths shorter than 500 nm, green between 500 and 600 nm and red from 600 to 800 nm) Niwa et al. [255] thus demonstrated the capability of the TES to distinguish the different ink pigments, impossible for the PMT which only produced a grey-scale image. They also demonstrated that a CMOS sensor needed one hundred-fold the illumination and a ten-fold exposure time to produce similar images. Furthermore, neither the CMOS sensors nor the PMTs exhibited any sensitivity to the near infra-red radiation to which the TES was sensitive.

Building on these results, Niwa et al. [257] demonstrated the use of a TES-based CLSM as a bio-imager for a fixed fluorescence-labelled cell, where three different dyes were simultaneously excited with the use of a 405 and a 488 nm laser. Using a single raster-scan, an RGB color image and a near-infrared image were produced with the means of only a few tens of photons per pixel and an irradiation power of 100 nW. The total exposure time was of 35 min at 20 ms per pixel and a raster step-size of 25 µm. In order to speed up the scan, two further improvements can be made: a faster X-Y micro-manipulator for the scan and the development of a multi-fiber–multi-TES array which contributes to the reduction of the scanning steps necessary. Further work in this direction by [258] consisted in the development of sub-µs TESs. Such fast detectors can be combined into arrays with extremely short dead times, and hence may result in reduced scan times.

In the same research group, Fukuda [259] investigated the energy resolution of single pixel TESs and the possibility of employing them in a raster-scan microscope where the sample/specimen is wide-field illuminated with a low-intensity light source. Such an apparatus demonstrated the capability of discerning different materials such as copper, silk and resistance by their color. Furthermore, since each pixel contains the spectrum between 400 and 1800 nm, it is possible to infer the different materials by their optical properties.

As a final remark, the work of Hao et al. [260] is worth of a mention. In said paper, they suggested the development of an Inductive Superconducting Transition Edge Detector (ISTED) which employs a thin patch of a superconductor deposited within a SQUID loop and maintained below transition temperature. Any energy deposition produces an increase in the temperature of the film and thus a change in the loop inductance by means of a change in the London penetration depth of the film. ISTEDs are expected to be capable of detecting massive molecular or polymeric species. Such bolometers would allow for the detection of large (>200 Da) fragments of DNA or bio-markers such as immunoglobulin with an unprecedented energy and spectrographs of 'difficult' molecular species [259].

## 7. TES for Quantum Applications

Quantum optics and quantum computing are on the rise as bleeding edge topics. In the dynamic landscape of quantum applications, TESs can play a critical role thanks to their single photon sensitivity and high quantum efficiency at communication wavelengths. Their unmatched sensitivity and their rather limited dark count rate make TESs promising detectors for a veto that rejects calculations which are potentially disturbed by the environment.

### *7.1. Quantum Optics and Quantum communication*

Transition Edge Sensors with their near-unity quantum efficiency and their single-photon sensitivity are currently being investigated as possible photon-counting detectors for quantum information systems and quantum optics experiments. As of currently, the detection and counting of telecom wavelength (1550 nm) photons with near-unity efficiency can only be achieved with low-temperature superconducting detectors such as Microwave Kinetic Inductance Detectors (MKIDs), Superconducting Nanowire Single Photon Detectors (SNSPDs) and Transition Edge Sensors.

The first experiment to benefit from the photon-detection capabilities of TESs was a Hong-Ou-Mandel (HOM) interference [261] experiment in which TESs were deployed to perform measurement of the output photon-number statistics. HOM interference is an effect that arises from the bosonic nature of photons and forbids two indistinguishable non-entangled photons that enter two different inputs of a beam splitter to exit at different outputs. Di Giuseppe et al. [262] successfully measured the photon-number statistics at the output of an HOM inteferometer when illuminated with a pair of orthogonally polarized photons arising from a Beta Barium Borate (BBO) photonic crystal. As the difference between the two photon paths approaches zero, the probability of measuring one photon at either output of the interferometer drops to zero. Di Giuseppe et al. [262] varied the optical path to create a delay between the two photons and demonstrated that, when then optical paths are identical, no single photon statistic can be measured at either end of the interferometer.

The production and verification of non-classical light states is one of the most critical limitations to the further development of quantum optics, quantum metrology and quantum computing [263–265]. Photon-number-resolving tungsten TESs allow direct access to the photon statistics of the light field in quantum metrology of light sources [266]. Another application of TESs for quantum optics experiments is in the generation of Coherent State Superpositions (CSSs) also known as Schroedinger Cat States. Such states exist when each subsystem of the superposition contains a macroscopic number of photons [267]. At least two experiments aimed at generating CSSs through photon subtraction have been performed using tungsten TESs to detect and indicate the presence of the CSS. The detection of such a CSS occurs through an optical homodyne readout scheme [268–270]. The TES used in such experiments exhibited an efficiency of 85% at 860 nm and photon-counting capabilities of up to a few tens of photons [269,271].

One further example of CSS produced by photon subtraction was demonstrated by Zhai et al. [272]. They demonstrated the subtraction of up to eight photons from a thermal state. By the use of a tungsten Transition Edge Sensor, it was possible to reconstruct the

photon number statistics as a function of the subtracted photons, demonstrating that the photon number of the photon-subtracted states increased linearly with the number of photons subtracted from the thermal state. Zhai et al. [272] further demonstrated that a TES-based setup allows for the derivation of correlation functions of second and further order can be derived from the photon number statistics [268,272].

TESs have been used as photon detectors in experiments intended to demonstrate the violation of the CH Bell inequality [273], which is a modified version of the more famous Bell inequality. Christensen et al. [274] deployed TES optimized for a wavelength of 710 nm with a 95% detection efficiency, achieving an overall 75% system efficiency. Giustina et al. [275] demonstrated the violation of the CH Bell inequality with a 78% system efficiency when using a TES optimized for the detection of 810 nm and a photon-detection efficiency of 95%.

Schmidt et al. [266] developed a system for photon number-resolving experiment with the use of two fiber-coupled TESs optimized for the detection of photons at 1087 nm with a detection efficiency larger than 87% and such a system has been deployed in experiments on single and twin-photon states [276] and the investigation of the emission statistics of bimodal lasers [277] and polarization lasers [278].

Chunnilall et al. [265] suggest the use of TESs for Quantum Key Distribution (QKD). QKD uses photons to generate a cyphered secret key between either end of a communication. QKD is a 'secure' communication channel because if the photons that serve as the communication medium are intercepted, their state is changed and the users at either end of the communication will know that the communication channel was 'hacked'. The paper suggests using a TES-based radiometer for the detection of such QKD photons (1550 nm) with optical powers in the range 50 fW–20 nW with repeatability better than $\pm 0.3\%$ and an NEP of $5 \times 10^{-15}$ W$/\sqrt{\text{Hz}}$.

### *7.2. Quantum Computing*

A concept device has been presented that combines a TES with a superconducting qubit on a shared silicon substrate. The idea is that the phonons produced by any radiation can spread efficiently through the substrate and thus both the qubits and the TES will experience correlated disturbances induced by the radiation. This correlated disturbance has been directly measured with substrates on which multiple quibits [279,280] and MKIDs [281] are present. The idea of pairing a qubit with a TES relies on the assumption that one single sensor is capable of detecting the condition of a radiation-induced error for all qubits on the same silicon substrate [282] and exploits the signal from the TES as a veto to reject the calculations that could be potentially incorrect due to an environmental disturbance. Orrell and Loer [282] demonstrated that radiation-induced disturbances can be monitored with a TES and they appear as a current peak with an amplitude of $\sim$100 nA, a rising edge of 5 µs and a 100 µs decay time. In reality, Orrell and Loer [282] also affirm that the choice of superconducting detector (in this case a TES) is potentially interchangable between TESs, MKIDs and SNSPDs.

## 8. TES as Detectors for X-Ray Spectroscopy and Imaging

### *8.1. X-Ray Spectroscopy at Beam-Line Facilities*

Transition Edge Sensors can be optimized to be excellent Soft X-ray detectors for many applications at beam-line facilities and in STEM equipment [283]. Near unity quantum efficiency, an energy resolution in the order of a few eV at 1–10 keV and their wide bandwidth makes them the obvious choice for many applications such as X-ray Emission and Absorption Spectroscopy (XES and XAS) and Resonant Inelastic X-ray Scattering (RIXS) [284]. TES detectors have been deployed at X-ray light sources since 2012 (U7A at Sinchrotron National Light Source—SNLS) [285]. The detector array consists of 240 Mo/Cu ($T_c = 107$ mK) TESs coupled each to a Bi absorber and read out in a $8 \times 30$ TDM scheme with a switching interval of 160 ns.

The deployment of TESs as beam-line X-ray detectors has been shown by Doriese et al. [286] who report NIST spectrometers deployed at light sources such as NIST, SNLS, Paul Scherrer Institut (PSI), Jyväskylä Pelletron and Lund Kemicentrum.

At NIST, the demonstration scale spectrometer acquired the spectrum of ammonium ferrioxalate in water [287] as well as $Fe_2O_3$ and $FeS_3$, which are high-spin and low-spin compounds. XES allowed one to distinguish the different features of the different ferrous compounds through the intensity ratios of $K_{\alpha_1}$ and $K_{\alpha_2}$ lines as well as $K_{\beta'}$ features in the $Fe_2O_3$ specimen.

The NIST system, like the one deployed in Lund, was proven to be capable of performing pump-probe XES to measure the spin state of different Fe vs time in photo-induced reactions [288].

At SNLS, the spectrometers were deployed to measure the elemental compositions of different samples, in particular the first tests included the spectrum of a 0.7% C sample in $SiO_2$, but most importantly it was successful at distinguishing ammonium nitrite ($NH_4NO_3$) from the explosive RDX ($C_3H_6N_6O_6$) based solely on the nitrogen content and in faster time than with more standard spectrometers [289].

The application at PSI involved the spectroscopy of exotic atoms and is fully described in Section 8.2; at Jyväskylä Pelletron, the spectrometer was tested for Particle-Induced X-ray Emission (PIXE) spectroscopy. An ion beam excites the samples in order to study its elemental composition through X-ray spectroscopy. TESs are excellent detectors for PIXE spectroscopy because of their high energy resolution that allows the resolution of almost all spectral-line overlaps of different atoms and because they exhibit better collection efficiency than Silicon Drift Detectors (SDDs) [286]. Palosaari et al. [290] demonstrated the capability of a TES-based PIXE spectrometer to distinguish eV-scale shifts in the Ti $K_\alpha$ line and $K_\beta$ structures in samples known to exhibit Ti atoms in different oxidation states.

One further application of a 240 pixel TES array produced by NIST is in an instrument at the SPring-8 (Super Photon Ring-8 GeV) synchrotron. Such a TES array was used to conduct X-ray Absorption Near-Edge Structure (XANES) analysis in fluorescence. TESs resulted in excellent detectors of fluorescence lines from diluted samples thanks to their energy resolution being better than 5 eV at 6 keV. As a test example, the NIST TES array could detect the presence of rare earths in a natural sample: europium (Eu), for instance, could be detected as soon as its mass fraction exceeded 0.1% of Mn [291]. Finally, Yamada et al. [291] demonstrated the capability of the instrument to distinguish between the spectrum of a blank target from the same target in a rare Fe aerosol. In 2019, the NIST EBIT TES Spectrometer (NETS) was commissioned, it improves on the capabilities of the spectrometer for the Electron Beam Ion Trap (EBIT). It consists of a 192 TES array optimized for sensitivity in the 0.5–8 keV range with energy resolution ranging between 3.7 and 5 eV. The calibration of the instrument resulted in line accuracy to below 100 meV in narrow band spectra.

Further development is in progress to develop a 1000 pixel spectrometer with 0.5 eV energy resolution for energies below 1 keV to be deployed at the Linac Coherent Light Source (LCLS-II) at SLAC National Laboratory [292].

### *8.2. X-Ray Spectroscopy for Exotic Atoms*

Exotic atoms are atoms which are normal except for the replacement of one or more of the sub-atomic particles with different particles with the same electric charge. For instance, Hadronic atoms are atoms which have one or more electrons replaced by hadrons such as $\pi$ (pionic atoms) or $K$ (kaonic atoms); hadrons such as $K$ can interact with the atomic nucleus not only through electromagnetic force, but also with attractive short-range strong force. This is most relevant for hadrons in the most inner and tightly bound orbitals. When looking at the innermost orbitals of a hadronic atom, the strong-force interaction produces a shift in their energy levels and a widening of their spectral lines due to the absorption of the hadron by the nucleus [293]. This interaction is not well established quantitatively due to a lack of precise data and because the current data can be explained through both a phenomenological interaction potential ($\sim -180$ MeV) and a chirally motivated potential

($\sim -50$ MeV). The shift and the broadening can be measured from the characteristic X-ray emission. Understanding such nuclear states would not only provide the community with better understanding of hadron properties, but also enlarge the concept of matter and provide further ground for exotic-atoms based astrophysics and cosmological models.

Traditionally, exotic atom X-ray spectroscopy was performed with SDDs but their energy resolution of about 200 eV at 6 keV was a major limitation to the experiments. The HEATES collaboration [294,295] demonstrated that Transition Edge Sensors can be multiplexed in a 240-pixel TDM array and optimized to exhibit an energy resolution of $\sim$5.7 eV at 6.9 keV, allowing the identification of spectral features with systematic uncertainties in the order of 0.1 eV as shown by [295]. With such an instrument, in 2014 the HEATES collaboration collaboration et al. [295] observed the $\pi - ^{12}C\ 4f \rightarrow 3d$ transition and for the first time the $\pi - ^{12}C\ 4d \rightarrow 3p$ which turned out to be compatible with the theoretical calculations through Seki–Masutani potential [296]. Based off such promising results, the $3d \rightarrow 2p$ transition was measured in kaonic-helium [297] such as JPARC-E62, producing measurements with sensitivities ten times better than those achieved with SDDs [298]. Further development is in progress to upgrade the test facility [299].

### *8.3. Nanoscale X-Ray Tomography of Integrated Circuits*

All proposed instruments for X-ray tomography exploit the same working principle: the X-rays are generated in a metallic conversion layer (usually Pt or Cu) on which the electron beam of a Scanning Electron Microscope (SEM) is focused in a nanometre spot, which results in an X-ray-generation volume with a diameter $\sim$130–160 nm. The X-rays thus produced are attenuated by the sample and measured by an instrument which features a TES array. NIST is leading the development efforts of such instruments. The first proposed instrument was NSENSE (Non-destructive Statistical Estimation of Nanoscale Structures and Electronics) [300] which then morphed into TOMCAT (Tomographic Circuit Analysis Tool) [301] and finally into MINT (Microscope for Integrated circuit NanoTomography). Across the years, the detectors have changed from Mo/Cu TESs with a critical temperature of 130 mK [300,302] to Mo/Au TESs with the same critical temperature [301] suspended on a SiN membrane and coupled to a bismuth X-ray absorber. The number of detectors increased from 240 for the first prototype of NSENSE [300] and MINT [302] to about 1000 pixels for the first assemblies of TOMCAT [301]. In this picture, the multiplexing technique evolved from an array of TESs read out in a TDM scheme for NSENSE [300] and MINT [302] to a μ-MUX scheme for the TOMCAT [301] prototype instrument. The energy resolution of the TESs has been measured to be 17.9 eV at the Cu $K_\alpha$ line (8.04 keV) for MINT [302], 14 eV for TOMCAT [301] and 12 eV for NSENSE [300]. Regardless, this technology has been proven effective at resolving features as small as 160 nm in a planar Cu-$SiO_2$ IC [302,303]. Further development is being carried out, especially towards the optimization of the TOMCAT instrument which is being expanded in order to accommodate 3000 pixels instead of the currently 1000 available, which will both increase the contrast of the tomography scans produced and reduce the photon-collection times.

Kikuchi et al. [304] developed an 8-Pixel TES-spectrometer for 320 keV radiation, pushing the detection range of TES-based instruments into the $\gamma$-ray range. Each pixel consists of a 0.8 mm-thick Sn absorber on a $SiO_2/Si_xN_y/SiO_2$ membrane and a Ti/Au TES with a critical temperature $T_C \sim 115$ mK. Such an instrument has been validated by carrying out $^{51}$Cr spectroscopy, yielding an impressive energy resolution of 159 eV at 320 keV.

### *8.4. Nuclear Safety*

In the scope of global nuclear nonproliferation and safeguards, the assay of plutonium-bearing materials can be carried out in a destructive and in a non-destructive fashion. The state of the art involves High-Purity germanium (HPGe) detectors which still exhibit an uncertainty limit of about 1% relative error for measured isotope ratios, which is still about one order of magnitude larger than that for destructive assays [305]. In order to be able to

measure the relative isotope abundance to 0.5%, spectra with up to tens of millions of counts are required [306], and therefore detectors capable of handling kHz count rates are necessary in order to perform such measurements in reasonable times. Transition Edge Sensors, therefore, fit perfectly the required technology. Unfortunately, the energy resolution of a TES calorimeter scales with the square root of its heat capacity [305]; therefore, in order to scale up the collection area while keeping the noise of the instrument to a minimum, it is necessary to employ a multi-pixel array: the individual heat capacity is small, whereas the total collection area increases.

Since the early 2000s, the ongoing development and optimization of Transition Edge Sensor technology has been trying to push the boundaries of $\gamma$-ray spectrometry, especially in the 20–200 keV range, which is that typical of applications such as the Non-Destructive Assay (NDA) of plutonium-enriched materials. The seminal work in this direction was lead by Zink et al. [307] and proved the feasibility of measuring a $\gamma$-ray spectrum at 103.5 keV with $\Delta E$ as low as 42 eV [307] and later 27 eV [308]. Such a calorimeter [307] was achieved through a 16-array $1 \times 1$ mm$^2$ Sn absorber each coupled to a Cu/Mo TES suspended on a SiN membrane.

In 2012, a NIST-LANL $\gamma$-spectrometer was first developed [306,309], scaling up the aforementioned instrument [310–312]. It exhibited a 256-pixel array with a collecting area of 5 cm$^2$ and it featured an energy resolution of 53 eV at 97 keV. Each detector consisted of a tin (Sn) absorber ($0.9 \times 0.9 \times 0.22$ mm$^3$) coupled to a Cu/Mo TES with critical temperature in the 100–150 mK range. The NIST-LANL instrument exhibited a 92% pixel yield and achieved optimal performance for counting rates below $2.5 \times 10^3$ counts per second and, as a proof of concept, was demonstrated to resolve the six most prominent $\gamma$-ray lines of a $^{153}$Gd radioisotope. The capability of an array of TES micro-calorimeters to measure the isotopic abundance in different Pu measurement standards was shown in [313,314]. Using the peaks at 129 keV and 203 keV, the isotopic ratios were calculated: $^{238}$ Pu/$^{239}$ Pu, $^{240}$ Pu/$^{239}$ Pu, $^{241}$ Pu/$^{239}$ Pu and $^{241}$Am/$^{239}$Pu. Such detectors were demonstrated to measure the correct value for such ratios, but when compared to HPGe detectors, TES micro-calorimeters exhibit an uncertainty which is still a factor 2 higher, thus limiting the resolution of such isotopic ratios to about 1%.

Unfortunately, a relative uncertainty of about 1% is not sufficient to achieve desired safeguard goals for large power plants. For clarity, a 1% Pu content in the fuel and a 1% measurement uncertainty leads to an uncertainty in the mass of the Pu fuel larger than the International Atomic Energy Agency (IAEA) of 8 kg for all plants with a fuel throughput larger than 80,000 kg per year.

In 2019, Becker et al. [315] finally demonstrated isotope ratios with uncertainty levels below 0.25%. This was possible using the latest NIST/LANL instrument developed in collaboration with the University of Colorado, SLEDGEHAMMER (Spectrometer to Leverage Extensive Development of Gamma-ray TESs for Huge Arrays using Microwave Multiplexed Enabled Readout), which consists of 125 TES micro-calorimeters with typical energy resolution of 75 eV at 100 keV. Such low uncertainties were achieved by acquiring high-count spectra ($10^8$ events in about 14 h) and feeding them through a pipeline. Such a pipeline at first operates to reject all data that exhibit event pile-up and also discards any events for which the baseline rms is larger than expected. Thus, the data were fed into an optimum filter pipeline [316] before being calibrated against a $^{57}$Co-$^{166m}$Ho source which features nine calibration lines in the energy range of interest (50–200 keV). The abundance ratio was evaluated at 103 keV with resolution on the area underneath the peak as low as 0.05%. Further improvement would rely on the development of a section of the pipeline that corrects for drifts in the signal produced by the calorimeters. Currently, there is ongoing work towards the increase in the number of micro-calorimeters by a factor 10 in order to speed up the assay and also the development of real-time analysis software.

Only in 2021 were the 103 keV and 159 keV $^{242}$Pu lines detected in a non-destructive measurement. The instrument used was SOFIA (Spectromenter Optimized for Facility Integrated Applications) [317,318]; it was used to characterize a sample consisting of

113.6 g of $PuO_2$ (99.75 g of Pu) in a steel 'food-pack' and placed inside a SAVVY container. Mercer et al. [319] demonstrated a very clear observation of the 103 keV peak from the $^{242}$Pu isotope with a precision on the position of the peak better than 0.5 eV. Furthermore, SOFIA is capable of resolving the $^{242}$Pu peak at 103.46 keV from the ones at 103.68 keV (arising from $^{241}$Pu) and the peak at 104.23 keV ($^{240}$Pu). Furthermore, in the region around 159 keV, SOFIA is capable of distinguishing the 159.02 keV peak ($^{241}$Pu) from the ones at 159.96 kev ($^{241}$Pu) and 160.31 keV ($^{241}$Pu $\alpha$-decay). SOFIA was capable of measuring a $^{242}$Pu/$^{240}$Pu ratio of (8.5 $\pm$ 2)% after a 12.5-h measurement with the counting statistics being the dominant factor in the uncertainty level.

## 9. Comparison with Other Superconducting Detectors

Transition Edge Sensors are the most mature technology when it comes to superconducting detectors and have been widely used for the better part of the last thirty years since Irwin [37] suggested their use in the electro-thermal feedback. TESs (both as bolometers and calorimeters) have seen applications in a plethora of fields of research and civil applications, most of which are described in this review. Transition Edge Sensors have been developed to a state of the art of unprecedented performance. Modern TESs exhibit resolving powers up to $R$ = 4000 [307] and NEP below 1 $\times 10^{-17}$ W/$\sqrt{\text{Hz}}$. Large arrays of TES have been developed and deploy several thousand pixels with multiplexing factors of up to 2000:1 [68].

In more recent years, other more-novel superconducting detectors have been invented and optimized. We intend to provide the reader with a brief overview of their characteristics and figures of merit. Our aim is to offer a helping hand in the troubled water of deciding what are the ideal superconducting detectors in many typical cases. Table 2 shows the main figures of merits of different superconducting detectors.

**Table 2. Comparison between different kinds of superconducting detectors** through some of their main figures of merit and other important information.

| | **TES** | **MKIDs** | **SNSPD** |
|---|---|---|---|
| Fabrication complexity | ○ ○ ○ | ○ | ○○ |
| Max. R (X-ray) | ≤5000 | ≤590 | N/A |
| Max. R (UVOIR) | ∼200 | 65 | ≤10 |
| NEP (typical) (W/$\sqrt{\text{Hz}}$) | $1 \times 10^{-19}$ | $3 \times 10^{-19}$ | $4.5 \times 10^{-19}$ |
| Time resolution | ∼1 µs | ∼1 µs | ∼1 ps |
| µ-MUX available? | Yes | Innate | Yes |
| Spectral range | THz/$\gamma$-ray | THz/X-ray | infra-red/Vis |
| Array size (typical) | 1 k | 20 k | 10 k |
| Pixel Yield | 95% | 75–80% | >95% |

### *9.1. Microwave Kinetic Inductance Detectors*

MKIDs are superconducting LC micro-resonators invented by Day et al. [320] in 2003 and have since been employed as photo-detectors in instrumentation ranging from astronomical telescopes to particle physics, to security applications [321]. Their working principle is rather simple: when a particle deposits its energy in the superconductor, it breaks down a number of Cooper pairs producing un-paired electrons. As the superconductor is depleted of superconducting carriers, its kinetic inductance increases (see Zmuidzinas [83]), which results in a reduced resonance frequency of the LC circuit. With a time constant that is typical of the superconductor of choice, the un-paired electrons recombine and the MKID is in its idle state ready for a new detection event. The shift in frequency is proportional to the energy deposited in the superconductor; therefore, it is possible to monitor the LC resonator in frequency and phase to identify particle-detection events and measure the energy deposited by the particle.

Advantages include sensitivity from X-rays to THz and their very straightforward fabrication as well as their inherent capability of being read out in an FDM/μ-MUX scheme. So far, arrays with up to 20,000 pixels with a multiplexing factor of 2000 : 1 have been demonstrated [322]. The pixel yield still lies below 80% and it can be due to inhomogeneities in the properties of the thin films [323] but it can be optimized through an accurate choice of the superconducting thin film [324] cautiously simulated design [325] (as opposed to interpolated) and *post-facto* leg trimming [326] and DC-bias [327].

### *9.2. Superconducting Nanowire Single Photon Detectors*

SNSPDs are thin and narrow superconducting nanowires patterned in a meander geometry to arrange them in a compact pixel. Quite like a TES, the SNSPD is kept at a temperature below its critical temperature but it is biased with a current which is close to, but smaller, than its critical current. When a particle strikes on the superconductor, it depletes it locally of Cooper pairs and produces a resistive hotspot. Such finite resistance produces a voltage drop across the SNSPD which can be measured. SNSPDs exhibit incredible quantum efficiency and pico-second time resolution, but exhibit no energy resolution and no photon-counting capabilities if not multiplexed (usually FDM) into arrays. As of July 2024, kilo-pixel arrays of SNSPDs are commercially available.

**Author Contributions:** Conceptualization, M.D.L.; writing—original draft preparation, M.D.L. except: F.P. (Sections 2.1–2.4, 5 and 5.4), P.D.B. (Section 3.8), E.D.G. (Sections 3.7.2 and 3.9), T.L. (Sections 5.1–5.3) and C.P. (Section 3.6.2); writing—review and editing, M.D.L.; visualization, M.D.L. and F.P.; supervision, M.D.L.; project administration, M.D.L. All authors have read and agreed to the published version of the manuscript.

**Funding:** This research was partially funded by Italian Space Agency under ASI Grants No. 2020-9-HH.0 and 2020-25-HH.0 (M.D.L.), by the Piano Nazionale di Ripresa e Resilienza, Ministero dell'Universitá e della Ricerca (PNRR MUR) Project under Grant PE0000023-NQSTI (C.P.), and by the National Recovery and Resilience Plan (NRRP), Mission 4, Component 2, Investment 1.1, Call PRIN 2022 by the Italian Ministry of University and Research (MUR), funded by the European Union—NextGenerationEU – EQUATE Project, "Defect engineered graphene for electro-thermal quantum technology"—Grant Assignment Decree No. 2022Z7RHRS (F.P.).

**Acknowledgments:** The authors acknowledge F. Gatti for the fabrication of the TES shown in Figure 8 and the NIST, Boulder Quantum Sensors Division for the fabrication of the TES shown in Figure 9.

**Conflicts of Interest:** The authors declare no conflicts of interest.

## Abbreviations

The following abbreviations are used in this manuscript:

| | |
|---|---|
| ABS | Atacama B-mode Search |
| ACT | Atacama Cosmology Telescope |
| AliCPT | Ali CMB Polarization Telescope |
| ALMA | Atacama Large Millimeter/submillimeter Array |
| ALPS II | Any Light Particle Search II |
| ASI | Agenzia Spaziale Italiana |
| Athena | Advanced Telescope for High-ENergy Astrophysics |
| BBO | Beta Barium Borate |
| BCS | Bardeen Cooper Schreifer |
| BICEP | Background Imaging of Cosmic Extragalactic Polarization |
| CCD | Charge Coupled Device |
| CDM | Code Division Multiplexing |
| CE$\nu$NS | Coherent Elastic Neutrino Nucleus Scattering |
| CLASS | Cosmology Large Angular Scale Surveyor |
| CLSM | Confocal Laser Scanning Microscope |
| CMB | Cosmic Microwave Background |
| CMB-S4 | Cosmic Microwave Background - Stage 4 |

| | |
|---|---|
| CMOS | Complimentary Metal-Oxide-Semiconductor |
| CSS | Coherent State Superposition |
| CPW | Coplanar Waveguide |
| CRESST | Cryogenic Rare Event Search using Superconducting Thermometers |
| CUPID | CUORE Upgrade with Particle IDentification |
| DAC | Digital-to-Analog Converter |
| DM | Dark Matter |
| EBEX | E and B EXperiment |
| EBIT | Electron Beam Ion Trap |
| EC | Electron Capture |
| ESA | European Space Agency |
| FIP | Far-Infrared Polarimeter |
| FoV | Field of View |
| FDM | Frequency Division Multiplexing |
| GISMO | Goddard IRAM Superconducting Millimeter Observer |
| HEMT | High Electron Mobility Transistor |
| HeRALD | Helium Roton Apparatus for Light Dark matter |
| HIXI | High Definition X-ray Imager |
| HOM | Hong-Ou-Mandel |
| HPGe | High Purity germanium |
| IAEA | International Atomic Energy Agency |
| IC | Integrated Circuits |
| INFN | Istituto Nazionale Fisica Nucleare |
| ISTED | Inductive Superconducting Transition Edge Sensor |
| JPARC | Japan Proton Accelerator Research Complex |
| JWST | James Webb Space Telescope |
| LANL | Los Alamos National Laboratory |
| LAT | Large Aperture Telescope |
| LCLS | Linac Coherent Light Source |
| LFT | Low Frequency Telescope |
| LiteBIRD | Lite (Light) satellite for the study of B-mode polarization and Inflation from cosmic background Radiation Detection |
| LSPE | Large-Scale Polarization Explorer |
| LSW | Light Shining through a Wall |
| LXM | Lynx X-ray Microcalorimeter |
| μ-MUX | Microwave Multiplexing |
| MBAC | Millimeter Bolometer Array Camera |
| MHFT | Medium and High Frequency Telescope |
| MINT | Microscope for Integrated circuit NanoTomography |
| MISC-T | Mid-Infrared Spectrometer Camera Transit |
| MKID | Microwave Kinetic Inductance Detector |
| NDA | Non-Destructive Assay |
| NEP | Noise Equivalent Power |
| NETF | Negative electro-thermal Feedback |
| NETS | NIST EBIT TES Spectrometer |
| NIST | National Institute of Standards and Technology |
| NSENSE | Non-destructive Statistical Estimation of Nanoscale Structures and Electronics |
| NTD | Neutron Transmutation Doped |
| OMT | Ortho-Mode Transducer |
| OSS | Origins Survey Spectrometer |
| PIXE | Particle-Induced X-ray Emission |
| PMT | Photo-multiplier Tube |
| POLARBEAR | POLARization of the Background Radiation |
| PSD | Power Spectral Density |
| PSI | Paul Scherrer Institut |

| | |
|---|---|
| QKD | Quantum Key Distribution |
| QUBIC | Q and U Bolometric Interferometer for Cosmology |
| RIXS | Resonant Inelastic X-ray Scattering |
| SAT | Small Aperture Telescope |
| SCUBA-2 | Submillimetre Common-User Bolometer Array 2 |
| SDD | Silicon Drift Detector |
| SEM | Scanning Electron Microscope |
| SLEDGEHAMMER | Spectrometer to Leverage Extensive Development of Gamma-ray TESs for Huge Arrays using Microwave Multiplexed Enabled Readout |
| SNLS | Sinchrotron National Light Source |
| SNSPD | Superconducting Nanowire Single Photon Detector |
| SNR | Signal-to-Noise Ratio |
| SPDT | Single Pole Double Throw |
| SOFIA | Spectromenter Optimized for Facility Integrated Applications |
| SPICA | Space Infrared Telescope for Cosmology and Astrophysics |
| SPICE | Sub-eV Polar Interactions Cryogenic Experiment |
| SPT | South Pole Telescope |
| SPTPol | South Pole Telescope Polarimeter |
| SQUID | Superconducting QUantum Interference Device |
| STEM | Scanning Transmission Electron Microscope |
| STFC | (UK) Science and Technology Facilities Council |
| STRIP | Survey TeneRIfe Polarimeter |
| SWIPE | Short Wavelength Instrument for the Polarization Explorer |
| TDM | Time Division Multiplexing |
| TES | Transition Edge Sensor |
| TOD | Time-Ordered Data |
| TOMCAT | Tomographic Circuit Analysis Tool |
| WFI | Wide Field Instrument |
| WHIM | Warm-Hot Interstellar Medium |
| WIMP | Weakly Interacting Massive Particle |
| X-IFU | X-ray Integral Field Unit |
| XANES | X-ray Absorption Near-Edge Structure |
| XAS | X-ray Absorption Spectroscopy |
| XES | X-ray Emission Spectroscopy |
| XGS | X-ray Grating Spectrometer |

## References


1. Enss, C.E. *Cryogenic Particle Detection*; Springer: Berlin/Heidelberger, Germany, 2005; Volume 99.
2. Enss, C.; Mccammon, D. Physical principles of low temperature detectors: Ultimate performance limits and current detector capabilities. *J. Low Temp. Phys.* **2008**, *151*, 5–24. [CrossRef]
3. Gottardi, L.; Nagayashi, K. A review of X-ray microcalorimeters based on superconducting Transition Edge Sensors for astrophysics and particle physics. *Appl. Sci.* **2021**, *11*, 3793. [CrossRef]
4. Nucciotti, A. The use of low temperature detectors for direct measurements of the mass of the electron neutrino. *Adv. High Energy Phys.* **2016**, *2016*, 9153024. [CrossRef]
5. Pirro, S.; Mauskopf, P. Advances in bolometer technology for fundamental physics. *Annu. Rev. Nucl. Part. Sci.* **2017**, *67*, 161–181. [CrossRef]
6. Poda, D.; Giuliani, A. Low background techniques in bolometers for double-beta decay search. *Int. J. Mod. Phys. A* **2017**, *32*, 1743012. [CrossRef]
7. Poda, D. Scintillation in low-temperature particle detectors. *Physics* **2021**, *3*, 473–535. [CrossRef]
8. Koehler, K.E. Low temperature microcalorimeters for decay energy spectroscopy. *Appl. Sci.* **2021**, *11*, 4044. [CrossRef]
9. Ullom, J.N.; Bennett, D.A. Review of superconducting transition-edge sensors for X-ray and gamma-ray spectroscopy. *Supercond. Sci. Technol.* **2015**, *28*, 084003. [CrossRef]
10. Tinkham, M. *Introduction to Superconductivity*; Dover Publications: Mineola, NY, USA, 2004.
11. Meissner, W.; Ochsenfeld, R. Ein neuer Effekt bei Eintritt der Supraleitfähigkeit. *Naturwissenschaften* **1933**, *21*, 787–788. [CrossRef]
12. London, F. On the Problem of the Molecular Theory of Superconductivity. *Phys. Rev.* **1948**, *74*, 562–573. [CrossRef]
13. Doll, R.; Näbauer, M. Experimental Proof of Magnetic Flux Quantization in a Superconducting Ring. *Phys. Rev. Lett.* **1961**, *7*, 51–52. [CrossRef]

14. Deaver, B.S.; Fairbank, W.M. Experimental Evidence for Quantized Flux in Superconducting Cylinders. *Phys. Rev. Lett.* **1961**, *7*, 43–46. [CrossRef]
15. Schrieffer, J. *Theory of Superconductivity*; Advanced Books Classics; Avalon Publishing: London, UK, 1999.
16. Keesom, W.; Kok, J. Measurements of the specific heat of thallium at liquid helium temperatures. *Physica* **1934**, *1*, 175–181. [CrossRef]
17. Giaever, I. Electron Tunneling Between Two Superconductors. *Phys. Rev. Lett.* **1960**, *5*, 464–466. [CrossRef]
18. Biondi, M.A.; Garfunkel, M.P. Millimeter Wave Absorption in Superconducting Aluminum. I. Temperature Dependence of the Energy Gap. *Phys. Rev.* **1959**, *116*, 853–861. [CrossRef]
19. Glover, R.E.; Tinkham, M. Conductivity of Superconducting Films for Photon Energies between 0.3 and $40kT_c$. *Phys. Rev.* **1957**, *108*, 243–256. [CrossRef]
20. Bardeen, J.; Cooper, L.N.; Schrieffer, J.R. Microscopic Theory of Superconductivity. *Phys. Rev.* **1957**, *106*, 162–164. [CrossRef]
21. Cooper, L.N. Bound Electron Pairs in a Degenerate Fermi Gas. *Phys. Rev.* **1956**, *104*, 1189–1190. [CrossRef]
22. De Gennes, P.G. *Superconductivity of Metals and Alloys*; Advanced Book Classics; Perseus: Cambridge, MA, USA, 1999.
23. Usadel, K.D. Generalized Diffusion Equation for Superconducting Alloys. *Phys. Rev. Lett.* **1970**, *25*, 507–509. [CrossRef]
24. Anderson, P.W. Theory of dirty superconductors. *J. Phys. Chem. Solids* **1959**, *11*, 26–30. [CrossRef]
25. Fominov, Y.V.; Feigel'man, M. Superconductive properties of thin dirty superconductor–normal-metal bilayers. *Phys. Rev. B* **2001**, *63*, 094518. [CrossRef]
26. Brammertz, G.; Golubov, A.A.; Verhoeve, P.; den Hartog, R.; Peacock, A.; Rogalla, H. Critical temperature of superconducting bilayers: Theory and experiment. *Appl. Phys. Lett.* **2002**, *80*, 2955–2957. [CrossRef]
27. Cooper, L.N. Superconductivity in the Neighborhood of Metallic Contacts. *Phys. Rev. Lett.* **1961**, *6*, 689–690. [CrossRef]
28. Martinis, J.M.; Hilton, G.; Irwin, K.; Wollman, D. Calculation of TC in a normal-superconductor bilayer using the microscopic-based Usadel theory. *Nucl. Instrum. Methods Phys. Res. Sect. A Accel. Spectrom. Detect. Assoc. Equip.* **2000**, *444*, 23–27. [CrossRef]
29. Giazotto, F.; Heikkilä, T.T.; Luukanen, A.; Savin, A.M.; Pekola, J.P. Opportunities for mesoscopics in thermometry and refrigeration: Physics and applications. *Rev. Mod. Phys.* **2006**, *78*, 217–274. [CrossRef]
30. Pekola, J.P.; Heikkilä, T.T.; Savin, A.M.; Flyktman, J.T.; Giazotto, F.; Hekking, F.W.J. Limitations in Cooling Electrons using Normal-Metal-Superconductor Tunnel Junctions. *Phys. Rev. Lett.* **2004**, *92*, 056804. [CrossRef]
31. Bardeen, J.; Rickayzen, G.; Tewordt, L. Theory of the Thermal Conductivity of Superconductors. *Phys. Rev.* **1959**, *113*, 982–994. [CrossRef]
32. Pekola, J.P.; Karimi, B. Colloquium: Quantum heat transport in condensed matter systems. *Rev. Mod. Phys.* **2021**, *93*, 041001. [CrossRef]
33. Bergeret, F.S.; Silaev, M.; Virtanen, P.; Heikkilä, T.T. Colloquium: Nonequilibrium effects in superconductors with a spin-splitting field. *Rev. Mod. Phys.* **2018**, *90*, 041001. [CrossRef]
34. Andreev, A.F. The Thermal Conductivity of the Intermediate State in Superconductors. *JETP* **1964**, *19*, 12284.
35. Paolucci, F.; Buccheri, V.; Germanese, G.; Ligato, N.; Paoletti, R.; Signorelli, G.; Bitossi, M.; Spagnolo, P.; Falferi, P.; Rajteri, M.; et al. Development of highly sensitive nanoscale Transition Edge Sensors for gigahertz astronomy and dark matter search. *J. Appl. Phys.* **2020**, *128*, 194502. [CrossRef]
36. Andrews, D.H.; Brucksch, W.F.J.; Ziegler, W.T.; Blanchard, E.R. Attenuated Superconductors I. For Measuring Infra-Red Radiation. *Rev. Sci. Instrum.* **1942**, *13*, 281–292. [CrossRef]
37. Irwin, K.D. An application of electrothermal feedback for high resolution cryogenic particle detection. *Appl. Phys. Lett.* **1995**, *66*, 1998–2000. [CrossRef]
38. Irwin, K.D.; Hilton, G.C. Transition-edge sensors. In *Cryogenic Particle Detection*; Springer: Berlin/Heidelberg, Germany, 2005; pp. 63–150.
39. McMahon, J.; Beall, J.; Becker, D.; Cho, H.; Datta, R.; Fox, A.; Halverson, N.; Hubmayr, J.; Irwin, K.; Nibarger, J.; et al. Multi-chroic feed-horn coupled TES polarimeters. *J. Low Temp. Phys.* **2012**, *167*, 879–884. [CrossRef]
40. Likharev, K.K. Superconducting weak links. *Rev. Mod. Phys.* **1979**, *51*, 101–159. [CrossRef]
41. Pleikies, J.; Usenko, O.; Kuit, K.; Flokstra, J.; De Waard, A.; Frossati, G. SQUID developments for the Gravitational Wave antenna MiniGRAIL. *IEEE Trans. Appl. Supercond.* **2007**, *17*, 764–767. [CrossRef]
42. Ketchen, M.B.; Kopley, T.; Ling, H. Miniature SQUID susceptometer. *Appl. Phys. Lett.* **1984**, *44*, 1008–1010. [CrossRef]
43. Wikswo, J.P. SQUID magnetometers for biomagnetism and nondestructive testing: Important questions and initial answers. *IEEE Trans. Appl. Supercond.* **1995**, *5*, 74–120. [CrossRef]
44. Jenks, W.; Sadeghi, S.; Wikswo, J.P., Jr. SQUIDs for nondestructive evaluation. *J. Phys. D Appl. Phys.* **1997**, *30*, 293. [CrossRef]
45. Clarke, J.; Hatridge, M.; Mößle, M. SQUID-detected magnetic resonance imaging in microtesla fields. *Annu. Rev. Biomed. Eng.* **2007**, *9*, 389–413. [CrossRef] [PubMed]
46. Mück, M.; McDermott, R. Radio-frequency amplifiers based on dc SQUIDs. *Supercond. Sci. Technol.* **2010**, *23*, 093001. [CrossRef]
47. Tanaka, H.; Sekine, Y.; Saito, S.; Takayanagi, H. DC-SQUID readout for qubit. *Phys. C Supercond.* **2002**, *368*, 300–304. [CrossRef]
48. Irwin, K.D.; Huber, M. SQUID operational amplifier. *IEEE Trans. Appl. Supercond.* **2001**, *11*, 1265–1270. [CrossRef]
49. Tsang, W.T.; Van Duzer, T. Dc analysis of parallel arrays of two and three Josephson junctions. *J. Appl. Phys.* **1975**, *46*, 4573–4580. [CrossRef]

50. Huber, M.E.; Neil, P.A.; Benson, R.G.; Burns, D.A.; Corey, A.; Flynn, C.S.; Kitaygorodskaya, Y.; Massihzadeh, O.; Martinis, J.M.; Hilton, G. DC SQUID series array amplifiers with 120 MHz bandwidth (corrected). *IEEE Trans. Appl. Supercond.* **2001**, *11*, 4048–4053. [CrossRef]
51. Labarias, M.A.G.; Müller, K.H.; Mitchell, E.E. The effect of bias current configuration on the performance of SQUID arrays. *Supercond. Sci. Technol.* **2023**, *36*, 115016. [CrossRef]
52. Mukhanov, O.; Prokopenko, G.; Romanofsky, R. Quantum Sensitivity: Superconducting Quantum Interference Filter-Based Microwave Receivers. *IEEE Microw. Mag.* **2014**, *15*, 57–65. [CrossRef]
53. Welty, R.P.; Martinis, J.M. Two-stage integrated SQUID amplifier with series array output. *IEEE Trans. Appl. Supercond.* **1993**, *3*, 2605–2608. [CrossRef]
54. Kiviranta, M. Two-stage SQUID amplifier with bias current re-use. *arXiv* **2020**, arXiv:2012.15362.
55. Drung, D.; Hinnrichs, C.; Barthelmess, H.J. Low-noise ultra-high-speed dc SQUID readout electronics. *Supercond. Sci. Technol.* **2006**, *19*, S235. [CrossRef]
56. Cantor, R.; Lee, L.P.; Matlashov, A.; Vinetskiy, V. A low-noise, two-stage DC SQUID amplifier with high bandwidth and dynamic range. *IEEE Trans. Appl. Supercond.* **1997**, *7*, 3033–3036. [CrossRef]
57. Kiviranta, M. Low-dissipating push-pull SQUID amplifier for TES detector readout. *arXiv* **2018**, arXiv:1810.04706.
58. Uhlig, K. Cryogen-free dilution refrigerator with separate 1K cooling circuit. *AIP Conf. Proc.* **2012**, *1434*, 1823–1829. [CrossRef]
59. Callahan, J.; Mathes, R.; Kahn, A. Time-Division Multiplex in Radiotelegraphic Practice. *Proc. Inst. Radio Eng.* **1938**, *26*, 55–75. [CrossRef]
60. Battistelli, E.S.; Amiri, M.; Burger, B.; Halpern, M.; Knotek, S.; Ellis, M.; Gao, X.; Kelly, D.; Macintosh, M.; Irwin, K.; et al. Functional description of read out electronics for time-domain multiplexed bolometers for millimeter and sub-millimeter astronomy. *J. Low Temp. Phys.* **2008**, *151*, 908–914. [CrossRef]
61. Wu, X.; Yu, Q.; He, Y.; Liu, J.; Chen, W. Multiplexing technology based on SQUID for readout of superconducting transition-edge sensor arrays. *Chin. Phys. B* **2022**, *31*, 108501. [CrossRef]
62. Niemack, M.D.; Beyer, J.; Cho, H.; Doriese, W.; Hilton, G.; Irwin, K.; Reintsema, C.D.; Schmidt, D.R.; Ullom, J.N.; Vale, L.R. Code-division SQUID multiplexing. *Appl. Phys. Lett.* **2010**, *96*, 163509. [CrossRef]
63. Doriese, W.; Beall, J.; Duncan, W.; Ferreira, L.; Hilton, G.; Irwin, K.; Reintsema, C.; Ullom, J.; Vale, L.; Xu, Y. Progress toward kilopixel arrays: 3.8 eV microcalorimeter resolution in 8-channel SQUID multiplexer. *Nucl. Instrum. Methods Phys. Res. Sect. A Accel. Spectrom. Detect. Assoc. Equip.* **2006**, *559*, 808–810. [CrossRef]
64. Dreyer, J.G.; Arnold, K.; Lanting, T.M.; Dobbs, M.A.; Friedrich, S.; Lee, A.T.; Spieler, H.G. Frequency-Domain Multiplexed Readout for Superconducting Gamma-Ray Detectors. *IEEE Trans. Appl. Supercond.* **2007**, *17*, 633–636. [CrossRef]
65. Irwin, K.; Niemack, M.; Beyer, J.; Cho, H.; Doriese, W.; Hilton, G.; Reintsema, C.; Schmidt, D.; Ullom, J.; Vale, L. Code-division multiplexing of superconducting transition-edge sensor arrays. *Supercond. Sci. Technol.* **2010**, *23*, 034004. [CrossRef]
66. Irwin, K.D.; Cho, H.M.; Doriese, W.B.; Fowler, J.W.; Hilton, G.C.; Niemack, M.D.; Reintsema, C.D.; Schmidt, D.R.; Ullom, J.N.; Vale, L.R. Advanced code-division multiplexers for superconducting detector arrays. *J. Low Temp. Phys.* **2012**, *167*, 588–594. [CrossRef]
67. Cukierman, A.; Ahmed, Z.; Henderson, S.; Young, E.; Yu, C.; Barkats, D.; Brown, D.; Chaudhuri, S.; Cornelison, J.; D'Ewart, J.M.; et al. Microwave multiplexing on the Keck Array. *J. Low Temp. Phys.* **2020**, *199*, 858–866. [CrossRef]
68. Dober, B.; Ahmed, Z.; Arnold, K.; Becker, D.; Bennett, D.; Connors, J.; Cukierman, A.; D'Ewart, J.; Duff, S.; Dusatko, J.; et al. A microwave SQUID multiplexer optimized for bolometric applications. *Appl. Phys. Lett.* **2021**, *118*, 062601. [CrossRef]
69. McCammon, D. Thermal equilibrium calorimeters—An introduction. In *Cryogenic Particle Detection*; Springer: Berlin/Heidelberg, Germany, 2005; pp. 1–34.
70. Richards, P.L. Bolometers for infrared and millimeter waves. *J. Appl. Phys.* **1994**, *76*, 1–24. [CrossRef]
71. Boyle, W.; Rodgers Jr, K. Performance characteristics of a new low-temperature bolometer. *J. Opt. Soc. Am.* **1959**, *49*, 66–69. [CrossRef]
72. Mather, J.C. Bolometer noise: Nonequilibrium theory. *Appl. Opt.* **1982**, *21*, 1125–1129. [CrossRef]
73. Johnson, J.B. Thermal agitation of electricity in conductors. *Phys. Rev.* **1928**, *32*, 97. [CrossRef]
74. Perepelitsa, D.V. *Johnson Noise and Shot Noise*; MIT Department of Physics: Cambridge, MA, USA, 2006.
75. Lamarre, J.M. Photon noise in photometric instruments at far-infrared and submillimeter wavelengths. *Appl. Opt.* **1986**, *25*, 870–876. [CrossRef]
76. Shirokoff, E.D. The South Pole Telescope Bolometer Array and the Measurement of Secondary Cosmic Microwave Background Anisotropy at Small Angular Scales. Ph.D. Thesis, UC Berkeley, Berkeley, CA, USA, 2011.
77. Ullom, J.N.; Doriese, W.B.; Hilton, G.C.; Beall, J.A.; Deiker, S.; Duncan, W.; Ferreira, L.; Irwin, K.D.; Reintsema, C.D.; Vale, L.R. Characterization and reduction of unexplained noise in superconducting transition-edge sensors. *Appl. Phys. Lett.* **2004**, *84*, 4206–4208. [CrossRef]
78. Jethava, N.; Ullom, J.N.; Irwin, K.D.; Doriese, W.; Beall, J.; Hilton, G.; Vale, L.; Zink, B. Dependence of excess noise on the partial derivatives of resistance in superconducting Transition Edge Sensors. *AIP Conf. Proc.* **2009**, *1185*, 31–33.
79. Galeazzi, M. Fundamental noise processes in TES devices. *IEEE Trans. Appl. Supercond.* **2010**, *21*, 267–271. [CrossRef]
80. Gildemeister, J.M.; Lee, A.T.; Richards, P.L. Model for excess noise in voltage-biased superconducting bolometers. *Appl. Opt.* **2001**, *40*, 6229–6235. [CrossRef]

81. Dobbs, M.; Lueker, M.; Aird, K.; Bender, A.; Benson, B.; Bleem, L.; Carlstrom, J.; Chang, C.; Cho, H.M.; Clarke, J.; et al. Frequency multiplexed superconducting quantum interference device readout of large bolometer arrays for cosmic microwave background measurements. *Rev. Sci. Instrum.* **2012**, *83*, 073113. [CrossRef]
82. Lueker, M.; Benson, B.A.; Chang, C.L.; Cho, H.M.; Dobbs, M.; Holzapfel, W.L.; Lanting, T.; Lee, A.T.; Mehl, J.; Plagge, T.; et al. Thermal design and characterization of transition-edge sensor (TES) bolometers for frequency-domain multiplexing. *IEEE Trans. Appl. Supercond.* **2009**, *19*, 496–500. [CrossRef]
83. Zmuidzinas, J. Superconducting microresonators: Physics and applications. *Annu. Rev. Condens. Matter Phys.* **2012**, *3*, 169–214. [CrossRef]
84. De Lucia, M.; Ulbricht, G.; Baldwin, E.; Piercy, J.; Creaner, O.; Bracken, C.; Ray, T. Limitations to the energy resolution of single-photon sensitive microwave kinetic inductance detectors. *AIP Adv.* **2023**, *13*, 125026. [CrossRef]
85. Yoshihara, F.; Kanno, I.; Shinada, K. Rf-SQUID microcalorimeter. *Supercond. Sci. Technol.* **2003**, *16*, 1257. [CrossRef]
86. Mates, J.; Becker, D.T.; Bennett, D.A.; Dober, B.J.; Gard, J.D.; Hilton, G.C.; Swetz, D.S.; Vale, L.R.; Ullom, J.N. Crosstalk in microwave SQUID multiplexers. *Appl. Phys. Lett.* **2019**, *115*, 202601. [CrossRef]
87. Noroozian, O.; Day, P.K.; Eom, B.H.; Leduc, H.G.; Zmuidzinas, J. Crosstalk reduction for superconducting microwave resonator arrays. *IEEE Trans. Microw. Theory Tech.* **2012**, *60*, 1235–1243. [CrossRef]
88. Hirayama, F.; Irimatsugawa, T.; Yamamori, H.; Kohjiro, S.; Sato, A.; Nagasawa, S.; Fukuda, D.; Sasaki, H.; Hidaka, M.; Sato, Y.; et al. Interchannel crosstalk and nonlinearity of microwave SQUID multiplexers. *IEEE Trans. Appl. Supercond.* **2016**, *27*, 2500205. [CrossRef]
89. Groh, J.C.; Ahmed, Z.; Henderson, S.W.; Hubmayr, J.; Mates, J.A.; Silva-Feaver, M.; Ullom, J.; Yu, C. Crosstalk effects in microwave SQUID multiplexed TES bolometer readout. *J. Low Temp. Phys.* **2024**, *216*, 225–236. [CrossRef]
90. Piro, L.; Amati, L.; Barbera, M.; Borgani, S.; Bazzano, A.; Branchini, E.; Brunetti, G.; Campana, S.; Caroli, E.; Cocchi, M.; et al. ESTREMO/WFXRT: Extreme physics in the transient and evolving cosmos. In Proceedings of the Space Telescopes and Instrumentation II: Ultraviolet to Gamma Ray, Orlando, FL, USA, 24–31 May 2006; SPIE: Bellingham, WA, USA, 2006; Volume 6266, pp. 163–174.
91. Piro, L. The future of GRB investigation from ground and space. *Philos. Trans. R. Soc. A Math. Phys. Eng. Sci.* **2007**, *365*, 1399–1409. [CrossRef]
92. Barret, D.; Trong, T.L.; Den Herder, J.W.; Piro, L.; Barcons, X.; Huovelin, J.; Kelley, R.; Mas-Hesse, J.M.; Mitsuda, K.; Paltani, S.; et al. The Athena X-ray integral field unit (X-IFU). In Proceedings of the Space Telescopes and Instrumentation 2016: Ultraviolet to Gamma Ray, Edinburgh, UK, 18 July 2016; SPIE: Bellingham, WA, USA, 2016; Volume 9905, pp. 714–754.
93. Meidinger, N.; Nandra, K.; Plattner, M. Development of the Wide Field Imager instrument for ATHENA. In Proceedings of the Space Telescopes and Instrumentation 2018: Ultraviolet to Gamma Ray, Austin, TX, USA, 10–15 June 2018; SPIE: Bellingham, WA, USA, 2018; Volume 10699, pp. 312–323.
94. Barret, D.; Albouys, V.; Herder, J.W.d.; Piro, L.; Cappi, M.; Huovelin, J.; Kelley, R.; Mas-Hesse, J.M.; Paltani, S.; Rauw, G.; et al. The Athena X-ray Integral Field Unit: A consolidated design for the system requirement review of the preliminary definition phase. *Exp. Astron.* **2023**, *55*, 373–426. [CrossRef]
95. Khosropanah, P.; Taralli, E.; Gottardi, L.; De Vries, C.; Nagayoshi, K.; Ridder, M.; Akamatsu, H.; Bruijn, M.; Gao, J.R. Development of TiAu TES X-ray calorimeters for the X-IFU on ATHENA space observatory. In Proceedings of the Space Telescopes and Instrumentation 2018: Ultraviolet to Gamma Ray, Austin, TX, USA, 10–15 June 2018; SPIE: Bellingham, WA, USA, 2018; Volume 10699, pp. 386–396.
96. D'Andrea, M.; Ravensberg, K.; Argan, A.; Brienza, D.; Lotti, S.; Macculi, C.; Minervini, G.; Piro, L.; Torrioli, G.; Chiarello, F.; et al. ATHENA X-IFU demonstration model: First joint operation of the main TES array and its cryogenic AntiCoincidence detector (CryoAC). *J. Low Temp. Phys.* **2022**, *209*, 433–440. [CrossRef]
97. Durkin, M.; Adams, J.S.; Bandler, S.R.; Chervenak, J.A.; Chaudhuri, S.; Dawson, C.S.; Denison, E.V.; Doriese, W.B.; Duff, S.M.; Finkbeiner, F.M.; et al. Demonstration of Athena X-IFU compatible 40-row time-division-multiplexed readout. *IEEE Trans. Appl. Supercond.* **2019**, *29*, 2101005. [CrossRef]
98. Bandler, S.R.; Chervenak, J.A.; Datesman, A.M.; Devasia, A.M.; DiPirro, M.; Sakai, K.; Smith, S.J.; Stevenson, T.R.; Yoon, W.; Bennett, D.; et al. Lynx X-ray microcalorimeter. *J. Astron. Telesc. Instrum. Syst.* **2019**, *5*, 021017. [CrossRef]
99. Gaskin, J.A.; Swartz, D.A.; Vikhlinin, A.; Özel, F.; Gelmis, K.E.; Arenberg, J.W.; Bandler, S.R.; Bautz, M.W.; Civitani, M.M.; Dominguez, A.; et al. Lynx X-ray observatory: An overview. *J. Astron. Telesc. Instrum. Syst.* **2019**, *5*, 021001. [CrossRef]
100. Gaskin, J.A.; Dominguez, A.; Gelmis, K.; Mulqueen, J.J.; Swartz, D.; McCarley, K.; Özel, F.; Vikhlinin, A.; Schwartz, D.; Tananbaum, H.; et al. The Lynx X-ray Observatory: Concept study overview and status. In Proceedings of the Space Telescopes and Instrumentation 2018: Ultraviolet to Gamma Ray, Austin, TX, USA, 10–15 June 2018; SPIE: Bellingham, WA, USA, 2018; Volume 10699, pp. 120–129.
101. Falcone, A.D.; Kraft, R.P.; Bautz, M.W.; Gaskin, J.A.; Mulqueen, J.A.; Swartz, D.A.; Technology Definition Team, f.t.L.S. Overview of the high-definition X-ray imager instrument on the Lynx X-ray surveyor. *J. Astron. Telesc. Instrum. Syst.* **2019**, *5*, 021019. [CrossRef]
102. McEntaffer, R.L. Reflection grating concept for the Lynx X-ray grating spectrograph. *J. Astron. Telesc. Instrum. Syst.* **2019**, *5*, 021002. [CrossRef]

103. Smith, S.J.; Adams, J.; Bandler, S.; Beaumont, S.; Chervenak, J.; Datesman, A.; Finkbeiner, F.; Hummatov, R.; Kelly, R.; Kilbourne, C.; et al. Toward 100,000-pixel microcalorimeter arrays using multi-absorber transition-edge sensors. *J. Low Temp. Phys.* **2020**, *199*, 330–338. [CrossRef]
104. Leisawitz, D.; Amatucci, E.; Allen, L.; Arenberg, J.; Armus, L.; Battersby, C.; Bauer, J.; Beaman, B.G.; Bell, R.; Beltran, P.; et al. Origins Space Telescope: Baseline mission concept. *J. Astron. Telesc. Instrum. Syst.* **2021**, *7*, 011002. [CrossRef]
105. Battersby, C.; Armus, L.; Bergin, E.; Kataria, T.; Meixner, M.; Pope, A.; Stevenson, K.B.; Cooray, A.; Leisawitz, D.; Scott, D.; et al. The Origins space telescope. *Nat. Astron.* **2018**, *2*, 596–599. [CrossRef]
106. Bradford, C.M.; Cameron, B.; Moore, B.; Hailey-Dunsheath, S.; Amatucci, E.; Bradley, D.; Corsetti, J.; Leisawitz, D.; DiPirro, M.; Tuttle, J.; et al. Origins Survey Spectrometer: Revealing the hearts of distant galaxies and forming planetary systems with far-IR spectroscopy. *J. Astron. Telesc. Instrum. Syst.* **2021**, *7*, 011017. [CrossRef]
107. Meixner, M.; Staguhn, J.; Vieira, J.; Amatucci, E.; DiPirro, M.; Bradley, D.; Cooray, A.; Battersby, C.; Sandstrom, K.; STDT, O.S.T.; et al. Origins Space Telescope (Origins): Far-infrared Imager and Polarimeter (FIP). In *American Astronomical Society Meeting Abstracts# 235*; Bulletin of the American Astronomical Society: Washington, DC, USA, 2020; Volume 235, p. 171.05.
108. Roellig, T.L.; McMurtry, C.; Greene, T.; Matsuo, T.; Sakon, I.; Staguhn, J. Mid-infrared detector development for the Origins Space Telescope. *J. Astron. Telesc. Instrum. Syst.* **2020**, *6*, 041503. [CrossRef]
109. Nagler, P.C.; Sadleir, J.E.; Wollack, E.J. Transition-edge sensor detectors for the Origins space telescope. *J. Astron. Telesc. Instrum. Syst.* **2021**, *7*, 011005. [CrossRef]
110. Roelfsema, P.R.; Shibai, H.; Armus, L.; Arrazola, D.; Audard, M.; Audley, M.D.; Bradford, C.; Charles, I.; Dieleman, P.; Doi, Y.; et al. SPICA—A Large Cryogenic Infrared Space Telescope: Unveiling the Obscured Universe. *Publ. Astron. Soc. Aust.* **2018**, *35*. [CrossRef]
111. Goicoechea, J.R.; Isaak, K.; Swinyard, B. Exoplanet research with SAFARI: A far-IR imaging spectrometer for SPICA. *arXiv* **2009**, arXiv:0901.3240.
112. Mauskopf, P.; Ade, P.; Beyer, J.; Bruijn, M.; Gao, J.; Glowacka, D.; Goldie, D.; Griffin, D.; Griffin, M.; Hoevers, H.; et al. A TES focal plane for SPICA-SAFARI. In Proceedings of the 21st International Symposium on Space Terahertz Technology 2010, ISSTT 2010, Oxford and Didcot, UK, 23–25 March 2010; pp. 23–25.
113. Audley, M.D.; Huijser, G.F.; de Lange, G.; Orlando, A. Optical measurements of ultra-sensitive far-infrared TES bolometers with FDM readout. In Proceedings of the Millimeter, Submillimeter, and Far-Infrared Detectors and Instrumentation for Astronomy XI, Montreal, QC, Canada, 31 August 2022; SPIE: Bellingham, WA, USA, 2022; Volume 12190, pp. 715–719.
114. Khosropanah, P.; Suzuki, T.; Ridder, M.; Hijmering, R.; Akamatsu, H.; Gottardi, L.; Van Der Kuur, J.; Gao, J.; Jackson, B. Ultra-low noise TES bolometer arrays for SAFARI instrument on SPICA. In Proceedings of the Millimeter, Submillimeter, and Far-Infrared Detectors and Instrumentation for Astronomy VIII, Edinburgh, UK, 26 June–1 July 2016; SPIE: Bellingham, WA, USA, 2016; Volume 9914, pp. 49–53.
115. Khosropanah, P.; Dirks, B.; Parra-Borderías, M.; Ridder, M.; Hijmering, R.; Van der Kuur, J.; Gottardi, L.; Bruijn, M.; Popescu, M.; Gao, J.; et al. Low-noise Transition Edge Sensor (TES) for SAFARI instrument on SPICA. In Proceedings of the Millimeter, Submillimeter, and Far-Infrared Detectors and Instrumentation for Astronomy V, San Diego, CA, USA, 27 June–2 July 2010; SPIE: Bellingham, WA, USA, 2010; Volume 7741, pp. 163–171.
116. Walton, A.; Parkes, W.; Terry, J.; Dunare, C.; Stevenson, J.; Gundlach, A.; Hilton, G.; Irwin, K.; Ullom, J.; Holland, W.; et al. Design and fabrication of the detector technology for SCUBA-2. *IEEE Proc.-Sci. Meas. Technol.* **2004**, *151*, 110–120. [CrossRef]
117. Audley, M.; Holland, W.; Duncan, W.; Atkinson, D.; Cliffe, M.; Ellis, M.; Gao, X.; Gostick, D.; Hodson, T.; Kelly, D.; et al. SCUBA-2: A large-format TES array for submillimetre astronomy. *Nucl. Instrum. Methods Phys. Res. Sect. A Accel. Spectrom. Detect. Assoc. Equip.* **2004**, *520*, 479–482. [CrossRef]
118. Bintley, D.; Holland, W.S.; MacIntosh, M.J.; Friberg, P.; Bell, G.S.; Berke, D.A.; Berry, D.S.; Berthold, R.M.; Cookson, J.L.; Coulson, I.M.; et al. SCUBA-2: An update on the performance of the 10,000 pixel bolometer camera after two years of science operation at the JCMT. In Proceedings of the Millimeter, Submillimeter, and Far-Infrared Detectors and Instrumentation for Astronomy VII, Montréal, QC, Canada, 22–27 June 2014; SPIE: Bellingham, WA, USA, 2014; Volume 9153, pp. 42–56.
119. Casey, C.M.; Chen, C.C.; Cowie, L.L.; Barger, A.J.; Capak, P.; Ilbert, O.; Koss, M.; Lee, N.; Le Floc'h, E.; Sanders, D.B.; et al. Characterization of Scuba-2 450 μm and 850 μm selected galaxies in the COSMOS field. *Mon. Not. R. Astron. Soc.* **2013**, *436*, 1919–1954. [CrossRef]
120. Mairs, S.; Dempsey, J.T.; Bell, G.S.; Parsons, H.; Currie, M.J.; Friberg, P.; Jiang, X.J.; Tetarenko, A.J.; Bintley, D.; Cookson, J.; et al. A Decade of SCUBA-2: A Comprehensive Guide to Calibrating 450 μm and 850 μm Continuum Data at the JCMT. *Astron. J.* **2021**, *162*, 191. [CrossRef]
121. Garratt, T.; Geach, J.; Tamura, Y.; Coppin, K.; Franco, M.; Ao, Y.; Chen, C.C.; Cheng, C.; Clements, D.; Dai, Y.; et al. The SCUBA-2 Large eXtragalactic Survey: 850 μm map, catalogue and the bright-end number counts of the XMM-LSS field. *Mon. Not. R. Astron. Soc.* **2023**, *520*, 3669–3687. [CrossRef]
122. Bennett, C.L.; Boggess, N.; Cheng, E.; Hauser, M.; Kelsall, T.; Mather, J.; Moseley Jr, S.; Murdock, T.L.; Shafer, R.A.; Silverberg, R.F.; et al. Scientific results from the Cosmic Background Explorer (COBE) (microwave/infrared). *Proc. Natl. Acad. Sci. USA* **1993**, *90*, 4766–4773. [CrossRef] [PubMed]

123. Staguhn, J.G.; Benford, D.J.; Allen, C.A.; Maher, S.F.; Sharp, E.H.; Ames, T.J.; Arendt, R.G.; Chuss, D.T.; Dwek, E.; Fixsen, D.J.; et al. Instrument performance of GISMO: A 2 millimeter TES bolometer camera used at the IRAM 30 m Telescope. In Proceedings of the Millimeter and Submillimeter Detectors and Instrumentation for Astronomy IV, Marseille, France, 26–28 June 2008; SPIE: Bellingham, WA, USA, 2008; Volume 7020, pp. 52–60.
124. Magnelli, B.; Karim, A.; Staguhn, J.; Kovács, A.; Jiménez-Andrade, E.; Casey, C.; Zavala, J.; Schinnerer, E.; Sargent, M.; Aravena, M.; et al. The IRAM/GISMO 2 mm Survey in the COSMOS Field. *Astrophys. J.* **2019**, *877*, 45. [CrossRef]
125. Casey, C.M.; Zavala, J.A.; Manning, S.M.; Aravena, M.; Béthermin, M.; Caputi, K.I.; Champagne, J.B.; Clements, D.L.; Drew, P.; Finkelstein, S.L.; et al. Mapping Obscuration to Reionization with ALMA (MORA): 2 mm Efficiently Selects the Highest-redshift Obscured Galaxies. *Astrophys. J.* **2021**, *923*, 215. [CrossRef]
126. Giard, M.; Casoli, F.; Paletou, F.; Maffei, B.; Ade, P.; Calderon, C.; Challinor, A.; De Bernardis, P.; Dunlop, L.; Gear, W.; et al. CLOVER: The CMB polarization observer. *Eur. Astron. Soc. Publ. Ser.* **2005**, *14*, 251–256.
127. Taylor, A.C.; Challinor, A.; Goldie, D.; Grainge, K.; Jones, M.; Lasenby, A.; Withington, S.; Yassin, G.; Gear, W.K.; Piccirillo, L.; et al. CLOVER—A new instrument for measuring the B-mode polarization of the CMB. *arXiv* **2004**, arXiv:astro-ph/0407148.
128. North, C.; Ade, P.A.; Audley, M.; Baines, C.; Battye, R.; Brown, M.; Cabella, P.; Calisse, P.G.; Challinor, A.; Duncan, W.; et al. Clover-measuring the CMB B-mode polarization. In Proceedings of the 18th International Symposium on Space Terahertz Technology 2007, ISSTT 2007, Pasadena, CA, USA, 21–23 March 2007; pp. 238–243.
129. Piccirillo, L.; Ade, P.; Audley, M.; Baines, C.; Battye, R.; Brown, M.; Calisse, P.; Challinor, A.; Duncan, W.; Ferreira, P.; et al. The CLOVER experiment. In Proceedings of the Millimeter and Submillimeter Detectors and Instrumentation for Astronomy IV, Marseille, France, 26–28 June 2008; SPIE: Bellingham, WA, USA, 2008; Volume 7020, pp. 385–394.
130. Audley, M.D.; Glowacka, D.; Goldie, D.J.; Tsaneva, V.; Withington, S.; Grimes, P.K.; North, C.E.; Yassin, G.; Piccirillo, L.; Ade, P.; et al. Performance of microstrip-coupled TES bolometers with finline transitions. In Proceedings of the Millimeter and Submillimeter Detectors and Instrumentation for Astronomy IV, Marseille, France, 26–28 June 2008; SPIE: Bellingham, WA, USA, 2008; Volume 7020, pp. 205–216.
131. Audley, M.D.; Glowacka, D.; Goldie, D.J.; Tsaneva, V.N.; Withington, S.; Grimes, P.K.; North, C.; Yassin, G.; Piccirillo, L.; Pisano, G.; et al. Microstrip-coupled TES bolometers for CLOVER. *Gravitat. Waves* **2008**, *2*, 3.
132. Fowler, J.W. The atacama cosmology telescope project. In Proceedings of the Millimeter and Submillimeter Detectors for Astronomy II, Glasgow, UK, 21–25 June 2004; SPIE: Bellingham, WA, USA, 2004; Volume 5498, pp. 1–10.
133. Swetz, D.; Ade, P.A.; Allen, C.; Amiri, M.; Appel, J.; Battistelli, E.S.; Burger, B.; Chervenak, J.; Dahlen, A.; Das, S.; et al. Instrument design and characterization of the millimeter Bolometer Array Camera on the Atacama Cosmology Telescope. In Proceedings of the Millimeter and Submillimeter Detectors and Instrumentation for Astronomy IV, Marseille, France, 26–28 June 2008; SPIE: Bellingham, WA, USA, 2008; Volume 7020, pp. 84–95.
134. Marriage, T.; Chervenak, J.; Doriese, W. Testing and assembly of the detectors for the Millimeter Bolometer Array Camera on ACT. *Nucl. Instrum. Methods Phys. Res. Sect. A Accel. Spectrom. Detect. Assoc. Equip.* **2006**, *559*, 551–553. [CrossRef]
135. Niemack, M.D.; Ade, P.A.; Aguirre, J.; Barrientos, F.; Beall, J.; Bond, J.; Britton, J.; Cho, H.; Das, S.; Devlin, M.; et al. ACTPol: A polarization-sensitive receiver for the Atacama Cosmology Telescope. In Proceedings of the Millimeter, Submillimeter, and Far-Infrared Detectors and Instrumentation for Astronomy V, San Diego, CA, USA, 27 June–2 July 2010; SPIE: Bellingham, WA, USA, 2010; Volume 7741, pp. 537–557.
136. Simon, S.; Beall, J.; Cothard, N.; Duff, S.; Gallardo, P.; Ho, S.; Hubmayr, J.; Koopman, B.; McMahon, J.; Nati, F.; et al. The advanced ACTPol 27/39 GHz array. *J. Low Temp. Phys.* **2018**, *193*, 1041–1047. [CrossRef]
137. Das, S.; Sherwin, B.D.; Aguirre, P.; Appel, J.W.; Bond, J.R.; Carvalho, C.S.; Devlin, M.J.; Dunkley, J.; Dunner, R.; Essinger-Hileman, T.; et al. Detection of the power spectrum of cosmic microwave background lensing by the atacama cosmology telescope. *arXiv* **2011**, arXiv:1103.2124. [CrossRef] [PubMed]
138. Marriage, T.A.; Acquaviva, V.; Ade, P.A.; Aguirre, P.; Amiri, M.; Appel, J.W.; Barrientos, L.F.; Battistelli, E.S.; Bond, J.R.; Brown, B.; et al. The Atacama Cosmology Telescope: Sunyaev–Zel'Dovich-Selected Galaxy Clusters at 148 GHz in the 2008 Survey. *Astrophys. J.* **2011**, *737*, 61. [CrossRef]
139. Zhao, Y.; Allen, C.; Amiri, M.; Appel, J.; Battistelli, E.S.; Burger, B.; Chervenak, J.; Dahlen, A.; Denny, S.; Devlin, M.; et al. Characterization of Transition Edge Sensors for the Millimeter Bolometer Array Camera on the Atacama Cosmology Telescope. In Proceedings of the Millimeter and Submillimeter Detectors and Instrumentation for Astronomy IV, Marseille, France, 26–28 June 2008; SPIE: Bellingham, WA, USA, 2008; Volume 7020, pp. 228–238.
140. Grace, E.; Beall, J.; Cho, H.; Devlin, M.; Fox, A.; Hilton, G.; Hubmayr, J.; Irwin, K.; Klein, J.; Li, D.; et al. Characterization and performance of a kilo-TES sub-array for ACTPol. *J. Low Temp. Phys.* **2014**, *176*, 705–711. [CrossRef]
141. Louis, T.; Grace, E.; Hasselfield, M.; Lungu, M.; Maurin, L.; Addison, G.E.; Ade, P.A.; Aiola, S.; Allison, R.; Amiri, M.; et al. The Atacama Cosmology Telescope: Two-season ACTPol spectra and parameters. *J. Cosmol. Astropart. Phys.* **2017**, *2017*, 031. [CrossRef]
142. Choi, S.K.; Austermann, J.; Beall, J.A.; Crowley, K.T.; Datta, R.; Duff, S.M.; Gallardo, P.A.; Ho, S.; Hubmayr, J.; Koopman, B.J.; et al. Characterization of the mid-frequency arrays for advanced ACTPol. *J. Low Temp. Phys.* **2018**, *193*, 267–275. [CrossRef]
143. Westbrook, B.; Prasad, B.; Raum, C.R.; Lee, A.T.; Suzuki, A.; Hubmayr, J.; Duff, S.M.; Link, M.J.; Lucas, T.J. Thermal Annealing of AlMn Transition Edge Sensors for Optimization in Cosmic Microwave Background Experiments. *J. Low Temp. Phys.* **2024**, *216*, 264–272. [CrossRef]

144. Li, D.; Austermann, J.E.; Beall, J.A.; Becker, D.T.; Duff, S.M.; Gallardo, P.A.; Henderson, S.W.; Hilton, G.C.; Ho, S.P.; Hubmayr, J.; et al. AlMn Transition Edge Sensors for advanced ACTPol. *J. Low Temp. Phys.* **2016**, *184*, 66–73. [CrossRef]
145. Crowley, K.T.; Austermann, J.E.; Choi, S.K.; Duff, S.M.; Gallardo, P.A.; Ho, S.P.P.; Hubmayr, J.; Koopman, B.J.; Nati, F.; Niemack, M.D.; et al. Advanced ACTPoL TES device parameters and noise performance in fielded arrays. *J. Low Temp. Phys.* **2018**, *193*, 328–336. [CrossRef]
146. Galloni, G.; Bartolo, N.; Matarrese, S.; Migliaccio, M.; Ricciardone, A.; Vittorio, N. Updated constraints on amplitude and tilt of the tensor primordial spectrum. *J. Cosmol. Astropart. Phys.* **2023**, *2023*, 062. [CrossRef]
147. Simon, S.; Raghunathan, S.; Appel, J.; Becker, D.; Campusano, L.; Cho, H.; Essinger-Hileman, T.; Ho, S.; Irwin, K.; Jarosik, N.; et al. Characterization of the Atacama B-mode Search. In Proceedings of the Millimeter, Submillimeter, and Far-Infrared Detectors and Instrumentation for Astronomy VII, Montréal, QC, Canada, 22–27 June 2014; SPIE: Bellingham, WA, USA, 2014; Volume 9153, pp. 283–297.
148. Appel, J.W. Detectors for the Atacama B-Mode Search Experiment. Ph.D. Thesis, Princeton University, Princeton, NJ, USA, 2012.
149. Essinger-Hileman, T.; Appel, J.W.; Beal, J.A.; Cho, H.M.; Fowler, J.; Halpern, M.; Hasselfield, M.; Irwin, K.D.; Marriage, T.A.; Niemack, M.D.; et al. The Atacama B-Mode Search: CMB Polarimetry with Transition-Edge-Sensor Bolometers. *AIP Conf. Proc.* **2009**, *1185*, 494–497. [CrossRef]
150. Kusaka, A.; Appel, J.; Essinger-Hileman, T.; Beall, J.A.; Campusano, L.E.; Cho, H.M.; Choi, S.K.; Crowley, K.; Fowler, J.W.; Gallardo, P.; et al. Results from the Atacama B-mode Search (ABS) experiment. *J. Cosmol. Astropart. Phys.* **2018**, *2018*, 005. [CrossRef]
151. Keating, B.G.; Ade, P.A.; Bock, J.J.; Hivon, E.; Holzapfel, W.L.; Lange, A.E.; Nguyen, H.; Yoon, K.W. BICEP: A large angular-scale CMB polarimeter. In *Proccedings of the Polarimetry in Astronomy*; SPIE: Bellingham, WA, USA, 2003; Volume 4843, pp. 284–295.
152. Ade, P.A.; Aikin, R.; Amiri, M.; Barkats, D.; Benton, S.; Bischoff, C.A.; Bock, J.; Brevik, J.; Buder, I.; Bullock, E.; et al. BICEP2. II. Experiment and three-year Data Set. *Astrophys. J.* **2014**, *792*, 62. [CrossRef]
153. Ade, P.A.; Aikin, R.; Barkats, D.; Benton, S.; Bischoff, C.A.; Bock, J.; Bradford, K.; Brevik, J.; Buder, I.; Bullock, E.; et al. BICEP2/Keck array. IV. Optical characterization and performance of the BICEP2 and Keck array experiments. *Astrophys. J.* **2015**, *806*, 206. [CrossRef]
154. Karkare, K.; Ade, P.A.; Ahmed, Z.; Aikin, R.; Alexander, K.; Amiri, M.; Barkats, D.; Benton, S.; Bischoff, C.; Bock, J.; et al. Keck array and BICEP3: Spectral characterization of 5000+ detectors. In Proceedings of the Millimeter, Submillimeter, and Far-Infrared Detectors and Instrumentation for Astronomy VII, Montréal, QC, Canada, 22–27 June 2014; SPIE: Bellingham, WA, USA, 2014; Volume 9153, pp. 1027–1037.
155. Hui, H.; Ade, P.; Ahmed, Z.; Aikin, R.; Alexander, K.D.; Barkats, D.; Benton, S.J.; Bischoff, C.A.; Bock, J.J.; Bowens-Rubin, R.; et al. BICEP Array: A multi-frequency degree-scale CMB polarimeter. In Proceedings of the Millimeter, Submillimeter, and Far-Infrared Detectors and Instrumentation for Astronomy IX, Austin, TX, USA, 12–15 June 2018; SPIE: Bellingham, WA, USA, 2018; Volume 10708, pp. 75–89.
156. Haller, E. Advanced far-infrared detectors. *Infrared Phys. Technol.* **1994**, *35*, 127–146. [CrossRef]
157. Brevik, J.; Aikin, R.; Amiri, M.; Benton, S.; Bock, J.; Bonetti, J.; Burger, B.; Dowell, C.; Duband, L.; Filippini, J.; et al. Initial performance of the BICEP2 antenna-coupled superconducting bolometers at the South Pole. In Proceedings of the Millimeter, Submillimeter, and Far-Infrared Detectors and Instrumentation for Astronomy V, San Diego, CA, USA, 27 June–2 July 2010; SPIE: Bellingham, WA, USA, 2010; Volume 7741, pp. 426–435.
158. Grayson, J.A.; Ade, P.; Ahmed, Z.; Alexander, K.D.; Amiri, M.; Barkats, D.; Benton, S.; Bischoff, C.A.; Bock, J.; Boenish, H.; et al. BICEP3 performance overview and planned Keck Array upgrade. In Proceedings of the Millimeter, Submillimeter, and Far-Infrared Detectors and Instrumentation for Astronomy VIII, Edinburgh, UK, 26 June–1 July 2016; SPIE: Bellingham, WA, USA, 2016; Volume 9914, pp. 157–173.
159. Essinger-Hileman, T.; Ali, A.; Amiri, M.; Appel, J.W.; Araujo, D.; Bennett, C.L.; Boone, F.; Chan, M.; Cho, H.M.; Chuss, D.T.; et al. CLASS: The cosmology large angular scale surveyor. In Proceedings of the Millimeter, Submillimeter, and Far-Infrared Detectors and Instrumentation for Astronomy VII, Montréal, QC, Canada, 22–27 June 2014; SPIE: Bellingham, WA, USA, 2014; Volume 9153, pp. 491–513.
160. Iuliano, J.; Eimer, J.; Parker, L.; Rhoades, G.; Ali, A.; Appel, J.W.; Bennett, C.; Brewer, M.; Bustos, R.; Chuss, D.; et al. The cosmology large angular scale surveyor receiver design. In Proceedings of the Millimeter, Submillimeter, and Far-Infrared Detectors and Instrumentation for Astronomy IX, Austin, TX, USA, 12–15 June 2018; SPIE: Bellingham, WA, USA, 2018; Volume 10708, pp. 259–277.
161. Chuss, D.T.; Ali, A.; Amiri, M.; Appel, J.; Bennett, C.; Colazo, F.; Denis, K.; Dünner, R.; Essinger-Hileman, T.; Eimer, J.; et al. Cosmology large angular scale surveyor (CLASS) focal plane development. *J. Low Temp. Phys.* **2016**, *184*, 759–764. [CrossRef]
162. Eimer, J.R.; Bennett, C.L.; Chuss, D.T.; Marriage, T.; Wollack, E.J.; Zeng, L. The cosmology large angular scale surveyor (CLASS): 40 GHz optical design. In Proceedings of the Millimeter, Submillimeter, and Far-Infrared Detectors and Instrumentation for Astronomy VI, Amsterdam, The Netherlands, 1–6 July 2012; SPIE: Bellingham, WA, USA, 2012; Volume 8452, pp. 619–633.
163. Dahal, S.; Ali, A.; Appel, J.W.; Essinger-Hileman, T.; Bennett, C.; Brewer, M.; Bustos, R.; Chan, M.; Chuss, D.T.; Cleary, J.; et al. Design and characterization of the cosmology large angular scale surveyor (CLASS) 93 GHz focal plane. In Proceedings of the Millimeter, Submillimeter, and Far-Infrared Detectors and Instrumentation for Astronomy IX, Austin, TX, USA, 12–15 June 2018; SPIE: Bellingham, WA, USA, 2018; Volume 10708, pp. 230–245.

164. Appel, J.W.; Ali, A.; Amiri, M.; Araujo, D.; Bennet, C.L.; Boone, F.; Chan, M.; Cho, H.M.; Chuss, D.T.; Colazo, F.; et al. The cosmology large angular scale surveyor (CLASS): 38-GHz detector array of bolometric polarimeters. In Proceedings of the Millimeter, Submillimeter, and Far-Infrared Detectors and Instrumentation for Astronomy VII, Montréal, QC, Canada, 22–27 June 2014; SPIE: Bellingham, WA, USA, 2014; Volume 9153, pp. 514–528.
165. Shirokoff, E.; Benson, B.A.; Bleem, L.E.; Chang, C.L.; Cho, H.M.; Crites, A.T.; Dobbs, M.A.; Holzapfel, W.L.; Lanting, T.; Lee, A.T.; et al. The south pole telescope SZ-receiver detectors. *IEEE Trans. Appl. Supercond.* **2009**, *19*, 517–519. [CrossRef]
166. Austermann, J.E.; Aird, K.; Beall, J.; Becker, D.; Bender, A.; Benson, B.; Bleem, L.; Britton, J.; Carlstrom, J.; Chang, C.; et al. SPTpol: An instrument for CMB polarization measurements with the South Pole Telescope. In Proceedings of the Millimeter, Submillimeter, and Far-Infrared Detectors and Instrumentation for Astronomy VI, Amsterdam, The Netherlands, 1–6 July 2012; SPIE: Bellingham, WA, USA, 2012; Volume 8452, pp. 393–410.
167. Benson, B.A.; Ade, P.; Ahmed, Z.; Allen, S.; Arnold, K.; Austermann, J.; Bender, A.; Bleem, L.; Carlstrom, J.; Chang, C.; et al. SPT-3G: A next-generation cosmic microwave background polarization experiment on the South Pole telescope. In Proceedings of the Millimeter, Submillimeter, and Far-Infrared Detectors and Instrumentation for Astronomy VII, Montréal, QC, Canada, 22–27 June 2014; SPIE: Bellingham, WA, USA, 2014; Volume 9153, pp. 552–572.
168. Anderson, A.; Ade, P.; Ahmed, Z.; Austermann, J.; Avva, J.; Barry, P.; Thakur, R.B.; Bender, A.; Benson, B.; Bleem, L.; et al. Spt-3g: A multichroic receiver for the south pole telescope. *J. Low Temp. Phys.* **2018**, *193*, 1057–1065. [CrossRef]
169. Sobrin, J.; Anderson, A.; Bender, A.; Benson, B.; Dutcher, D.; Foster, A.; Goeckner-Wald, N.; Montgomery, J.; Nadolski, A.; Rahlin, A.; et al. The design and integrated performance of SPT-3G. *Astrophys. J. Suppl. Ser.* **2022**, *258*, 42. [CrossRef]
170. Kermish, Z.D.; Ade, P.; Anthony, A.; Arnold, K.; Barron, D.; Boettger, D.; Borrill, J.; Chapman, S.; Chinone, Y.; Dobbs, M.A.; et al. The POLARBEAR experiment. In Proceedings of the Millimeter, Submillimeter, and Far-Infrared Detectors and Instrumentation for Astronomy VI, Amsterdam, The Netherlands, 1–6 July 2012; SPIE: Bellingham, WA, USA, 2012; Volume 8452, pp. 366–380.
171. Suzuki, A.; Ade, P.; Akiba, Y.; Aleman, C.; Arnold, K.; Atlas, M.; Barron, D.; Borrill, J.; Chapman, S.; Chinone, Y.; et al. The POLARBEAR-2 experiment. *J. Low Temp. Phys.* **2014**, *176*, 719–725. [CrossRef]
172. Barron, D.; Mitchell, K.; Groh, J.; Arnold, K.; Elleflot, T.; Howe, L.; Ito, J.; Lee, A.T.; Lowry, L.N.; Anderson, A.; et al. Integrated electrical properties of the frequency multiplexed cryogenic readout system for POLARBEAR/Simons Array. *IEEE Trans. Appl. Supercond.* **2021**, *31*, 2101805. [CrossRef]
173. Mennella, A.; Ade, P.; Amico, G.; Auguste, D.; Aumont, J.; Banfi, S.; Barbaràn, G.; Battaglia, P.; Battistelli, E.; Baù, A.; et al. QUBIC: Exploring the Primordial Universe with the Q&U Bolometric Interferometer. *Universe* **2019**, *5*, 42. [CrossRef]
174. O'Sulivan, C.; Scully, S.; Gayer, D.; Gradziel, M.; Murphy, J.; De Petris, M.; Buzi, D.; Gervasi, M.; Zannoni, M.; Hamilton, J.; et al. The QU Bolometric Interferometer for Cosmology (QUBIC). In Proceedings of the 36th ESA Antenna Workshop on Antennas and RF Systems for Space Science, Noordwijk, The Netherlands, 6–9 October 2015.
175. Marnieros, S.; Ade, P.; Alberro, J.; Almela, A.; Amico, G.; Arnaldi, L.; Auguste, D.; Aumont, J.; Azzoni, S.; Banfi, S.; et al. TES bolometer arrays for the QUBIC B-mode CMB experiment. *J. Low Temp. Phys.* **2020**, *199*, 955–961. [CrossRef]
176. Piat, M.; Stankowiak, G.; Battistelli, E.; De Bernardis, P.; d'Alessandro, G.; De Petris, M.; Grandsire, L.; Hamilton, J.C.; Hoang, T.; Marnieros, S.; et al. QUBIC IV: Performance of TES bolometers and readout electronics. *J. Cosmol. Astropart. Phys.* **2022**, *2022*, 037. [CrossRef]
177. Ghosh, S.; Liu, Y.; Zhang, L.; Li, S.; Zhang, J.; Wang, J.; Dou, J.; Chen, J.; Delabrouille, J.; Remazeilles, M.; et al. Performance forecasts for the primordial Gravitational Wave detection pipelines for AliCPT-1. *J. Cosmol. Astropart. Phys.* **2022**, *2022*, 063. [CrossRef]
178. Gao, H.; Liu, C.; Li, Z.; Liu, Y.; Li, Y.; Li, S.; Li, H.; Gao, G.; Lu, F.; Zhang, X. Introduction to the detection technology of Ali CMB polarization telescope. *Radiat. Detect. Technol. Methods* **2017**, *1*, 12. [CrossRef]
179. Salatino, M.; Austermann, J.; Thompson, K.L.; Ade, P.A.; Bai, X.; Beall, J.A.; Becker, D.T.; Cai, Y.; Chang, Z.; Chen, D.; et al. The design of the Ali CMB Polarization Telescope receiver. In Proceedings of the Millimeter, Submillimeter, and Far-Infrared Detectors and Instrumentation for Astronomy X, Virtual, 14–18 December 2020; SPIE: Bellingham, WA, USA, 2020; Volume 11453, pp. 341–360.
180. Lee, A.; Abitbol, M.H.; Adachi, S.; Ade, P.; Aguirre, J.; Ahmed, Z.; Aiola, S.; Ali, A.; Alonso, D.; Alvarez, M.A.; et al. The Simons Observatory. *Bull. Am. Astron. Soc* **2019**, *51*, 147.
181. Ade, P.; Aguirre, J.; Ahmed, Z.; Aiola, S.; Ali, A.; Alonso, D.; Alvarez, M.A.; Arnold, K.; Ashton, P.; Austermann, J.; et al. The Simons Observatory: Science goals and forecasts. *J. Cosmol. Astropart. Phys.* **2019**, *2019*, 056. [CrossRef]
182. Stevens, J.R.; Cothard, N.F.; Vavagiakis, E.M.; Ali, A.; Arnold, K.; Austermann, J.E.; Choi, S.K.; Dober, B.J.; Duell, C.; Duff, S.M.; et al. Characterization of Transition Edge Sensors for the Simons observatory. *J. Low Temp. Phys.* **2020**, *199*, 672–680. [CrossRef]
183. Galitzki, N.; Ali, A.; Arnold, K.S.; Ashton, P.C.; Austermann, J.E.; Baccigalupi, C.; Baildon, T.; Barron, D.; Beall, J.A.; Beckman, S.; et al. The Simons observatory: Instrument overview. In Proceedings of the Millimeter, Submillimeter, and Far-Infrared Detectors and Instrumentation for Astronomy IX, Austin, TX, USA, 12–15 June 2018; SPIE: Bellingham, WA, USA, 2018; Volume 10708, pp. 40–52.
184. Bryan, S.A.; Simon, S.M.; Gerbino, M.; Teply, G.; Ali, A.; Chinone, Y.; Crowley, K.; Fabbian, G.; Gallardo, P.A.; Goeckner-Wald, N.; et al. Development of calibration strategies for the Simons Observatory. In Proceedings of the Millimeter, Submillimeter, and Far-Infrared Detectors and Instrumentation for Astronomy IX, Austin, TX, USA, 12–15 June 2018; SPIE: Bellingham, WA, USA, 2018; Volume 10708, pp. 988–1000.

185. Abazajian, K.N.; Adshead, P.; Ahmed, Z.; Allen, S.W.; Alonso, D.; Arnold, K.S.; Baccigalupi, C.; Bartlett, J.G.; Battaglia, N.; Benson, B.A.; et al. CMB-S4 science book. *arXiv* **2016**, arXiv:1610.02743.
186. Abitbol, M.H.; Ahmed, Z.; Barron, D.; Thakur, R.B.; Bender, A.N.; Benson, B.A.; Bischoff, C.A.; Bryan, S.A.; Carlstrom, J.E.; Chang, C.L.; et al. CMB-S4 technology book. *arXiv* **2017**, arXiv:1706.02464.
187. Duff, S.M.; Austermann, J.; Beall, J.A.; Daniel, D.P.; Hubmayr, J.; Jaehnig, G.C.; Johnson, B.R.; Jones, D.; Link, M.J.; Lucas, T.J.; et al. The Simons observatory: Production-level fabrication of the mid-and ultra-high-frequency wafers. *J. Low Temp. Phys.* **2024**, *216*, 135–143. [CrossRef]
188. Abazajian, K.; Abdulghafour, A.; Addison, G.E.; Adshead, P.; Ahmed, Z.; Ajello, M.; Akerib, D.; Allen, S.W.; Alonso, D.; Alvarez, M.; et al. Snowmass 2021 CMB-S4 white paper. *arXiv* **2022**, arXiv:2203.08024.
189. Oxley, P.; Ade, P.A.; Baccigalupi, C.; deBernardis, P.; Cho, H.M.; Devlin, M.J.; Hanany, S.; Johnson, B.; Jones, T.; Lee, A.T.; et al. The EBEX experiment. In Proceedings of the Infrared Spaceborne Remote Sensing XII, Denver, CO, USA, 2–6 August 2004; SPIE: Bellingham, WA, USA, 2004; Volume 5543, pp. 320–331.
190. Reichborn-Kjennerud, B.; Aboobaker, A.M.; Ade, P.; Aubin, F.; Baccigalupi, C.; Bao, C.; Borrill, J.; Cantalupo, C.; Chapman, D.; Didier, J.; et al. EBEX: A balloon-borne CMB polarization experiment. In Proceedings of the Millimeter, Submillimeter, and Far-Infrared Detectors and Instrumentation for Astronomy V, San Diego, CA, USA, 27 June–2 July 2010; SPIE: Bellingham, WA, USA, 2010; Volume 7741, pp. 381–392.
191. Crill, B.; Ade, P.A.; Battistelli, E.S.; Benton, S.; Bihary, R.; Bock, J.; Bond, J.; Brevik, J.; Bryan, S.; Contaldi, C.; et al. SPIDER: A balloon-borne large-scale CMB polarimeter. In Proccedings of the Space Telescopes and Instrumentation 2008: Optical, Infrared, and Millimeter, Marseille, France, 23–28 June 2008; SPIE: Bellingham, WA, USA, 2008; Volume 7010, pp. 800–811.
192. Gualtieri, R.; Filippini, J.; Ade, P.; Amiri, M.; Benton, S.; Bergman, A.; Bihary, R.; Bock, J.; Bond, J.; Bryan, S.; et al. SPIDER: CMB Polarimetry from the Edge of Space. *J. Low Temp. Phys.* **2018**, *193*, 1112–1121. [CrossRef]
193. Gambrel, A.E. Measurement of the Polarization of the Cosmic Microwave Background with the SPIDER Instrument. Ph.D. Thesis, Princeton University, Princeton, NJ, USA, 2018.
194. Hubmayr, J.; Austermann, J.E.; Beall, J.A.; Becker, D.T.; Benton, S.J.; Bergman, A.S.; Bond, J.R.; Bryan, S.; Duff, S.M.; Duivenvoorden, A.J.; et al. Design of 280 GHz feedhorn-coupled TES arrays for the balloon-borne polarimeter SPIDER. In Proceedings of the Millimeter, Submillimeter, and Far-Infrared Detectors and Instrumentation for Astronomy VIII, Edinburgh, UK, 26 June–1 July 2016; SPIE: Bellingham, WA, USA, 2016; Volume 9914, pp. 185–198.
195. Rahlin, A.; Ade, P.; Amiri, M.; Benton, S.; Bock, J.; Bond, J.; Bryan, S.; Chiang, H.C.; Contaldi, C.; Crill, B.; et al. Pre-flight integration and characterization of the SPIDER balloon-borne telescope. In Proceedings of the Millimeter, Submillimeter, and Far-Infrared Detectors and Instrumentation for Astronomy VII, Montréal, QC, Canada, 22–27 June 2014; SPIE: Bellingham, WA, USA, 2014; Volume 9153, pp. 336–360.
196. Lamagna, L.; Addamo, G.; Ade, P.; Baccigalupi, C.; Baldini, A.; Battaglia, P.; Battistelli, E.; Baù, A.; Bersanelli, M.; Biasotti, M.; et al. Progress report on the large-scale polarization explorer. *J. Low Temp. Phys.* **2020**, *200*, 374–383. [CrossRef]
197. Columbro, F.; Battistelli, E.; Coppolecchia, A.; D'Alessandro, G.; de Bernardis, P.; Lamagna, L.; Masi, S.; Pagano, L.; Paiella, A.; Piacentini, F.; et al. The short wavelength instrument for the polarization explorer balloon-borne experiment: Polarization modulation issues. *Astron. Nachrichten* **2019**, *340*, 83–88. [CrossRef]
198. Tartari, A.; Baldini, A.; Cei, F.; Celasco, E.; Dal Bo, P.; Di Giorgi, E.; Ferrari Barusso, L.; Galli, L.; Gatti, F.; Grosso, D.; et al. A Characterization Procedure for Large Area Spiderweb TES. *J. Low Temp. Phys.* **2024**, *216*, 112–118. [CrossRef]
199. Sandri, M. LSPE: The STRIP Instrument. In Proccedings of the Workshop sull'Astronomia Millimetrica in Italia, Bologna, Italy, 7–10 November 2017; p. 35.
200. Matsumura, T.; Akiba, Y.; Borrill, J.; Chinone, Y.; Dobbs, M.; Fuke, H.; Ghribi, A.; Hasegawa, M.; Hattori, K.; Hattori, M.; et al. Mission design of LiteBIRD. *J. Low Temp. Phys.* **2014**, *176*, 733–740. [CrossRef]
201. Sekimoto, Y.; Ade, P.A.; Adler, A.; Allys, E.; Arnold, K.; Auguste, D.; Aumont, J.; Aurlien, R.; Austermann, J.; Baccigalupi, C.; et al. Concept design of low frequency telescope for CMB B-mode polarization satellite LiteBIRD. In Proceedings of the Millimeter, Submillimeter, and Far-Infrared Detectors and Instrumentation for Astronomy X, Virtual, 14–18 December 2020; SPIE: Bellingham, WA, USA, 2020; Volume 11453, pp. 189–209.
202. Montier, L.; Mot, B.; de Bernardis, P.; Maffei, B.; Pisano, G.; Columbro, F.; Gudmundsson, J.E.; Henrot-Versillé, S.; Lamagna, L.; Montgomery, J.; et al. Overview of the medium and high frequency telescopes of the LiteBIRD space mission. In Proccedings of the Space Telescopes and Instrumentation 2020: Optical, Infrared, and Millimeter Wave, Virtual, 14–18 December 2020; SPIE: Bellingham, WA, USA, 2020; Volume 11443, pp. 451–471.
203. Tominaga, M.; Tsujimoto, M.; Smecher, G.; Ishino, H.; Group, L.J.S. Design of the on-board data compression for the bolometer data of LiteBIRD. *J. Low Temp. Phys.* **2022**, *209*, 686–692. [CrossRef]
204. Abdelhameed, A.H.; Angloher, G.; Bauer, P.; Bento, A.; Bertoldo, E.; Bucci, C.; Canonica, L.; D'Addabbo, A.; Defay, X.; Di Lorenzo, S.; et al. First results from the CRESST-III low-mass dark matter program. *Phys. Rev. D* **2019**, *100*, 102002. [CrossRef]
205. Alkhatib, I.; Amaral, D.; Aralis, T.; Aramaki, T.; Arnquist, I.; Ataee Langroudy, I.; Azadbakht, E.; Banik, S.; Barker, D.; Bathurst, C.; et al. Light Dark Matter Search with a High-Resolution Athermal Phonon Detector Operated above Ground. *Phys. Rev. Lett.* **2021**, *127*, 061801. [CrossRef]

206. Lattaud, H.; Armengaud, E.; Arnaud, Q.; Augier, C.; Benoit, A.; Bergé, L.; Billard, J.; Broniatowski, A.; Camus, P.; Cazes, A.; et al. Sub-MeV Dark Matter Searches with EDELWEISS: Results and prospects. In Proceedings of the European Physical Society Conference on High Energy Physics—PoS (EPS-HEP2021), Sissa Medialab, 2022, EPS-HEP2021, Virtual, 26–30 July 2021; p. 153. [CrossRef]
207. D'Angelo, D. DarkSide50 results from first argon run. *arXiv* **2015**, arXiv:1501.03541.
208. Cao, J.; He, Y.; Shang, L.; Zhang, Y.; Zhu, P. Current status of a natural NMSSM in light of LHC 13 TeV data and XENON-1T results. *Phys. Rev. D* **2019**, *99*, 075020. [CrossRef]
209. Adams, D.; Alduino, C.; Alessandria, F.; Alfonso, K.; Andreotti, E.; Avignone III, F.; Azzolini, O.; Balata, M.; Bandac, I.; Banks, T.; et al. CUORE opens the door to tonne-scale cryogenics experiments. *Prog. Part. Nucl. Phys.* **2022**, *122*, 103902. [CrossRef]
210. Agrawal, A.; Alenkov, V.V.; Aryal, P.; Beyer, J.; Bhandari, B.; Boiko, R.S.; Boonin, K.; Buzanov, O.; Byeon, C.R.; Chanthima, N.; et al. Improved limit on neutrinoless double beta decay of $^{100}$Mo from AMoRE-I. *arXiv* **2024**, arXiv:2407.05618.
211. Akimov, D.; Albert, J.; An, P.; Awe, C.; Barbeau, P.; Becker, B.; Belov, V.; Blackston, M.; Blokland, L.; Bolozdynya, A.; et al. COHERENT Collaboration data release from the first detection of coherent elastic neutrino-nucleus scattering on argon. *ArXiV* **2020**, arXiv:2006.12659.
212. O'Hare, C.A.J. New Definition of the Neutrino Floor for Direct Dark Matter Searches. *Phys. Rev. Lett.* **2021**, *127*, 251802. [CrossRef]
213. Boyarsky, A.; Drewes, M.; Lasserre, T.; Mertens, S.; Ruchayskiy, O. Sterile neutrino Dark Matter. *Prog. Part. Nucl. Phys.* **2019**, *104*, 1–45. [CrossRef]
214. Alpert, B.; Balata, M.; Bennett, D.; Biasotti, M.; Boragno, C.; Brofferio, C.; Ceriale, V.; Corsini, D.; Day, P.K.; De Gerone, M.; et al. HOLMES: The electron capture decay of $^{163}$Ho to measure the electron neutrino mass with sub-eV sensitivity. *Eur. Phys. J. C* **2015**, *75*, 112. [CrossRef]
215. Borghesi, M.; Alpert, B.; Balata, M.; Becker, D.; Bennet, D.; Celasco, E.; Cerboni, N.; De Gerone, M.; Dressler, R.; Faverzani, M.; et al. An updated overview of the HOLMES status. *Nucl. Instrum. Methods Phys. Res. Sect. A Accel. Spectrom. Detect. Assoc. Equip.* **2023**, *1051*, 168205. [CrossRef]
216. Croce, M.P.; Rabin, M.W.; Mocko, V.; Kunde, G.J.; Birnbaum, E.R.; Bond, E.; Engle, J.W.; Hoover, A.S.; Nortier, F.M.; Pollington, A.D.; et al. Development of holmium-163 electron-capture spectroscopy with transition-edge sensors. *J. Low Temp. Phys.* **2016**, *184*, 958–968. [CrossRef]
217. Collaboration, C. CUPID pre-CDR. *arXiv* **2019**, arXiv:1907.09376.
218. Alfonso, K.; Armatol, A.; Augier, C.; Avignone III, F.; Azzolini, O.; Balata, M.; Barabash, A.; Bari, G.; Barresi, A.; Baudin, D.; et al. CUPID: The next-generation neutrinoless double beta decay experiment. *J. Low Temp. Phys.* **2023**, *211*, 375–383. [CrossRef]
219. Singh, V.; Beretta, M.; Hansen, E.; Vetter, K.; Benato, G.; Marini, L.; Capelli, C.; Fujikawa, B.; Schmidt, B.; Chang, C.; et al. Large-area photon calorimeter with Ir-Pt bilayer transition-edge sensor for the CUPID experiment. *Phys. Rev. Appl.* **2023**, *20*, 064017. [CrossRef]
220. Bratrud, G.; Chang, C.L.; Chen, R.; Cudmore, E.; Figueroa-Feliciano, E.; Hong, Z.; Kennard, K.T.; Lewis, S.; Lisovenko, M.; Mateo, L.O.; et al. First demonstration of a TES based cryogenic $Li_2MoO_4$ detector for neutrinoless double beta decay search. *arXiv* **2024**, arXiv:2406.02025.
221. Pagnanini, L.; Benato, G.; Carniti, P.; Celi, E.; Chiesa, D.; Corbett, J.; Dafinei, I.; Di Domizio, S.; Di Stefano, P.; Ghislandi, S.; et al. Array of cryogenic calorimeters to evaluate the spectral shape of forbidden $\beta$-decays: The ACCESS project. *Eur. Phys. J. Plus* **2023**, *138*, 445. [CrossRef]
222. Strauss, R.; Rothe, J.; Angloher, G.; Bento, A.; Gütlein, A.; Hauff, D.; Kluck, H.; Mancuso, M.; Oberauer, L.; Petricca, F.; et al. The Nucleus experiment: A gram-scale fiducial-volume cryogenic detector for the first detection of coherent neutrino–nucleus scattering. *Eur. Phys. J. C* **2017**, *77*, 506. [CrossRef]
223. Collaboration, N.; Angloher, G.; Ardellier-Desages, F.; Bento, A.; Canonica, L.; Erhart, A.; Ferreiro, N.; Friedl, M.; Ghete, V.; Hauff, D.; et al. Exploring CE$\nu$NS with NUCLEUS at the Chooz nuclear power plant. *Eur. Phys. J. C* **2019**, *79*, 1018.
224. Goupy, C.; Marnieros, S.; Mauri, B.; Nones, C.; Vivier, M. Prototyping a High Purity Germanium cryogenic veto system for a bolometric detection experiment. *Nucl. Instrum. Methods Phys. Res. Sect. A Accel. Spectrom. Detect. Assoc. Equip.* **2024**, *1064*, 169383. [CrossRef]
225. Agnolet, G.; Baker, W.; Barker, D.; Beck, R.; Carroll, T.; Cesar, J.; Cushman, P.; Dent, J.; De Rijck, S.; Dutta, B.; et al. Background studies for the MINER coherent neutrino scattering reactor experiment. *Nucl. Instrum. Methods Phys. Res. Sect. A Accel. Spectrom. Detect. Assoc. Equip.* **2017**, *853*, 53–60. [CrossRef]
226. Adari, P.; Aguilar-Arevalo, A.A.; Amidei, D.; Angloher, G.; Armengaud, E.; Augier, C.; Balogh, L.; Banik, S.; Baxter, D.; Beaufort, C.; et al. EXCESS workshop: Descriptions of rising low-energy spectra. *SciPost Phys. Proc.* **2022**, *9*, 001. [CrossRef]
227. Angloher, G.; Banik, S.; Benato, G.; Bento, A.; Bertolini, A.; Breier, R.; Bucci, C.; Burkhart, J.; Canonica, L.; D'Addabbo, A.; et al. Observation of a low energy nuclear recoil peak in the neutron calibration data of the CRESST-III experiment. *Phys. Rev. D* **2023**, *108*, 022005. [CrossRef]
228. Pattavina, L.; Ferreiro Iachellini, N.; Tamborra, I. Neutrino observatory based on archaeological lead. *Phys. Rev. D* **2020**, *102*, 063001. [CrossRef]

229. Pattavina, L.; Iachellini, N.F.; Pagnanini, L.; Canonica, L.; Celi, E.; Clemenza, M.; Ferroni, F.; Fiorini, E.; Garai, A.; Gironi, L.; et al. RES-NOVA sensitivity to core-collapse and failed core-collapse supernova neutrinos. *J. Cosmol. Astropart. Phys.* **2021**, *2021*, 064. [CrossRef]
230. Augier, C.; Beaulieu, G.; Belov, V.; Berge, L.; Billard, J.; Bres, G.; Bret, J.L.; Broniatowski, A.; Calvo, M.; Cazes, A.; et al. Ricochet progress and status. *J. Low Temp. Phys.* **2023**, *212*, 127–137. [CrossRef]
231. First demonstration of 30 eVee ionization energy resolution with Ricochet germanium cryogenic bolometers. *Eur. Phys. J. C* **2024**, *84*, 186. [CrossRef] [PubMed]
232. Chen, R.; Pinckney, H.D.; Figueroa-Feliciano, E.; Hong, Z.; Schmidt, B. Transition Edge Sensor Chip Design of a Modular CE$\nu$NS Detector for the Ricochet Experiment. *J. Low Temp. Phys.* **2023**, *211*, 237–247. [CrossRef]
233. Augier, C.; Baulieu, G.; Belov, V.; Bergé, L.; Billard, J.; Bres, G.; Broniatowski, A.; Calvo, M.; Cazes, A.; Chaize, D.; et al. Results from a prototype TES detector for the Ricochet experiment. *Nucl. Instrum. Methods Phys. Res. Sect. A Accel. Spectrom. Detect. Assoc. Equip.* **2023**, *1057*, 168765. [CrossRef]
234. Bravin, M.; Bruckmayer, M.; Bucci, C.; Cooper, S.; Giordano, S.; von Feilitzsch, F.; Höhne, J.; Jochum, J.; Jörgens, V.; Keeling, R.; et al. The CRESST dark matter search. *Astropart. Phys.* **1999**, *12*, 107–114. [CrossRef]
235. Angloher, G.; Bento, A.; Bucci, C.; Canonica, L.; Defay, X.; Erb, A.; von Feilitzsch, F.; Iachellini, N.F.; Gorla, P.; Gütlein, A.; et al. Results on light dark matter particles with a low-threshold CRESST-II detector. *Eur. Phys. J. C Part. Fields* **2016**, *76*, 25. [CrossRef]
236. Rothe, J.; Angloher, G.; Bauer, P.; Bento, A.; Bucci, C.; Canonica, L.; D'Addabbo, A.; Defay, X.; Erb, A.; Feilitzsch, F.v.; et al. TES-based light detectors for the CRESST direct dark matter search. *J. Low Temp. Phys.* **2018**, *193*, 1160–1166. [CrossRef]
237. Kurinsky, N.; Brink, P.; Partridge, R.; Cabrera, B.; Pyle, M. SuperCDMS SNOLAB low-mass detectors: Ultra-sensitive phonon calorimeters for a sub-GeV dark matter search. *arXiv* **2016**, arXiv:1611.04083.
238. Bähre, R.; Döbrich, B.; Dreyling-Eschweiler, J.; Ghazaryan, S.; Hodajerdi, R.; Horns, D.; Januschek, F.; Knabbe, E.A.; Lindner, A.; Notz, D.; et al. Any light particle search II—Technical Design Report. *J. Instrum.* **2013**, *8*, T09001. [CrossRef]
239. Sikivie, P. Experimental Tests of the "Invisible" Axion. *Phys. Rev. Lett.* **1983**, *51*, 1415–1417. [CrossRef]
240. Rubiera Gimeno, J.A.; Januschek, F.; Isleif, K.S.; Lindner, A.; Meyer, M.; Othman, G.; Schwemmbauer, C.; Shah, R. A TES system for ALPS II - Status and Prospects. *Proc. Sci.* **2023**, *449*, 567. [CrossRef]
241. Armengaud, E.; Arnaud, Q.; Augier, C.; Benoît, A.; Bergé, L.; Bergmann, T.; Billard, J.; De Boissière, T.; Bres, G.; Broniatowski, A.; et al. Performance of the EDELWEISS-III experiment for direct dark matter searches. *J. Instrum.* **2017**, *12*, P08010. [CrossRef]
242. Marnieros, S.; Armengaud, E.; Arnaud, Q.; Augier, C.; Benoît, A.; Bergé, L.; Billard, J.; Broniatowski, A.; Camus, P.; Cazes, A.; et al. High impedance TES bolometers for EDELWEISS. *J. Low Temp. Phys.* **2023**, *211*, 214–219. [CrossRef]
243. Lattaud, H.; Guy, E.; Billard, J.; Colas, J.; Jésus, M.D.; Gascon, J.; Juillard, A.; Marnieros, S.; Oriol, C. Characterization of the Phonon Sensor of the CRYOSEL Detector with IR Photons. *J. Low Temp. Phys.* **2024**, *215*, 268–275. [CrossRef]
244. Capparelli, L.; Cavoto, G.; Ferretti, J.; Giazotto, F.; Polosa, A.; Spagnolo, P. Axion-like particle searches with sub-THz photons. *Phys. Dark Universe* **2016**, *12*, 37–44. [CrossRef]
245. He, K.; Zhang, X.; Ren, S.; Sun, J. Deep Residual Learning for Image Recognition. In Proceedings of the 2016 IEEE Conference on Computer Vision and Pattern Recognition (CVPR), Las Vegas, NV, USA, 27–30 June 2016; pp. 770–778. [CrossRef]
246. Bernabei, R.; Belli, P.; Bussolotti, A.; Cappella, F.; Caracciolo, V.; Cerulli, R.; Dai, C.; d'Angelo, A.; Di Marco, A.; Ferrari, N.; et al. The DAMA project: Achievements, implications and perspectives. *Prog. Part. Nucl. Phys.* **2020**, *114*, 103810. [CrossRef]
247. Krishak, A.; Dantuluri, A.; Desai, S. Robust model comparison tests of DAMA/LIBRA annual modulation. *J. Cosmol. Astropart. Phys.* **2020**, *2020*, 007. [CrossRef]
248. Angloher, G.; Carniti, P.; Cassina, L.; Gironi, L.; Gotti, C.; Gütlein, A.; Hauff, D.; Maino, M.; Nagorny, S.; Pagnanini, L.; et al. The COSINUS project: Perspectives of a NaI scintillating calorimeter for dark matter search. *Eur. Phys. J. C* **2016**, *76*, 441. [CrossRef]
249. Angloher, G.; Bharadwaj, M.; Dafinei, I.; Di Marco, N.; Einfalt, L.; Ferroni, F.; Fichtinger, S.; Filipponi, A.; Frank, T.; Friedl, M.; et al. Deep-underground dark matter search with a COSINUS detector prototype. *Phys. Rev. D* **2024**, *110*, 043010. [CrossRef]
250. Abeln, A.; Altenmüller, K.; Arguedas Cuendis, S.; Armengaud, E.; Attié, D.; Aune, S.; Basso, S.; Bergé, L.; Biasuzzi, B.; Borges De Sousa, P.; et al. Conceptual design of BabyIAXO, the intermediate stage towards the International Axion Observatory. *J. High Energy Phys.* **2021**, *2021*, 137.
251. Billard, J.; Gascon, J.; Marnieros, S.; Scorza, S. Transition Edge Sensors with Sub-eV Resolution and Cryogenic Targets (TESSERACT) at the underground laboratory of Modane (LSM). *Nucl. Phys. B* **2024**, *1003*, 116465. [CrossRef]
252. Hertel, S.A.; Biekert, A.; Lin, J.; Velan, V.; McKinsey, D.N. Direct detection of sub-GeV dark matter using a superfluid $^4$He target. *Phys. Rev. D* **2019**, *100*, 092007. [CrossRef]
253. Anthony-Petersen, R.; Biekert, A.; Bunker, R.; Chang, C.L.; Chang, Y.Y.; Chaplinsky, L.; Fascione, E.; Fink, C.W.; Garcia-Sciveres, M.; Germond, R.; et al. A stress induced source of phonon bursts and quasiparticle poisoning. *arXiv* **2022**, arXiv:2208.02790. [CrossRef]
254. Icha, J.; Weber, M.; Waters, J.C.; Norden, C. Phototoxicity in live fluorescence microscopy, and how to avoid it. *BioEssays* **2017**, *39*, 1700003. [CrossRef]
255. Niwa, K.; Numata, T.; Hattori, K.; Fukuda, D. Few-photon color imaging using energy-dispersive superconducting transition-edge sensor spectrometry. *Sci. Rep.* **2017**, *7*, 45660. [CrossRef]

256. Fukuda, D.; Fujii, G.; Numata, T.; Amemiya, K.; Yoshizawa, A.; Tsuchida, H.; Fujino, H.; Ishii, H.; Itatani, T.; Inoue, S.; et al. Titanium-based transition-edge photon number resolving detector with 98% detection efficiency with index-matched small-gap fiber coupling. *Opt. Express* **2011**, *19*, 870–875. [CrossRef]
257. Niwa, K.; Hattori, K.; Fukuda, D. Few-photon spectral confocal microscopy for cell imaging using superconducting Transition Edge Sensor. *Front. Bioeng. Biotechnol.* **2021**, *9*, 789709. [CrossRef]
258. Hattori, K.; Kobayashi, R.; Takasu, S.; Fukuda, D. Complex impedance of a transition-edge sensor with sub-$\mu$s time constant. *AIP Adv.* **2020**, *10*, 035004. [CrossRef]
259. Fukuda, D. Single-photon measurement techniques with a superconducting Transition Edge Sensor. *IEICE Trans. Electron.* **2019**, *102*, 230–234. [CrossRef]
260. Hao, L.; Gallop, J.; Gardiner, C.; Josephs-Franks, P.; Macfarlane, J.; Lam, S.; Foley, C. Inductive superconducting transition-edge detector for single-photon and macro-molecule detection. *Supercond. Sci. Technol.* **2003**, *16*, 1479. [CrossRef]
261. Hong, C.K.; Ou, Z.Y.; Mandel, L. Measurement of subpicosecond time intervals between two photons by interference. *Phys. Rev. Lett.* **1987**, *59*, 2044–2046. [CrossRef]
262. Di Giuseppe, G.; Atatüre, M.; Shaw, M.D.; Sergienko, A.V.; Saleh, B.E.; Teich, M.C.; Miller, A.J.; Nam, S.W.; Martinis, J. Direct observation of photon pairs at a single output port of a beam-splitter interferometer. *Phys. Rev. A* **2003**, *68*, 063817. [CrossRef]
263. Knill, E.; Laflamme, R.; Milburn, G.J. A scheme for efficient quantum computation with linear optics. *Nature* **2001**, *409*, 46–52. [CrossRef]
264. Gisin, N.; Thew, R. Quantum communication. *Nat. Photonics* **2007**, *1*, 165–171. [CrossRef]
265. Chunnilall, C.J.; Degiovanni, I.P.; Kück, S.; Müller, I.; Sinclair, A.G. Metrology of single-photon sources and detectors: A review. *Opt. Eng.* **2014**, *53*, 081910. [CrossRef]
266. Schmidt, M.; Von Helversen, M.; López, M.; Gericke, F.; Schlottmann, E.; Heindel, T.; Kück, S.; Reitzenstein, S.; Beyer, J. Photon-number-resolving transition-edge sensors for the metrology of quantum light sources. *J. Low Temp. Phys.* **2018**, *193*, 1243–1250. [CrossRef]
267. Gerrits, T.; Lita, A.; Calkins, B.; Nam, S.W. Superconducting Transition Edge Sensors for quantum optics. In *Superconducting Devices in Quantum Optics*; Springer: Berlin/Heidelberg, Germany, 2016; pp. 31–60.
268. Gerrits, T.; Glancy, S.; Clement, T.S.; Calkins, B.; Lita, A.E.; Miller, A.J.; Migdall, A.L.; Nam, S.W.; Mirin, R.P.; Knill, E. Generation of optical coherent-state superpositions by number-resolved photon subtraction from the squeezed vacuum. *Phys. Rev. A—At. Mol. Opt. Phys.* **2010**, *82*, 031802. [CrossRef]
269. Bartley, T.J.; Donati, G.; Spring, J.B.; Jin, X.M.; Barbieri, M.; Datta, A.; Smith, B.J.; Walmsley, I.A. Multiphoton state engineering by heralded interference between single photons and coherent states. *Phys. Rev. A—At. Mol. Opt. Phys.* **2012**, *86*, 043820. [CrossRef]
270. Sridhar, N.; Shahrokhshahi, R.; Miller, A.J.; Calkins, B.; Gerrits, T.; Lita, A.; Nam, S.W.; Pfister, O. Direct measurement of the Wigner function by photon-number-resolving detection. *J. Opt. Soc. Am. B* **2014**, *31*, B34–B40. [CrossRef]
271. Laiho, K.; Cassemiro, K.N.; Gross, D.; Silberhorn, C. Probing the negative Wigner function of a pulsed single photon point by point. *Phys. Rev. Lett.* **2010**, *105*, 253603. [CrossRef]
272. Zhai, Y.; Becerra, F.E.; Glebov, B.L.; Wen, J.; Lita, A.E.; Calkins, B.; Gerrits, T.; Fan, J.; Nam, S.W.; Migdall, A. Photon-number-resolved detection of photon-subtracted thermal light. *Opt. Lett.* **2013**, *38*, 2171–2173. [CrossRef]
273. Clauser, J.F.; Horne, M.A. Experimental consequences of objective local theories. *Phys. Rev. D* **1974**, *10*, 526. [CrossRef]
274. Christensen, B.G.; McCusker, K.T.; Altepeter, J.B.; Calkins, B.; Gerrits, T.; Lita, A.E.; Miller, A.; Shalm, L.K.; Zhang, Y.; Nam, S.W.; et al. Detection-loophole-free test of quantum nonlocality, and applications. *Phys. Rev. Lett.* **2013**, *111*, 130406. [CrossRef]
275. Giustina, M.; Mech, A.; Ramelow, S.; Wittmann, B.; Kofler, J.; Beyer, J.; Lita, A.; Calkins, B.; Gerrits, T.; Nam, S.W.; et al. Bell violation using entangled photons without the fair-sampling assumption. *Nature* **2013**, *497*, 227–230. [CrossRef]
276. Heindel, T.; Thoma, A.; von Helversen, M.; Schmidt, M.; Schlehahn, A.; Gschrey, M.; Schnauber, P.; Schulze, J.H.; Strittmatter, A.; Beyer, J.; et al. A bright triggered twin-photon source in the solid state. *Nat. Commun.* **2017**, *8*, 14870. [CrossRef]
277. Schlottmann, E.; von Helversen, M.; Leymann, H.A.; Lettau, T.; Krüger, F.; Schmidt, M.; Schneider, C.; Kamp, M.; Höfling, S.; Beyer, J.; et al. Exploring the photon-number distribution of bimodal microlasers with a Transition Edge Sensor. *Phys. Rev. Appl.* **2018**, *9*, 064030. [CrossRef]
278. Klaas, M.; Schlottmann, E.; Flayac, H.; Laussy, F.; Gericke, F.; Schmidt, M.; Helversen, M.v.; Beyer, J.; Brodbeck, S.; Suchomel, H.; et al. Photon-number-resolved measurement of an exciton-polariton condensate. *Phys. Rev. Lett.* **2018**, *121*, 047401. [CrossRef]
279. Wilen, C.D.; Abdullah, S.; Kurinsky, N.; Stanford, C.; Cardani, L.; d'Imperio, G.; Tomei, C.; Faoro, L.; Ioffe, L.; Liu, C.; et al. Correlated charge noise and relaxation errors in superconducting qubits. *Nature* **2021**, *594*, 369–373. [CrossRef] [PubMed]
280. McEwen, M.; Faoro, L.; Arya, K.; Dunsworth, A.; Huang, T.; Kim, S.; Burkett, B.; Fowler, A.; Arute, F.; Bardin, J.C.; et al. Resolving catastrophic error bursts from cosmic rays in large arrays of superconducting qubits. *Nat. Phys.* **2022**, *18*, 107–111. [CrossRef]
281. Cardani, L.; Valenti, F.; Casali, N.; Catelani, G.; Charpentier, T.; Clemenza, M.; Colantoni, I.; Cruciani, A.; D'Imperio, G.; Gironi, L.; et al. Reducing the impact of radioactivity on quantum circuits in a deep-underground facility. *Nat. Commun.* **2021**, *12*, 2733. [CrossRef]
282. Orrell, J.L.; Loer, B. Sensor-assisted fault mitigation in quantum computation. *Phys. Rev. Appl.* **2021**, *16*, 024025. [CrossRef]
283. Maehata, K.; Hara, T.; Mitsuda, K.; Hidaka, M.; Tanaka, K.; Yamanaka, Y. A Transition Edge Sensor microcalorimeter system for the energy dispersive spectroscopy performed on a scanning-transmission electron microscope. *J. Low Temp. Phys.* **2016**, *184*, 5–10. [CrossRef]

284. Lee, S.J.; Titus, C.J.; Alonso Mori, R.; Baker, M.L.; Bennett, D.A.; Cho, H.M.; Doriese, W.B.; Fowler, J.W.; Gaffney, K.J.; Gallo, A.; et al. Soft X-ray spectroscopy with transition-edge sensors at Stanford Synchrotron Radiation Lightsource beamline 10-1. *Rev. Sci. Instrum.* **2019**, *90*, 113101. [CrossRef]
285. Ullom, J.; Doriese, W.; Fischer, D.; Fowler, J.; Hilton, G.; Jaye, C.; Reintsema, C.; Swetz, D.; Schmidt, D. Transition-edge sensor microcalorimeters for X-ray beamline science. *Synchrotron Radiat. News* **2014**, *27*, 24–27. [CrossRef]
286. Doriese, W.B.; Abbamonte, P.; Alpert, B.K.; Bennett, D.; Denison, E.; Fang, Y.; Fischer, D.; Fitzgerald, C.; Fowler, J.; Gard, J.; et al. A practical superconducting-microcalorimeter X-ray spectrometer for beamline and laboratory science. *Rev. Sci. Instrum.* **2017**, *88*, 053108. [CrossRef] [PubMed]
287. Miaja-Avila, L.; O'Neil, G.C.; Uhlig, J.; Cromer, C.L.; Dowell, M.L.; Jimenez, R.; Hoover, A.; Silverman, K.L.; Ullom, J.N. Laser plasma X-ray source for ultrafast time-resolved X-ray absorption spectroscopy. *Struct. Dyn.* **2015**, *2*, 024301. [CrossRef]
288. Joe, Y.I.; O'Neil, G.C.; Miaja-Avila, L.; Fowler, J.W.; Jimenez, R.; Silverman, K.; Swetz, D.; Ullom, J. Observation of iron spin-states using tabletop X-ray emission spectroscopy and microcalorimeter sensors. *J. Phys. B At. Mol. Opt. Phys.* **2015**, *49*, 024003. [CrossRef]
289. Uhlig, J.; Doriese, W.; Fowler, J.; Swetz, D.; Jaye, C.; Fischer, D.; Reintsema, C.; Bennett, D.; Vale, L.; Mandal, U.; et al. High-resolution X-ray emission spectroscopy with transition-edge sensors: Present performance and future potential. *J. Synchrotron Radiat.* **2015**, *22*, 766–775. [CrossRef] [PubMed]
290. Palosaari, M.; Käyhkö, M.; Kinnunen, K.; Laitinen, M.; Julin, J.; Malm, J.; Sajavaara, T.; Doriese, W.; Fowler, J.; Reintsema, C.; et al. Broadband ultrahigh-resolution spectroscopy of particle-induced x rays: Extending the limits of nondestructive analysis. *Phys. Rev. Appl.* **2016**, *6*, 024002. [CrossRef]
291. Yamada, S.; Ichinohe, Y.; Tatsuno, H.; Hayakawa, R.; Suda, H.; Ohashi, T.; Ishisaki, Y.; Uruga, T.; Sekizawa, O.; Nitta, K.; et al. Broadband high-energy resolution hard X-ray spectroscopy using Transition Edge Sensors at SPring-8. *Rev. Sci. Instrum.* **2021**, *92*, 013103. [CrossRef] [PubMed]
292. Morgan, K.M.; Becker, D.T.; Bennett, D.A.; Doriese, W.B.; Gard, J.D.; Irwin, K.D.; Lee, S.J.; Li, D.; Mates, J.A.; Pappas, C.G.; et al. Use of transition models to design high performance TESs for the LCLS-II soft X-ray spectrometer. *IEEE Trans. Appl. Supercond.* **2019**, *29*, 2100605. [CrossRef] [PubMed]
293. Okada, S.; Bennett, D.; Doriese, W.; Fowler, J.; Irwin, K.; Ishimoto, S.; Sato, M.; Schmidt, D.; Swetz, D.; Tatsuno, H.; et al. High-resolution kaonic-atom X-ray spectroscopy with transition-edge-sensor microcalorimeters. *J. Low Temp. Phys.* **2014**, *176*, 1015–1021. [CrossRef]
294. Tatsuno, H.; Bennett, D.; Doriese, W.; Durkin, M.; Fowler, J.; Gard, J.; Hashimoto, T.; Hayakawa, R.; Hayashi, T.; Hilton, G.; et al. Mitigating the effects of charged particle strikes on TES arrays for exotic atom X-ray experiments. *J. Low Temp. Phys.* **2020**, *200*, 247–254. [CrossRef]
295. collaboration, H.; Okada, S.; Bennett, D.; Curceanu, C.; Doriese, W.; Fowler, J.; Gard, J.; Gustafsson, F.; Hashimoto, T.; Hayano, R.; et al. First application of superconducting transition-edge sensor microcalorimeters to hadronic atom X-ray spectroscopy. *Prog. Theor. Exp. Phys.* **2016**, *2016*, 091D01.
296. Seki, R.; Masutani, K. Unified analysis of pionic atoms and low-energy pion-nucleus scattering: Phenomenological analysis. *Phys. Rev. C* **1983**, *27*, 2799. [CrossRef]
297. Hashimoto, T.; Bazzi, M.; Bennett, D.; Berucci, C.; Bosnar, D.; Curceanu, C.; Doriese, W.; Fowler, J.; Fujioka, H.; Guaraldo, C.; et al. Beamline test of a transition-edge-sensor spectrometer in preparation for kaonic-atom measurements. *IEEE Trans. Appl. Supercond.* **2016**, *27*, 2100905. [CrossRef]
298. Hashimoto, T.; Aikawa, S.; Akaishi, T.; Asano, H.; Bazzi, M.; Bennett, D.; Berger, M.; Bosnar, D.; Butt, A.; Curceanu, C.; et al. Measurements of strong-interaction effects in kaonic-helium isotopes at sub-eV precision with X-ray microcalorimeters. *Phys. Rev. Lett.* **2022**, *128*, 112503. [CrossRef]
299. Aoki, K.; Fujioka, H.; Gogami, T.; Hidaka, Y.; Hiyama, E.; Honda, R.; Hosaka, A.; Ichikawa, Y.; Ieiri, M.; Isaka, M.; et al. Extension of the J-PARC hadron experimental facility: Third white paper. *arXiv* **2021**, arXiv:2110.04462.
300. Pappas, C.G.; Durkin, M.; Fowler, J.W.; Morgan, K.M.; Ullom, J.N.; Doriese, W.B.; Hilton, G.C.; O'Neil, G.C.; Schmidt, D.R.; Szypryt, P.; et al. A TES X-ray spectrometer for NSENSE. *Proc. GOMACTech.* **2019**, 300–305.
301. Szypryt, P.; Nakamura, N.; Becker, D.T.; Bennett, D.A.; Dagel, A.L.; Doriese, W.B.; Fowler, J.W.; Gard, J.D.; Harris, J.Z.; Hilton, G.C.; et al. A tabletop X-ray tomography instrument for nanometer-scale imaging: Demonstration of the 1000-element transition-edge sensor subarray. *IEEE Trans. Appl. Supercond.* **2023**, *33*, 2100705. [CrossRef]
302. Nakamura, N.; Szypryt, P.; Dagel, A.L.; Alpert, B.K.; Bennett, D.A.; Doriese, W.B.; Durkin, M.; Fowler, J.W.; Fox, D.T.; Gard, J.D.; et al. Nanoscale Three-Dimensional Imaging of Integrated Circuits Using a Scanning Electron Microscope and Transition-Edge Sensor Spectrometer. *Sensors* **2024**, *24*, 2890. [CrossRef] [PubMed]
303. Levine, Z.H.; Alpert, B.K.; Dagel, A.L.; Fowler, J.W.; Jimenez, E.S.; Nakamura, N.; Swetz, D.S.; Szypryt, P.; Thompson, K.R.; Ullom, J.N. A tabletop X-ray tomography instrument for nanometer-scale imaging: Reconstructions. *Microsyst. Nanoeng.* **2023**, *9*, 47. [CrossRef]
304. Kikuchi, T.; Fujii, G.; Hayakawa, R.; Smith, R.; Hirayama, F.; Sato, Y.; Kohjiro, S.; Ukibe, M.; Ohno, M.; Sato, A.; et al. A 320-keV Spectrometer Based on 8-Pixel Transition Edge Sensor With Trilayer Membrane and Novel Numerical Analysis. *IEEE Trans. Appl. Supercond.* **2023**, *33*, 2101706. [CrossRef]

305. Hoover, A.S.; Winkler, R.; Rabin, M.W.; Bennett, D.A.; Doriese, W.B.; Fowler, J.W.; Hayes-Wehle, J.; Horansky, R.D.; Reintsema, C.D.; Schmidt, D.R.; et al. Uncertainty of Plutonium Isotopic Measurements with Microcalorimeter and High-Purity Germanium Detectors. *IEEE Trans. Nucl. Sci.* **2014**, *61*, 2365–2372. [CrossRef]
306. Bennett, D.A.; Horansky, R.D.; Schmidt, D.R.; Hoover, A.; Winkler, R.; Alpert, B.K.; Beall, J.A.; Doriese, W.B.; Fowler, J.W.; Fitzgerald, C.; et al. A high resolution gamma-ray spectrometer based on superconducting microcalorimeters. *Rev. Sci. Instrum.* **2012**, *83*, 093113. [CrossRef]
307. Zink, B.L.; Ullom, J.; Beall, J.A.; Irwin, K.D.; Doriese, W.B.; Duncan, W.; Ferreira, L.; Hilton, G.C.; Horansky, R.; Reintsema, C.D.; et al. Array-compatible transition-edge sensor microcalorimeter $\gamma$-ray detector with 42 eV energy resolution at 103 keV. *Appl. Phys. Lett.* **2006**, *89*, 124101. [CrossRef]
308. Ullom, J.; Doriese, W.B.; Beall, J.A.; Duncan, W.; Ferreira, L.; Hilton, G.C.; Horansky, R.; Irwin, K.D.; Jach, T.; Mates, B.; et al. Multiplexed microcalorimeter arrays for precision measurements from microwave to gamma-ray wavelengths. *Nucl. Instrum. Methods Phys. Res. Sect. A Accel. Spectrom. Detect. Assoc. Equip.* **2007**, *579*, 161–164. [CrossRef]
309. Hoover, A.; Hoteling, N.; Rabin, M.; Ullom, J.; Bennett, D.; Karpius, P.; Vo, D.; Doriese, W.; Hilton, G.; Horansky, R.; et al. Large microcalorimeter arrays for high-resolution X-and gamma-rayspectroscopy. *Nucl. Instrum. Methods Phys. Res. Sect. A Accel. Spectrom. Detect. Assoc. Equip.* **2011**, *652*, 302–305. [CrossRef]
310. Ullom, J.; Zink, B.; Beall, J.; Doriese, W.; Duncan, W.; Ferreira, L.; Hilton, G.; Irwin, K.; Reintsema, C.; Vale, L.; et al. Development of large arrays of microcalorimeters for precision gamma-ray spectroscopy. In Proceedings of the IEEE Nuclear Science Symposium Conference Record, Fajardo, PR, USA, 23–29 October 2005; Volume 2, pp. 1154–1158. [CrossRef]
311. Doriese, W.B.; Ullom, J.; Beall, J.A.; Duncan, W.; Ferreira, L.; Hilton, G.C.; Horansky, R.; Irwin, K.D.; Mates, J.; Reintsema, C.D.; et al. Toward a 256-pixel array of gamma-ray microcalorimeters for nuclear-materials analysis. *J. Low Temp. Phys.* **2008**, *151*, 754–759. [CrossRef]
312. Bacrania, M.K.; Hoover, A.S.; Karpius, P.J.; Rabin, M.W.; Rudy, C.R.; Vo, D.T.; Beall, J.A.; Bennett, D.A.; Doriese, W.B.; Hilton, G.C.; et al. Large-Area Microcalorimeter Detectors for Ultra-High-Resolution X-Ray and Gamma-Ray Spectroscopy. *IEEE Trans. Nucl. Sci.* **2009**, *56*, 2299–2302. [CrossRef]
313. Hoover, A.S.; Winkler, R.; Rabin, M.W.; Vo, D.T.; Ullom, J.N.; Bennett, D.A.; Doriese, W.B.; Fowler, J.W.; Horansky, R.D.; Schmidt, D.R.; et al. Determination of Plutonium Isotopic Content by Microcalorimeter Gamma-Ray Spectroscopy. *IEEE Trans. Nucl. Sci.* **2013**, *60*, 681–688. [CrossRef]
314. Winkler, R.; Hoover, A.; Rabin, M.; Bennett, D.; Doriese, W.; Fowler, J.; Hays-Wehle, J.; Horansky, R.; Reintsema, C.; Schmidt, D.; et al. 256-pixel microcalorimeter array for high-resolution $\gamma$-ray spectroscopy of mixed-actinide materials. *Nucl. Instrum. Methods Phys. Res. Sect. A Accel. Spectrom. Detect. Assoc. Equip.* **2015**, *770*, 203–210. [CrossRef]
315. Becker, D.T.; Alpert, B.K.; Bennett, D.A.; Croce, M.P.; Fowler, J.W.; Gard, J.D.; Hoover, A.S.; Joe, Y.I.; Koehler, K.E.; Mates, J.A.; et al. Advances in analysis of microcalorimeter gamma-ray spectra. *IEEE Trans. Nucl. Sci.* **2019**, *66*, 2355–2363. [CrossRef]
316. Fomin, V.N. *Optimal Filtering: Volume I: Filtering of Stochastic Processes*; Springer Science & Business Media: Berlin/Heidelberg, Germany, 2012; Volume 457.
317. Croce, M.; Henzlova, D.; Menlove, H.; Becker, D.; Ullom, J. Electrochemical Safeguards Measurement Technology Development at LANL. *J. Nucl. Mater. Manag.* **2021**, *49*, 116–135.
318. Croce, M.; Becker, D.; Bennett, D.; Cantor, R.; Carpenter, M.; Feissle, E.; Friedrich, S.; Gard, J.; Imrek, J.; Kim, G.; et al. *Nuclear Facility Experience with the SOFIA Ultra-High-Resolution Microcalorimeter Gamma Spectrometer*; Technical Report; Lawrence Livermore National Lab. (LLNL): Livermore, CA, USA, 2022.
319. Mercer, D.J.; Winkler, R.; Koehler, K.E.; Becker, D.T.; Bennett, D.A.; Carpenter, M.H.; Croce, M.P.; de Castro, K.I.; Feissle, E.A.; Fowler, J.W.; et al. Quantification of 242Pu with a Microcalorimeter Gamma Spectrometer. *arXiv* **2022**, arXiv:2202.02933.
320. Day, P.K.; LeDuc, H.G.; Mazin, B.A.; Vayonakis, A.; Zmuidzinas, J. A broadband superconducting detector suitable for use in large arrays. *Nature* **2003**, *425*, 817–821. [CrossRef]
321. Ulbricht, G.; De Lucia, M.; Baldwin, E. Applications for microwave kinetic induction detectors in advanced instrumentation. *Appl. Sci.* **2021**, *11*, 2671. [CrossRef]
322. Walter, A.; Mazin, B.B.; Bockstiegel, C.; Fruitwala, N.; Szypryt, P.; Lipartito, I.; Meeker, S.; Zobrist, N.; Collura, G.; Coiffard, G.; et al. MEC: The MKID exoplanet camera for high contrast astronomy at Subaru (Conference Presentation). In Proceedings of the Ground-Based and Airborne Instrumentation for Astronomy VII, Austin, TX, USA, 10–15 June 2018; Evans, C.J., Simard, L., Takami, H., Eds.; International Society for Optics and Photonics SPIE: Bellingham, WA, USA, 2018; Volume 10702. [CrossRef]
323. Vissers, M.R.; Gao, J.; Kline, J.S.; Sandberg, M.; Weides, M.P.; Wisbey, D.S.; Pappas, D.P. Characterization and in-situ monitoring of sub-stoichiometric adjustable superconducting critical temperature titanium nitride growth. *Thin Solid Films* **2013**, *548*, 485–488. [CrossRef]
324. De Lucia, M.; Baldwin, E.; Ulbricht, G.; Piercy, J.; Creaner, O.; Bracken, C.; Ray, T. High-uniformity TiN/Ti/TiN multilayers for the development of Microwave Kinetic Inductance Detectors. In Proceedings of the X-Ray, Optical, and Infrared Detectors for Astronomy X, Montréal, QC, Canada, 17–23 July 2022; SPIE: Bellingham, WA, USA, 2022; Volume 12191, pp. 21–31.
325. McAleer, C.; Creaner, O.; Bracken, C.; Ulbricht, G.; De Lucia, M.; Piercy, J.; Ray, T. Automation of MKID Simulations for Array Building with AEM (Automated Electromagnetic MKID Simulations). *J. Low Temp. Phys.* **2024**, *216*, 57–66. [CrossRef] [PubMed]

326. McKenney, C.M.; Austermann, J.E.; Beall, J.A.; Dober, B.J.; Duff, S.M.; Gao, J.; Hilton, G.C.; Hubmayr, J.; Li, D.; Ullom, J.N.; et al. Tile-and-trim micro-resonator array fabrication optimized for high multiplexing factors. *Rev. Sci. Instrum.* **2019**, *90*, 023908. [CrossRef] [PubMed]
327. De Lucia, M.; Baldwin, E.; Ulbricht, G.; Bracken, C.; Stamenov, P.; Ray, T. Multiplexable frequency retuning of MKID arrays using their non-linear kinetic inductance. In *X-Ray, Optical, and Infrared Detectors for Astronomy IX;* SPIE: Bellingham, WA, USA, 2020; Volume 11454, pp. 580–590.